UC Berkeley
UC Berkeley Electronic Theses and Dissertations

Title
Bandgap Engineering of Gallium Telluride

Permalink
https://escholarship.org/uc/item/9dp4z0f3

Author
Fonseca Vega, Jose Javier

Publication Date
2017

Peer reviewed|Thesis/dissertation

eScholarship.org Powered by the California Digital Library
University of California

Bandgap Engineering of Gallium Telluride

By

Jose Javier Fonseca Vega

A dissertation submitted in partial satisfaction of the
requirements for the degree of
Doctor of Philosophy

in

Engineering – Materials Science and Engineering

in the

Graduate Division

of the

University of California, Berkeley

Committee in charge:
Professor Oscar D. Dubón, Chair
Professor Jie Yao
Professor Ali Javey

Summer 2017

Abstract

Bandgap Engineering of Gallium Telluride

by

Jose Javier Fonseca Vega

Doctor of Philosophy in Engineering – Materials Science and Engineering

University of California, Berkeley

Professor Oscar D. Dubón, Chair

Layered semiconductors, like transition-metal dichalcogenides and III-VI monochalcogenides, possess interesting properties attractive for future opto-electronic applications. Among the III-VI monochalcogenides, gallium telluride (GaTe) possesses a unique monoclinic structure, good p-type transport properties, and contrary to most layered materials, a direct bandgap in the bulk (1.67 eV). This dissertation explores different avenues for the bandgap engineering of GaTe, including access to the bandstructure through the layers' surfaces, conventional semiconductor alloying and stabilization of alternate metastable phases.

In the presence of air, mechanically exfoliated GaTe develops a deep-level defect band effectively reducing the bandgap in a direct-to-indirect transition to about 0.8 eV. The intercalation and chemisorption of molecular oxygen to the Te-terminated layers was responsible for the behavior. I discuss on how surface defects created by the mechanical exfoliation facilitate the transformation as well as procedures to delay or accelerate such transformation. Contrary to traditional bandgap engineering methods, the partial reversibility of this process can also be achieved.

The alignment of the conduction and valence band edges as well as shallow-defect levels were determined following an ion irradiation study. Based on the amphoteric defect model, the conduction band and valence band edges of GaTe were found to be 3.47 eV and 5.12 eV below vacuum, respectively. Low-temperature spectroscopy found two acceptor levels around 100 and 150 meV above the valence band and a donor level around 130 meV below the conduction band.

Gallium selenide (GaSe) and GaTe alloys ($GaSe_xTe_{1-x}$) were grown by vapor deposition. Monoclininc crystals were obtained for $x < 0.32$, and hexagonal crystals were obtained for $x >$

0.28. The bandgap of the monoclinic phase increases linearly with Se content from 1.65 eV to 1.77 eV while hexagonal-phase bandgap decreases from 2.01 eV (GaSe) to 1.38 eV (x = 0.28). Finally, the bandgap of hexagonal GaTe was confirmed to be 1.45 eV, by epitaxially growing hexagonal GaTe crystals on GaSe substrates. The results presented here show how the selected bandgap-engineering avenue can affect the structural and opto-electronic properties of GaTe.

A mis padres, José y Eva, por todo su apoyo y sacrificios que han permitido mis logros.

To my parents, José and Eva, for all their support and sacrifices that have allowed my success.

Table of Contents

List of Figures

List of Tables

List of Acronyms and Symbols

Acronyms

0D, 1D, 2D, 3D	zero, one, two and three dimensional material
1T	Tetragonal structure composed of one layer
1T’	Distorted 1T
2H	Hexagonal structure composed of two layers
3R	Rhombohedral structure composed of three layers
4H	Hexagonal structure composed of four layers
AFM	Atomic force microscopy
ANDM	Amphoteric native defect model
AX, A_1X, A_2X	Acceptor bound excitons
CBM	Conduction band minimum
DAP, DA_1P, DA_2P	Donor-acceptor pair transition
DFT	Density functional theory
diH_2O	De-ionized water
DOS, PDOS	Full and partial density of states
DX	Donor bound exciton
EBSD	Electron backscattering diffraction
EDS	Energy dispersive x-ray spectroscopy
FB_A, FB_{A1}, FB_{A2}	Free-to-acceptor-bound transition
FB_D	Free-to-donor-bound transition
FWHM	Full-width at half maximum
FX	Free exciton
GIXD	Grazing-incidence x-ray diffraction
HSE	Heyd-Scuseria-Ernzerhof
ICSD	Inorganic Crystal Structure Database
III-V	Compound semiconductor composed of III and V elements
III-VI	Compound semiconductor composed of III and VI elements
IR	Infrared
MBJ	Tran-Blaha modified-Becke Johnson
PAW	Projected augmented wave
PBE	Perdew-Burke-Ernzerhof
PL	Photoluminescence
PR	Photomodulated reflectance
RMS	Root-mean-square
SEM	Scanning electron microscopy
SO	Spin-orbit
SRIM	Stopping and Range of Ions in Matter software

STS	Scanning tunneling spectroscopy
TMD	Transition-metal dichalcogenide
UV-Vis	Ultraviolet to visible light range
VASP	Vienna Ab-initio Simulation Package
VBM	Valence band maximum
VCA	Virtual crystal approximation
XPS	X-ray photoelectron spectroscopy
XRD	X-ray diffraction

Symbols

2θ	Diffracted angle
a, b, c, β	Lattice parameters and angles
A, l	Cross-sectional area and length
A, Γ, H, K, L, M	Brillouin-zone high-symmetry points for the hexagonal structures
α-, β-, γ-, δ-, ε-	Crystal structure polytypes
$\alpha(E)$	Absorption coefficient
$Abs(E)$, $T(E)$, $R(E)$	Absorbance, transmittance and reflectance
b	Hayne’s rule constant
$b_{\perp}$, $b_{\parallel}$	Axis perpendicular or parallel to the b-axis
B_z	Magnetic field applied in the z-axis
d	Penetration depth
E	Energy
E_A, E_{A1}, E_{A2}	Activation energy of the acceptors
E_{AD}, E_{DD}	Acceptor-defect and donor-defect energy level
E_{BA}, E_{BA1}, E_{BA2}	Binding energy of the exciton to the acceptors
E_C, E_V	Conduction band minimum and valence band maxium
E_D	Activation energy of the donor
E_F	Fermi energy
E_{FS}	Fermi stabilization energy
E_g^{dir}, E_g^{ind}	Direct and indirect bandgap energy
E_p	Phonon energy
E_X	Exciton binding energy
F, Γ, H, I, L, M, N, X, Y, Z	Brillouin-zone high-symmetry points for monoclinic GaTe
h	Planck’s constant
I_0	Diffracted intensity at surface
I_L	Diffracted intensity at a given depth L
I_{mn}	Current flowing from m to n
k_B	Boltzmann constant
μ	Linear absorption coefficient of x-rays

m_e	Electron mass
m_h^*	Effective hole mass
μ_h	Hole mobility
N_V	Effective density of states in the valence band
ω	Incident angle
p	Hole concentration
p_{sat}	Saturated hole concentration
q_e	Elementary charge
ρ	Resistivity
$R_{uv,mn}$	Resistance measured with V_{uv} and I_{mn}
t	Thickness
T	Temperature
V_H	Hall-voltage
V_{uv}	Electric potencial (voltage) measured between u and w
χ	Electron affinity
ZT	Thermoelectric figure of merit

Acknowledgements

I must thank all the people who made this dissertation possible through their mentorship, guidance, support, motivation and friendship throughout my graduate school life.

First of all, I want to thank my advisor, Prof. Oscar Dubón, for all his guidance inside and outside the lab. Oscar's dedication to the academic advancement as well as the well-being of the students in his group have been essential for my scientific and profesional development.

I would like to thank the other members of my committee, Profs. Jie Yao and Ali Javey, for their comments on the preparation of this dissertation. Also, Profs. Yao and Mark Asta for all their mentorship and support along the years including, but not limited to, Master's report, qualifying exam and letters of recommendation. I want to thanks Prof. Junqiao Wu for the continuous access to instruments in his lab and for his research guidance earlier on my graduate student career. Additionally, I want to thank Prof. Eduardo Nicolau, at the University of Puerto Rico, Rio Piedras, for all his scientific and academic mentorship, career advice and friendship for the past ten years. He has been instrumental in my career, including my decision to come to UC Berkeley for graduate school.

I would also like to thank past and current members of the Dubón group and the extended Electronic Materials (EMAT) group at LBNL, including Dr. Joseph Wofford, Dr. Alejandro Levander, Dr. Douglas Detert, Dr. Alex Luce, Dr. Paul Rogge, Prof. Sefaattin Tongay, Dr. Changhyun Ko, Dr. Min Ting, Dr. Kevin Wang, Dr. Joonki Suh, Dr. Marie Mayer, Dr, Karen Bustillo, Dr. Erin Ford, Dr. Hui Fang, Dr. Mahmut Tosun, Dr. Yabin Chen, Dr. Matthew Horton. Jeffrey Beeman, Grant Buchowickz, Christopher Francis, Maribel Jaquez, Edy Cardona, Xiaojie Xu, Kyle Tom, Matin Amani, Anand Sampat and visitors Prof. James Heyman and Prof. Juan Sanchez-Royo. I want to give special thanks to the Dubón's GaTe subgroup that I had the priviledge to mentor and that contributed significantly to the work presented in this dissertation, Alex Tseng, Alex Lin, Holly Ubellacker and Karlene Vega. I want to thank Dr. Petra Specht for all her help in electron microscopy and valuable mentorship over the years; and Dr. Erick Ulin-Ávila for his help during my first year at UC Berkeley, getting to learn more about the field of layered electronic materials. Also, thanks to my scientific collaborators outside UC Berkeley and LBNL, Prof. Alberto Salleo, Dr. Mehemet Topsakal and Annabel Chew.

I want to acknowledge the support from the National Science Foundation Graduate Research Fellowships Program (Grant No. DGE-1106400) and UC Berkeley Chancellor's Fellowship for graduate students. The research project presented here is also part of the Electronic Materials Program at the Lawrence Berkeley National Laboratory, supported by the Director, Office of Science, Office of Basic Energy Sciences, Materials Sciences and Engineering Division, of the U.S. Department of Energy under Contract No. DE-AC02-05CH11231.

Outside of lab I want to thank all of my friends for their support, including those in MSE, LAGSES, across campus, Berkeley/Bay Area and back home in Puerto Rico. All of them made my tenure at UC Berkeley possible and enjoyable. Specially, I want to thank the "*Amigos*", who have been there for me since the beginning, with a couple of additions: Dr. Isaac Markus, Dr. Joo Chuan Ang, Dr. Brian Panganiban, Dr. William Chang, Tim Lee, Shawn Darnall, Ian Winters

and Benson Jung. Similar thanks to Dr. Enid Contés, Dr. Karla Ramos, the “*Boris (A-Team)*” and the “*Savages*”, who brought a bit of Puerto Rico to the Bay Area. I’m grateful to Natalia Díaz, Nicole Carreras and Gabriela Fernández-Cuervo who were always there and kept me motivated.

Finally, to my family, thanks for all of their support. To my parents, José and Eva, my brother Rafi and the rest of the extended Fonseca-Vega family, who have always be supporting me every step of my career, even from afar and without even knowing what an electron is, thank you!

Chapter 1

Introduction

1.1 Motivation for bandgap engineering of layered semiconductors

Most modern-day electronic devices–transistors, light emitting diodes and solar cells–are based on semiconductor technologies, mainly around silicon and group III-V materials (GaAs, GaN, etc.).[1,2] As technology evolves, smaller and faster devices with higher capacity are in more demand.[2] To maintain this trend, the limitations of state-of-the-art devices have to be constantly improving. Smaller high-performance electronic materials with different shapes and mechanical properties are in demand for diverse applications.[1,3] Similarly, there's a need for electronic materials whose properties cater to the specific requirements of applications, optimizing the device's performance.[3] Physical and electronic limitations of silicon will prevent the continued usage of this material in many future opto-electronic applications.[1,2] For this, we have engaged in studying low-dimensionality materials and their electrical properties. Specifically, we have focused on studying layered semiconductors which can potentially form single-crystalline few-atom-thick films without compromising their performance.[4,5] On top of that, their electronic properties can be further tuned, by bandgap engineering, to optimize their performance for a desired application.[6,7]

1.2 The rise of layered semiconductors

In 2004 the discovery of graphene by Geim and Novoselov started the continuously-expanding field of atomically-thin layered electronic materials.[8,9] Graphene was discovered by the mechanical exfoliation and isolation of a single layer of sp^2-bonded carbon from a bulk piece of graphite. This atomically-thin crystal exhibited extraordinary mechanical and electrical properties, like a tensile strength of 130 GPa and carrier mobility over 200,000 cm^2/Vs.[9–11] Graphene also exhibits metallic behavior and the absence of an energy band gap, which is essential for most modern electronic devices.[9] While attempts on opening a band gap in graphene have been made–through orienting bilayer graphene, controlling the width of nanoribbons and surface functionalization–the magnitude of the resulting bandgap is limited.[12–14] Hence, efforts have been focused on the discovery and characterization of new and interesting two-dimensional semiconducting materials from layered bulk crystals.

Layered semiconductors can be divided into two main groups, transition-metal dichalcogenides (TMD) and III-VI monochalcogenides, with the former being widely more popular and studied. The popularity of TMDs arises from their interesting opto-electronic properties, particularly in the single-layer regime, where an indirect-to-direct bandgap transition

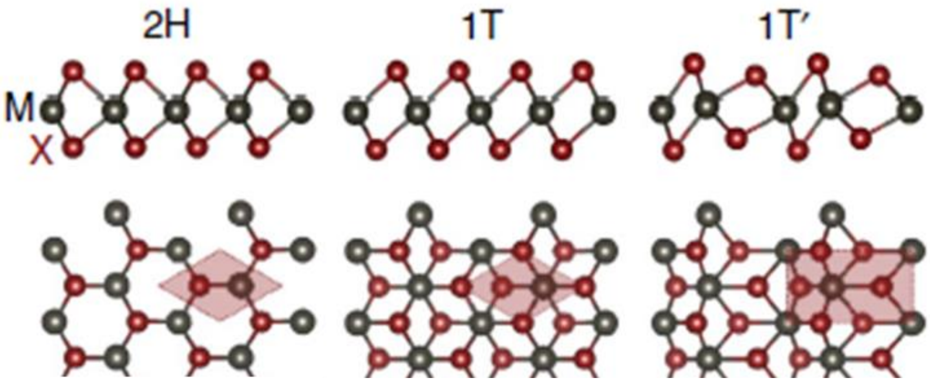

Figure 1.1. Lateral and top-view of the 2H, 1T and 1T' crystal structures. The pink area represents the primitive unit cell.[17]

takes place.[4,5,15] As direct semiconductors, monolayer TMDs exhibit strong absorption and photoluminescence (PL) and have been considered excellent candidates for photodetectors and light-emitting applications.[16] The crystal structures of TMD semiconductors consist of a three-atom X-M-X assembly, where X represents a chalcogenide atom (sulfur, selenium or tellurium) and M represents a transition-metal atom.[5,15] The covalently-bonded assemblies form two-dimensional layers that stack on top of each other by van der Waals forces.

The bonding coordination of the transition-metal atom will vary depending on the chemical composition and growth conditions, between trigonal prismatic, octahedral and distorted octahedral.[5,17,18] The trigonal prismatic coordination will result in the formation of a hexagonal lattice (2H), where the chalcogenide atoms align with those at the other side of the layer, see Figure 1.1.[5,17] In turn, the octahedral coordination will result in a tetragonal lattice (1T), where the chalcogenide atoms at one side of the layer are rotated 60° along the layer plane, compared to the 2H structure. The distorted octahedral coordination and resulting distorted tetragonal phase (1T') are generally observed for larger chalcogenides, like tellurides.[19,20] The octahedral bonds distort their lengths and angles to accommodate the large chalcogenide, these distortions generate the stabilized 1T' phase.

Molybdenum and tungsten-based TMDs have been in the center of attention for many years now. These materials typically behave as semiconductors that crystallize in the 2H phase (e.g. MoS_2, WS_2, $MoSe_2$, WSe_2 and $MoTe_2$) while WTe_2 is a semimetal that crystallizes in the 1T' phase.[4,5,15,19] For $MoTe_2$, the 2H phase is more stable for bulk crystals at room temperature, however the semimetallic 1T' phase is close in energy and phase transformations from 2H to 1T' have been observed at high temperatures and in the few-layer regime.[20,22] As mentioned above, one of the most interesting properties of these semiconductors is the indirect-to-direct bandgap transformation at the monolayer. This transformation is evident by the increase in the photoluminescence intensity by several orders of magnitude, in the single-layer crystals (Figure1.2.a).[4,23,24] The transformation is explained by the removal of the adjacent-layers interactions–responsible for the conduction-band minimum and valence-band maximum in the multi-layered crystal–resulting in new and aligned band extrema (Figure 1.2.b-d).[21] The bandgaps of TMDs also experience a significant increase at the monolayer regime; for example, in MoS_2 the bulk bandgap is 1.29 eV while the bilayer and monolayer bandgaps are 1.59 eV and

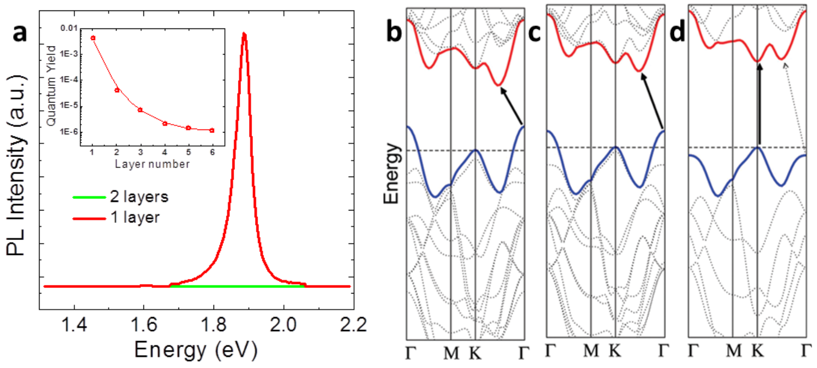

Figure 1.2. (a) PL spectra for mono- and bilayer MoS_2 samples. Inset: PL Quatum Yield as a function of amount of layers.[4] **(b)-(d)** Bandstructure of bulk, bilayer and monolayer MoS_2, the indirect-to-direct bandgap transformation is evident.[21]

1.89 eV, respectively.[4,21]

Tin, hafnium and zirconium-based TMDs, on the other hand, crystallize in the 1T phase.[5,25] Sulfides and selenides of these compounds (i.e. SnS_2, HfS_2, ZrS_2, $SnSe_2$, $HfSe_2$ and $ZrSe_2$) behave as semiconductors with similar properties as those based on molybdenum or tungsten. Tellurides ($SnTe_2$, $HfTe_2$ and $ZrTe_2$) show semimetallic behavior, similar to 1T'-$MoTe_2$ and WTe_2.[20,25] In general, monolayers of both 2H and 1T TMD semiconductors exhibit bandgaps around the 1 – 2.5 eV range, but only the 2H phase exhibits the indirect-to-direct bandgap transition.[4,5,24,26–28] This energy range can be ideal for several electronic applications like transistors or other switching electronics, light emitting devices and solar cell active layers.

1.3 III-VI monochalcogenide semiconductors

III-VI monochalcogenide semiconductors are also part of the larger family of layered electronic materials. This small group includes four semiconductors: GaS, GaSe, GaTe and InSe. The intralayer structure of these semiconductors consist on an X-M-M-X assembly, where X represents the chalcogenide and M represents either gallium or indium metal.[29–31] Similar to TMDs, Van der Waals forces at the interlayer keep the layer stacking together. Generally, the layers of these semiconductors have a hexagonal structure where each metal has a tetrahedral coordination bonded to three chalcogenides and one other metal. The metal-chalcogenide bonds on each side of the layer are aligned in such a way that the X-M-M-X assembly forms a trigonal prism, similar to the 2H-TMD structure (Figure 1.3.a).[29,30] The only exception is GaTe which crystallizes in a monoclinic structure;[30] a more detailed discussion about GaTe's crystal structure can be found in Section 1.2.1.

While GaS, GaSe and InSe have the same intralayer structure, the possible layer-stacking sequences can result in different polytypes with slightly different properties for the same compound. Gallium sulfide (GaS) preferentially crystallizes in the β-polytype, where two layers are aligned in a way that the chalcogenides and metals of the second layer sit on top of the metals and chalcogenides of the first layer, respectively.[31] The β-polytype has a three-dimensional hexagonal unit cell consisting of two layers (2H) with symmetry represented by the $P6_3/mmc$

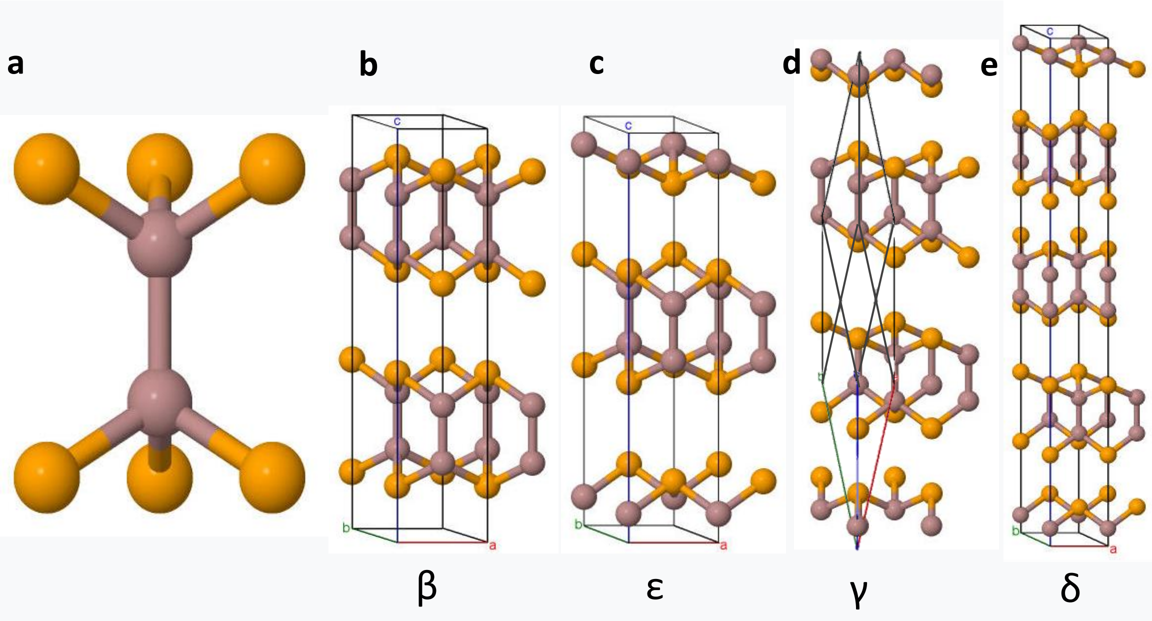

Figure 1.3. (a) Trigonal prismatic assembly in III-VI monochalcogenide semiconductors. **(b)-(e)** unit cells of the β-, ε-, γ- and δ-polytypes.[32–34]

space group (Figure 1.3.b).[31,33] Gallium selenide (GaSe) instead prefers the ε-polytype, in which two layers align themselves where the chalcogenides (or the metals) of the second layer sit on top of the metals (chalcogenides) of the first layer, but not both.[30,33] The ε-polytype also has a three-dimensional hexagonal unit cell consisting of two layers (2H) but with the symmetry represented by the $P\bar{6}m2$ space group, instead (Figure 1.3.c).[33] Finally, indium selenide (InSe) preferentially stacks in the γ-polytype which results when a third layer is added to the ε-polytype where the chalcogenides (or metals) of this layer sit on top of the metals (chalcogenides) of the second layer that weren't aligned to any atom on the first layer.[30] Different to β- and ε-polytypes, the γ-polytype unit cell has a rhombohedral structure consisting of three layers (3R) and its symmetry is represented by the R3m space group (Figure 1.3.d).[30] It is important to state that these semiconductors are capable of stacking in polytypes different from their preferred ones. For example, GaSe has also been observed in the β-, γ- and even the δ-polytype, which consists of a hexagonal unit cell of four layers (4H) obtained by the combination of the β- and ε-polytypes (Figure 1.3.e).[32,33]

The layer thickness of GaS is about 7.75 Å, where the Ga-S and Ga-Ga bond lengths are 2.37 Å and 2.48 Å, respectively.[35] The lattice parameters are a = 3.59 Å and c = 15.49 Å. GaS is an indirect bandgap semiconductor (2.59 eV) with a direct gap of 3.05 eV.[36] As-grown GaS tends to be n-type with electron concentration around $10^{12} – 10^{13}$ cm^{-3} and bulk mobility up to 80 cm^2/Vs.[37,38] The unintentionally doped n-type behavior arises mainly from sulfur vacancies. Attempts to increase either the electron or hole carrier concentration in GaS haven't shown significant results.[37]

The GaSe unit cell dimensions are a = 3.74 Å and c = 15.92 Å, where the layer thickness of is about 7.96 Å, and the Ga-Se and Ga-Ga bond lengths are 2.48 Å and 2.38 Å, respectively.[33] Similar to GaS, GaSe is an indirect semiconductor (2.0 eV) with the direct gap about 25 meV larger.[39] This small difference in energy between the indirect and direct gaps allows GaSe to exhibit photoluminescence, similar to a direct semiconductor.[39,40] For unintentionally doped GaSe, gallium vacancies are typically the dominant defect, which causes p-type behavior.[41] Hole concentration ranges around 10^{14} – 10^{15} cm^{-3} while the hole mobility has been reported to reach up to 215 cm^{2}/Vs.[41,42] The low carrier concentration, and thus the high resistivity, of GaSe hinder the use if this material in many electronic applications. However, the most interesting opto-electronic properties of GaSe are the non-linear optical properties in the infrared (IR) range.[43,44] GaSe is a well-known second-harmonic generating material and promising candidate for terahertz (THz) source and tuning, due to its anisotropic structure, high optical birefringence, high transparency and high nonlinear susceptibility.[43]

As mentioned before, InSe has a rhombohedral crystal structure, which can be defined with a hexagonal unit cell of the following parameters a = 4.01 Å and c = 24.96 Å or with its primitive rhombohedral unit cell parameters: a = 4.01 Å and α = 26.85°.[45] Its layer thickness is about 8.32 Å, and the In-Se and In-In bond lengths are 2.63 Å and 2.77 Å, respectively. Contrary to GaS and GaSe, InSe has a direct bandgap of 1.25 eV but goes through a direct-to-indirect bandgap transition when the crystal is thinned-down to less than 20 layers.[46] Below 20 layers, the bandstructure near the valence band maximum takes the form of an inverted “Mexican hat”, with the new valence band maximum shifting farther away from the direct gap, with reduced thickness.[46] Monolayer InSe has an indirect bandgap around 1.9 eV, with the direct gap about 70 meV larger. Unintentionally-doped InSe typically shows n-type behavior with the electron concentration around 10^{15} cm^{-3} and one of the highest electron mobility for layered semiconductors at room temperature 600 – 1000 cm^{2}/Vs.[47–49] N-type and p-type doping has been successfully achieved in InSe with carrier concentrations exceeding the 10^{17} cm^{-3} for both carrier types, without significantly affecting the mobility (500 – 800 cm^{2}/Vs).[49,50]

1.3.1 Gallium Telluride (GaTe)

Gallium telluride, the last member of the III-VI monochalcogenide semiconducting family, is an interesting material with several unique properties. First off, it is the only member of this family that does not have the same intralayer structure, but a distorted version of it. Starting from the same intralayer structure as the other members of the family, GaTe’s structure can be obtained when one out of every other third Ga-Ga bond in the layer is flipped horizontally along the layer plane.[30] This modification will cause restructuring of the bond angles and slight changes to the bond lengths, resulting in a two-dimensional monoclinic structure (Figure 1.4.a). In this reduced-symmetry structure, there are three different Ga and Te atomic positions, as shown in Figure 1.4.b.[52] The different bond lengths within a layer are shown in Table 1. The GaTe layers are around 7.47 Å in thickness and preferentially stack in the monoclinic α-structure, with a = 17.40 Å, b = 4.08 Å, c = 10.46 Å and β = 104.50° (Figure 1.4.c).[51] A metastable hexagonal phase for GaTe has also been reported with the β-2H (GaS-like) structure, rapidly changing back to the monoclinic structure.[53–55]

The in-plane anisotropy of α-GaTe, gives the material unique orientation-dependent structural, electrical and optical properties, not observed in most layered semiconductors. Structurally, the layer exhibits mechanical weakness at the in-plane Ga-Ga bonds, commonly cleaving there.[56,57] The in-plane Ga-Ga bonds are aligned along the $b_{\perp}$-axis or the [2 0 1] direction.[51] Optically, the layer anisotropy doesn’t have much impact on the bandgap and

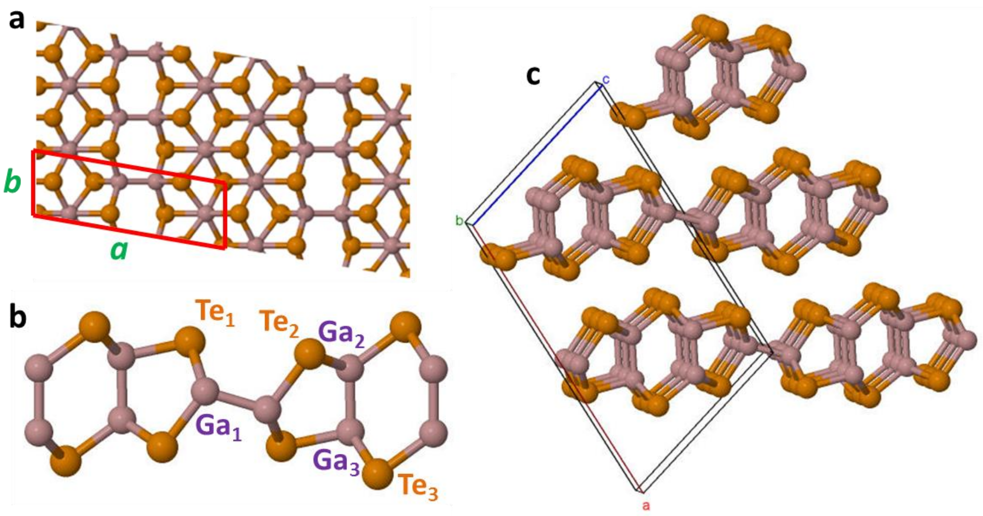

Figure 1.4. (a) Two-dimensional monoclinic unit cell of GaTe monolayer (top view). **(b)** Different atomic positions for Ga and Te in GaTe monolayer (side view). **(c)** Multi-layer α-GaTe and monoclinic unit cell.[34,51]

absorption coefficient; however the effects are more evident on the excitons observed by optical absorption and photoluminescence spectroscopy.[56,58,59] The exciton peaks observed with polarized light along the $b_{\perp}$-axis tend to split into twin peaks and be more prominent than those observed with light polarized along the $b_{\parallel}$-axis. The slight differences in the absorption spectrum arise mainly due to the anisotropy on the refractive index, which along $b_{\perp}$ is larger for wavelengths below 1,000 nm and smaller afterwards, compared to the refractive index along $b_{\parallel}$.[56] The layer anisotropy is also evident through the active Raman modes observed under polarized light.[60,61] In-plane anisotropy is probably more noticeable in the electrical resistivity of the material, which can increase by about two orders of magnitude from $b_{\parallel}$ to $b_{\perp}$.[30]

Gallium telluride is a direct bandgap semiconductor with a gap of 1.67 eV at room temperature and 1.78 eV at 0K.[62] Even at room temperature, it shows strong excitonic absorption and emission around 1.65 eV or about 18 meV below bandgap.[62,63] Unintentionally-doped gallium telluride typically shows good p-type transport behavior with carrier concentrations around 10^{16} – 10^{17} cm^{-3}.[30,64] Similar to GaSe, the main source of acceptor defects are the gallium vacancies.[63,65] The in-plane hole mobility will depend on the crystal orientation, but average values are around 30 – 40 cm^2/Vs.[30,64,66]

Several applications have been demonstrated for GaTe over the years. Traditionally, GaTe has been considered a candidate for radiation detection given its relatively high average atomic number, intermediate bandgap and good transport properties.[52,57] GaTe transistors have shown to have ON/OFF ratios around 10^5 and hole mobility over 4 cm^2/Vs.[67,68] Visible-light photodetectors have also been demonstrated for few-layer GaTe with photoresponsivities as high as 10^4 A/W–higher than graphene and MoS_2–and detectivity around 10^{12} Jones–larger than commercially available InGaAs photodetectors.[69,70] Nanosheet-based and nanowire-based flexible photodetectors with promising performances have also been fabricated.[71,72]

Table 1.1. Bond lengths within a layer of GaTe. Atomic positions shown in Figure 1.4.b.[51]

Bond	Bond length (Å)	Bond	Bond length (Å)
Ga_1–Ga_1	2.44	Ga_2–Te_2	2.67
Ga_1–Te_1	2.68	Ga_2–Te_3	2.64
Ga_1–Te_2	2.69	Ga_3–Te_1	2.65
Ga_2–Ga_3	2.44	Ga_3–Te_3	2.66

Heterojunctions with n-Si and n-MoS_2 have exhibited external quantum efficiencies around 62% and fill factors around 0.4, displaying their potential capability for solar applications.[66,73] As shown here, GaTe is a layered semiconductor with unique and interesting properties that shows potential for opto-electronic applications. The work presented in this dissertation further expands our knowledge on this material and its properties.

1.4 Bandgap engineering

The ability to precisely tune the electrical properties of materials has always been of upmost interest to scientists and engineers. The bandgap engineering of semiconductors is a powerful tool that has been in use for decades, allowing such control on the energy gap of materials. Several methods for bandgap engineering have been developed throughout the years, but with new and exciting materials–like layered semiconductors–new methods will be needed and discovered based on these materials properties. Throughout the remaining of this chapter, we will discuss some of the most common methods of bandgap engineering and how they relate to the field of layered semiconductors.

There are three main approaches typically employed to modify the bandstructure of an electronic material. First, the bandstructure can be modified by altering the crystal structure of the material, either by slight distortions or complete phase transformations.[17,74] Distortions in the crystal structure can be achieved by applying stress to the material. Tensile or compressive stress application will result in a strained unit cell that could alter the crystal symmetry and affect the bandstrucutre.[74–76] This method, referred to as strain engineering, has been demonstrated for layered semiconductors by depositing them on flexible substrates followed by stretching or bending of the substrate (Figure 1.5.a).[75] Experimental bandgap changes of over 0.1 eV have been reported for monolayer MoS_2, after straining the material by 1.8% (Figure 1.5.b). However, this behavior is not always desired, as many flexible electronic applications require constant performance regardless of strain. In some instances, the application of an external stimulus–stress, temperature, pressure, electrical potential, etc.–can result in an abrupt phase transformation into a new phase with different electronic properties.[22,77,78] Within the layered semiconductors, this behavior has been observed with the lithiation of MoS_2 and changes in temperature for $MoTe_2$ (Figure 1.5.c).[20,77] In both of these examples, the bandstrucutre of the starting semiconductors is drastically altered resulting in semi-metallic behavior. This type of phase engineering is of great interest for switching applications where metallic-to-insulator transitions are desired.[22,79]

Another common approach for the bandgap engineering of electronic materials is based on the modification of their density of states by reducing their dimensionality. As the

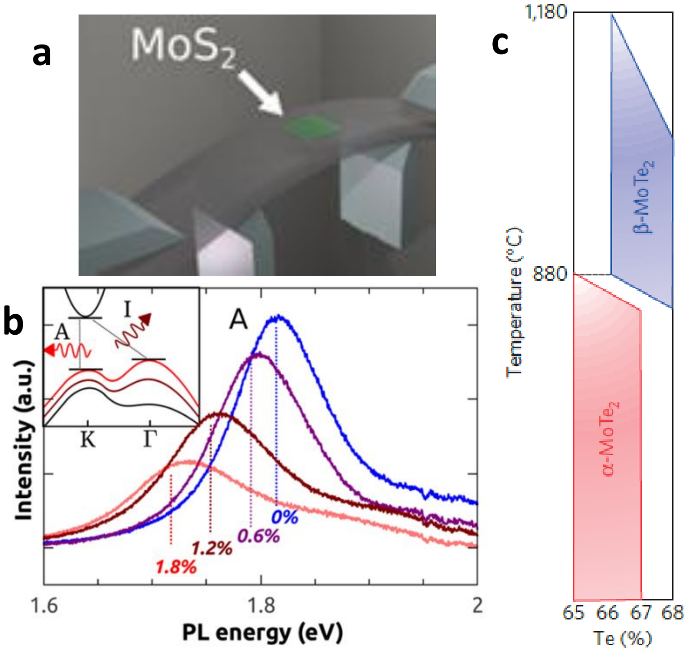

Figure 1.5. **(a)** Illustration of the strain engineering setup for layered materials.[75] **(b)** PL spectra of strained MoS_2. Bandgap change of about 0.1 eV with 1.8% strain.[75] **(c)** Binary Mo-Te phase diagram around the $MoTe_2$ compounds.[77]

dimensionality of the the material decreases, quantum confinement effects become more obvious opening the bandgap.[80] Typically, the density of states near the band extrema for a three-dimensional (3D) material follows a square-root dispersion (Figure 1.6.a).[80] When the material is confined in one direction–thickness bellow 10 nm–it starts behaving as a two-dimensional (2D) material. These thin-films or nanosheets are known as quantum wells and their density-of-states dispersion follows a step-wise distribution that starts at higher energies than the 3D dispersion, opening the bandgap.[80] Layered materials are also often called 2D materials, given their feasibility to grow or exfoliate them down to single-layer crystals with thicknesses below one nanometer. The increase in bandgap energy, as a result of the reduction in the number of layers, has been previously demonstrated numerous times for layered semiconductors. MoS_2, for example, has a bulk indirect bandgap around 1.2 eV, while the monolayer has a direct bandgap around 1.9 eV (Figure 1.6.b).[4] One-dimensional (1D) materials or quantum wires are confined in two directions, where the bandgap opens furthermore and the density of states follow an inverse distribution.[80] While nanowires of layered semiconductors have been grown before, these typically have diameters too large to observe any clear effect of quantum confinement. Interestingly, MoS_2 nanowires with widths below 3 nm have been reported where the bandgap decreases with increasing confinement, which must be due to a different effect.[81] Finally, when the material is confined in every direction, it becomes a zero-dimensional (0D) material or quantum dot. Quantum dots possess the larger bandgap out of all the confined structures with discrete energy states.[80] It is well stablished that quantum dots of layered semiconductors can have considerably large bandgaps, such as 3.3 eV and 3.0 eV for 2.5 nm-GaSe and 10 nm-MoS_2 quantum dots, respectively (Figure 1.6.c and 1.6.d).[82,83]

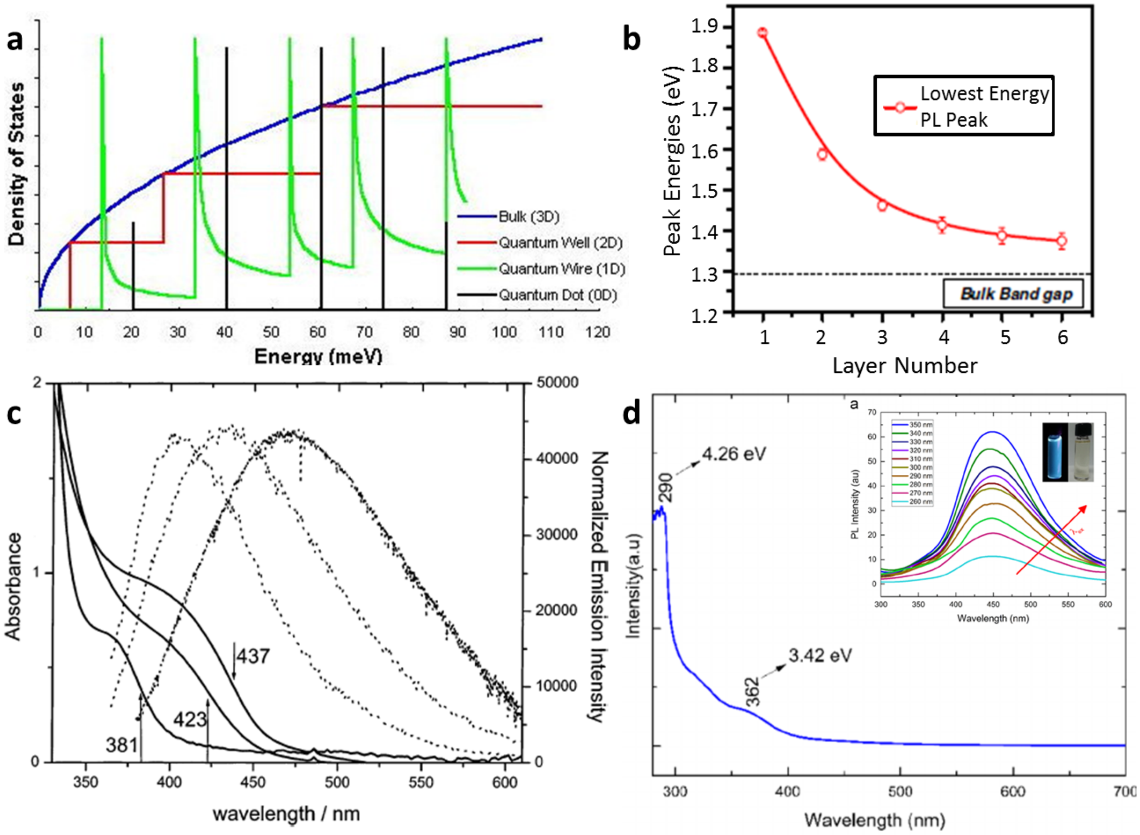

Figure 1.6. (a) Density of states of materials with different degrees of quantum confinement.[80] **(b)** Dependence of the MoS_2 bandgap on the number of layers.[4] **(c)** Optical absorption and photoluminescence of GaSe quantum dots of 2.5, 4 and 9 nm.[82] **(d)** Optical absorption and photoluminescence (inset) of MoS_2 quantum dots of 3.5 nm.[83]

1.4.1 Semiconductor alloying

The third typical approach for bandgap engineering is the alloying of different electronic materials with diverse properties. Generally, alloys are obtained by the substitution of at least one element for a different one with similar size, valence and coordination geometry.[84] This will allow the incorporation of the new element into the original compound throughout the composition range until the substitution is completed. There are numerous examples of these alloys among layered semiconductors, such as: substitution of transition metal in 2H-TMDs ($Mo_{1-x}W_xS_2$, $Mo_{1-x}W_xSe_2$),[85,86] substitution of chalcogenide in 2H-TMDs ($MoS_{2(1-x)}Se_{2x}$, $WS_{2(1-x)}Se_{2x}$),[6,87] substitution of chalcogenide in 1T-TMDs ($HfS_{2(1-x)}Se_{2x}$, $ZrS_{2(1-x)}Se_{2x}$)[27,28] and substitution of chalcogenide in III-VI monochalcogenides ($GaS_{1-x}Se_x$).[36,88] In all of these examples, we observe unlimited solubility of the alloying element into the original compound and a linear change in lattice parameter with composition. For the chalcogenide-substitution alloys the bandgap also exhibits a linear dependency on the composition as predicted by the virtual crystal approximation (VCA) (Figure 1.7.a). However when the transition-metal is substituted, the bandgap exhibits a parabolic or bowing behavior with a minimum around $x = 0.33$ (i.e. 33% of Mo has been substituted by W) (Figure 1.7.b).[85,86,89] This behavior has been

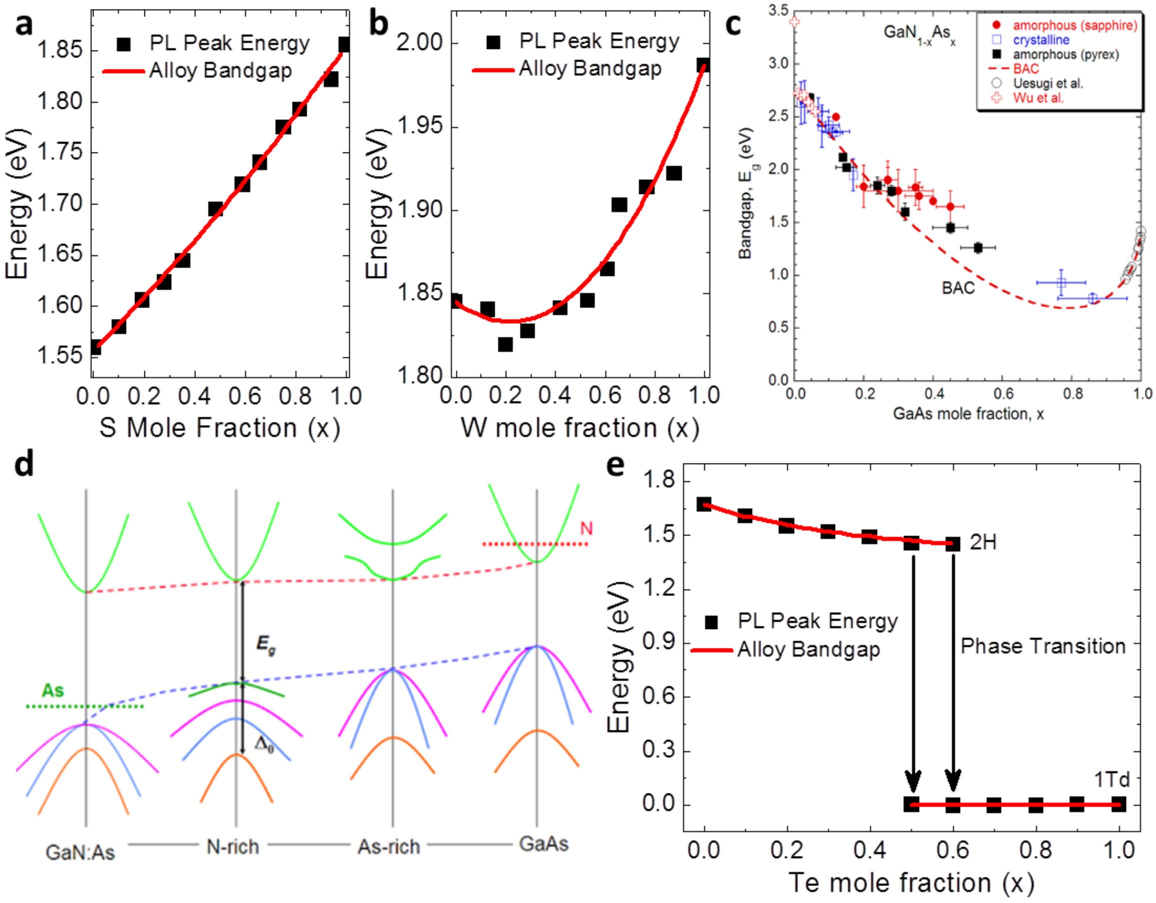

Figure 1.7. (a),(b) Composition-dependent bandgaps of $MoS_{2x}Se_{2(1-x)}$ and $Mo_{1-x}W_xS_2$ monolayers, respectively.[6,85] **(c),(d)** Band anti-crossing (BAC) model and bandgap values for $GaN_{1-x}As_x$, respectively.[84,89] **(e)** Composition-dependent bandgaps of $WSe_{2(1-x)}Te_{2x}$ monolayers, the phase transition from 2H to 1T' is evident.[78]

explained by a relatively linear change of the valence band maximum and an almost exponential change of the conduction band minimum with composition.[89] At low W content, the conduction band minimum is relatively constant as the tungsten *d* orbitals contribution is minimal; after x = 0.33, the tungsten *d* orbitals start dominating the contribution to the conduction band minimum and a large change is observed.

Alloy systems that follow the VCA allow for the precise tuning of the bandgap within the two endpoints. However, deviations from the VCA can result in larger ranges for bandgap tuning, not limited to the endpoints. While alloys are typically obtained by substituting elements of similar size, valence and coordination geometry, often substitution with elements beyond those parameters can yield interesting properties. It has been shown that large bandgap bowings can result from the substitution of elements with considerable size and electronegativity differences.[90,91] In this example, explained by the band anti-crossing model, the incorporated specie starts behaving as a defect impurity in the host material creating defect levels; as the concentration increases, the discrete defect levels merge to form a band. The host material bands and the new band will experience Coulombic repulsion from each other, generating the band anti-crossing structure and modifying the bandgap (Figure 1.7.c and 1.7.d).[84,90]

Alloys between species with different crystal structures are also possible. In this case a phase-transition concentration or concentration range is expected.[30,78,92,93] These alloys can now exhibit smooth bandgap tuning in certain ranges and abrupt transformations in others.[30,78,93] The $WSe_{2(1-x)}Te_{2x}$ alloy is a perfect example, as monolayer 2H-WSe_2 has a bandgap around 1.65 eV and 1T'-WTe_2 is a semimetal. As seen in Figure 1.7.e, with the incorporation of Te the bandgap decreases from 1.65 eV to about 1.45 eV and 1.44 eV for $x = 0.5$ and 0.6, respectively.[78] The phase transformation takes place within the $0.5 \leq x \leq 0.6$ range, where the material becomes a semimetal. While the growth of alloys with multiple crystal structures might be more difficult, the possible properties and applications make them of great interest.

Chapter 2

Bandgap restructuring of gallium telluride in air

The layered nature of TMDs and III-VI monochalcogenides opens the opportunity for novel and unique methods for the bandgap engineering of such semiconductors. In this chapter we explore the consequences of prolonged exposure of GaTe to air, and its effect on the bandstructure. Section 2.1 describes the general sample preparation method utilized in the following experiments. Sections 2.2, 2.3, 2.4 and 2.5 discuss the optical, electrical, surface and structural properties of GaTe after different periods of air exposure, respectively. Section 2.6 presents supporting DFT calculations explaining the observed behavior in the previous sections, and in Section 2.7 a proposed mechanism for the behavior is given. The results presented here showcase how the surfaces of the layers offer a direct route to access and modify the bulk properties, including bandgap, of some layered materials.

2.1 Sample preparation

Single-crystal bulk ingots of GaTe were grown elsewhere by the Bridgman method. In this method, polycrystalline GaTe was heated above its melting point and slowly cooled along a temperature gradient starting from a single-crystal seed at one end, continuously solidifying in the same crystal orientation as the temperature gradient moves along the melted material.[94] The samples were produced by exfoliation using adhesive tape or by peeling with a razor blade. By repeating these procedures and the use of thermal tape, we obtained GaTe flakes with fresh surfaces on both sides. Free-standing bulk flakes with thicknesses ranging from 1 – 50 μm were selected. The samples were exposed to air for different periods of time at ambient conditions before studying their properties.

2.2 Optical properties

Fresh, or as-cleaved, GaTe has characteristic dark-blue highly-reflective surfaces, noticeable to the naked eye. When exposed to air for prolonged periods of time, the surfaces appearance turn into a dull yellow-brown color. The change in appearance of the GaTe flakes, observed through the human eye, can be correlated to changes on several optical properties, discussed below.

2.2.1 Optical Absorption

Optical transmittance and reflectance spectroscopies were obtained within the 0.5 eV – 2 eV range, with a UV-Vis spectrometer. Optical absorbance was calculated with the following equation

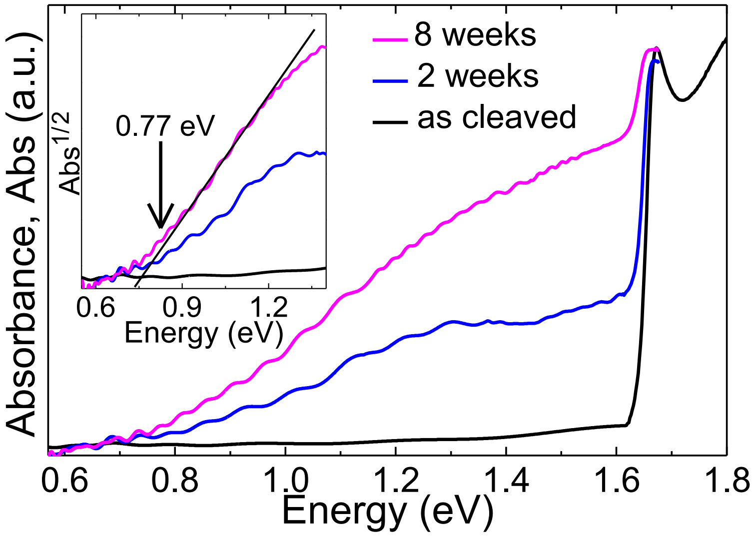

Figure 2.1. Optical absorption spectra of GaTe at different exposure time to air: as-cleaved (black), 2 weeks (blue) and 8 weeks (magenta). The excitonic absorption peak is observed around 1.65 eV. Inset: square root of the absorbance as a function of energy. Linear extrapolation of the square root of absorbance reveals an optical gap of 0.77 eV associated with an indirect bandgap material.

$$Abs(E) = \ln\left(\frac{1-R(E)}{T(E)}\right), \tag{2.1}$$

where $T(E)$ and $R(E)$ are the experimentally determined transmittance and reflectance for a given energy E, respectively.[95,96] From Figure 2.1, for an as-cleaved crystal the sharp absorption edge corresponding to the direct band-to-band transition is observed at ≈1.67 eV. The absorption edge is overlapped by an excitonic peak, with typical binding energy of 18 meV.[39] After exposure to air, the strong absorption of photons with energies below the band edge occurs, and a new absorption edge emerges. The optical absorption around the bandgap typically shows an $E^{1/2}$ and E^2 dependencies for direct and indirect transitions, respectively.[97] This can be seen from the relations between absorbance and absorption coefficient ($\alpha(E)$), and absorption coefficient and direct ($E_g{}^{dir}$) or indirect bandgap ($E_g{}^{ind}$).[95,96,97] The relations are as follow

$$Abs(E) = \alpha(E)t, \tag{2.2}$$

$$\alpha(E) = \alpha_0\left(E - E_g^{dir}\right)^{1/2}, \tag{2.3}$$

$$\alpha(E) \propto \left(E - E_g^{ind} \pm E_p\right)^2, \tag{2.4}$$

where t is the sample thickness, α_o is a material-dependent constant and the absorption coefficient for an indirect transition will depend on the phonon energy (E_p) and weather the phonon is being absorbed or emitted.

From Equations 2.3 and 2.4, the direct and indirect gaps can be obtained by the onset of the square of absorption (Abs^2) or the onset of the square-root of absorption ($Abs^{1/2}$),

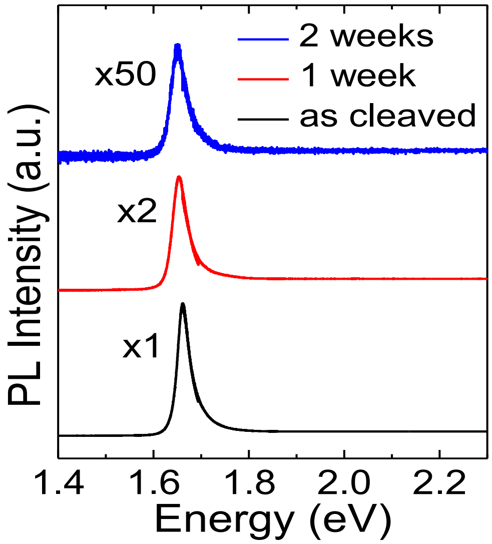

Figure 2.2. Micro-photoluminescence spectra showing that the peak intensity at 1.65 eV decreases over exposure time to air.

respectively. The inset in Figure 2.1, shows the linear relation between the square-root of absorption and energy, characteristic of an indirect transition. From here, we can approximate a new indirect bandgap around 0.77 eV for GaTe exposed to air, less than half of the bandgap of pristine GaTe. This new absorption edge cannot be attributed to the formation of the common oxide-decomposition products TeO_2 or Ga_2O_3 as their bandgaps are ≈3.8 eV and 4.9 eV, respectively.[98,99]

Equation 2.1, used above to calculate the optical absorption of the material, is a simple approximation that assumes no internal light scattering, no back reflection and only and single-pass absorption.[96] However, the layered nature of the material and its high reflectivity causes the material to behave like a Fabry-Pérot interferometer, with multiple internal reflections.[100] This causes the oscillations observed for the 2 weeks (blue) and 8 weeks (magenta) curves in Figure 2.1, where constructive and deconstructive interactions, in both the reflectance and transmittance spectra, take place.

2.2.2 Photoluminescence

The photoluminescence (PL) spectroscopy was obtained at room temperature with a micro-PL setup in a back-reflection geometry, within the range of 1.3 – 2.3 eV. Excitation was done with an argon-ion laser with 488 nm wavelength and 1.3 μm laser spot radius. As seen in Figure 2.2, the as-cleaved sample shows strong excitonic PL emission around 1.65 eV. Over time, exposure to air leads to quenching of the PL signal. Exposure times longer than 20 days lead to the complete disappearance of the peak. Additional near-IR PL was obtained between 0.68 – 1.03 eV with an argon-ion laser and cooled InGaAs detector. No PL signal was measured after any period of air exposure. The absence of photoluminescence within these regions, suggests that prolonged exposure to air can result in the formation of an indirect-bandgap semiconductor. The progressive loss of PL signal over time and the emergence of a sub-bandgap absorption edge are consistent with the formation of an indirect bandgap material at the surface

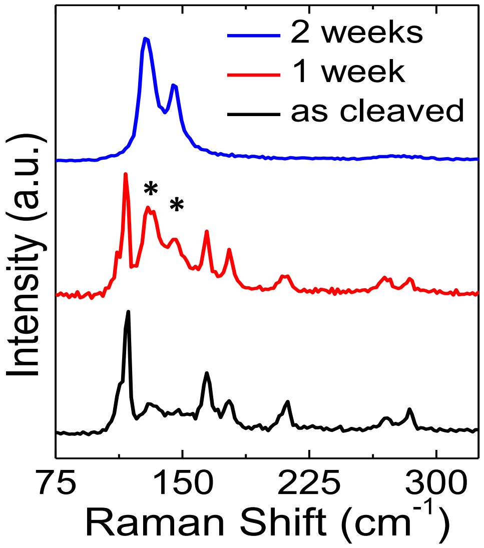

Figure 2.3. Micro-Raman spectra showing the emergence of two Raman peaks at 131 cm^{-1} and 145 cm^{-1}, after sample exposure to air (each indicated by an asterisk for the spectrum measured after one week).

that grows over time. We note that the PL and optical absorption spectra associated with as-cleaved GaTe reappear in samples upon removal of a surface layer via exfoliation. Supporting photomodulated reflectance spectroscopy is available in Appendix A.1

2.2.3 Raman spectroscopy

Raman spectroscopy is an indirect approach to probe the vibrational modes of molecules and crystals.[101] Complementary to IR spectroscopy–which probes the vibrational modes with changes in the dipole moment–Raman spectroscopy probes the vibrational modes with changes on the polarizability. This technique is commonly used as fingerprint to identify semiconductors and to inspect their quality. Narrow peaks are indicative of high-quality crystals, while broad peaks represent some degree of disorder. Blue-shifts and red-shifts of the Raman peaks represent internal strains, leading to the hardening or softening of the corresponding vibrational modes, respectively.[75] For layered semiconductors, this technique is widely utilized as it can easily determine the number of layers in the few-layer regime, based on the collective shifts of their peaks.[18]

Figure 2.3 shows the evolution of the Raman spectrum of exfoliated, or cleaved, single crystals of GaTe after being exposed to air. The peaks at 112, 117, 164, 177, 210, 270 and 283 cm^{-1} observed in the as-cleaved sample have been previously identified for monoclinic GaTe.[60,61,102] With extended exposure to air, two new broad peaks at 131 and 145 cm^{-1} grow until they dominate the Raman spectrum. There is an additional weak peak at around 280 cm^{-1}. Although these new peaks have not been identified for GaTe, they have been attributed to defects or disorder since the peaks are broad.[57,103] As with the PL and optical absorption spectra, the Raman spectrum associated with as-cleaved GaTe reappears in samples upon removal of a surface layer via exfoliation. We note that Raman spectra such as the one in Figure 2.3 (blue curve) have been measured for multilayered crystals with thicknesses ranging from below 10 nm to tens of micrometers. However, it has been speculated that such change in the Raman spectrum

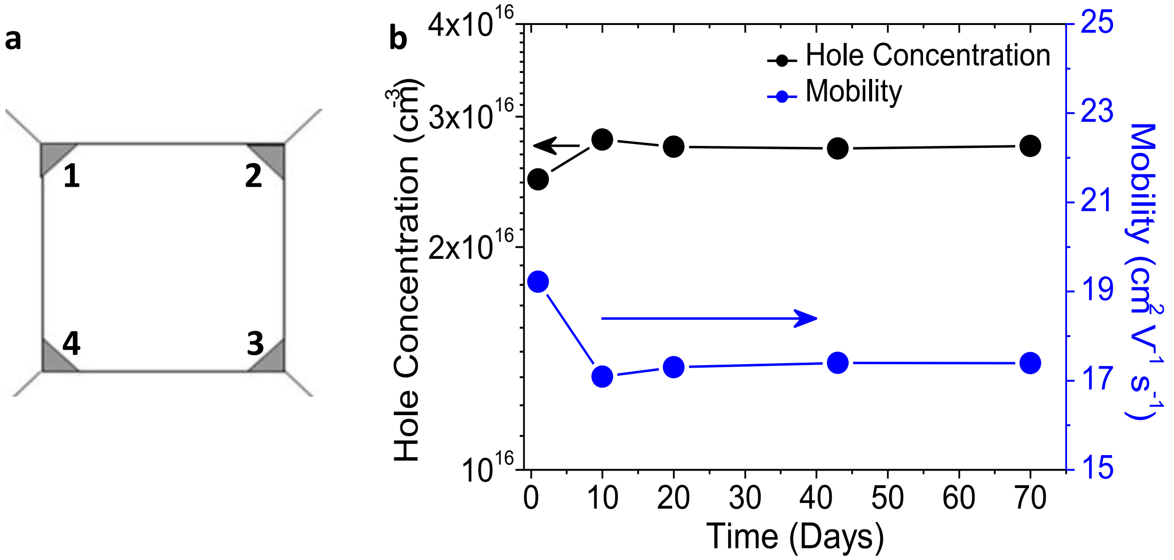

Figure 2.4. (a) Four-point contacts in van der Pauw geometry, contacts 1 – 4 are arranged clockwise. **(b)** Change in the hole concentration and hole mobility of GaTe over time, at room temperature.

may be related to a reduced thickness effect; but no physical basis for this explanation is provided.[70,104]

2.3 Electrical properties

The effect of prolonged air exposure on the electronic transport properties of GaTe was studied. As mentioned on the previous chapter, unintentionally doped GaTe typically behaves as a p-type semiconductor with carrier concentrations around 10^{16} – 10^{17} cm^{-3} and average hole mobility around 30 – 40 cm^2/Vs. For the electronic transport measurements, Cr/Au ohmic contacts were deposited with an electron-beam evaporator on the four corners of square samples to simulate a proper van der Pauw geometry, as seen in Figure 2.4.a.[105] Additionally, for the low-temperature measurements, thin copper wires were bonded to the Cr/Au contacts through indium, to connect the sample outside the low-temperature chamber.

2.3.1 Room-temperature resistivity and Hall effect

Four-point van der Paw-geometry resistivity measurements consist on the application of a current (I) through two adjacent contacts (e.g. I: 1→2) and measurement of the voltage (V) across the other two (e.g. V: 4→3). The resistance (R) can be then calculated from Ohm's law

$$R_{43,12} = V_{43}/I_{12}. \tag{2.5}$$

If the contacts are ohmic, switching polarities should result in similar resistance values, that is $R_{43,12} = R_{34,21}$. Similarly, given the square shape of the sample, opposing sides should reflect similar resistance values by reciprocity (i.e. $R_{43,12} = R_{12,43}$). Typical isotropic samples would also show similar resistance values in the horizontal and vertical directions (i.e. $R_{43,12} = R_{23,14}$). Anisotropic materials like GaTe, show large differences in the resistances between the horizontal and vertical direction, as the direction perpendicular to the *b*-axis has a larger resistance than that along the b-axis.[106] For simplicity, here we will use the average resistance between both directions to calculate the hole mobility. Resistivity (ρ), a material property, is given by the following equation

$$\rho = R\frac{A}{l} \tag{2.6}$$

where A is the cross-sectional area and l is the length. Given that the sample has a square shape (length and width are equal) and a thickness t, the resistivity can be determined by

$$\rho = Rt. \tag{2.7}$$

For a p-type material, resistivity can be expressed in terms of the hole concentration and mobility

$$\rho = (q_e p \mu_h)^{-1}, \tag{2.8}$$

where q_e is the elementary charge, p is the hole concentration and μ_h is the hole mobility.

The carrier concentration can be determined individually by the Hall effect.[80,106] Here, a current is passed diagonally through two contacts in opposing corners (e.g. I: 1→3) and the voltage is measured between the other two contacts (e.g. V: 2→4) while a magnetic field is applied perpendicular to the sample surface (B_z). When the magnetic field is applied, the charge carriers experience Lorentz forces that modify their path.[80] The charges start accumulating perpendicular from the current and magnetic field directions and, thus, inducing a Hall voltage (V_H) between the contacts (contacts 2 and 4 in this example). The carrier concentration can be calculated from the Hall voltage, which for a p-type semiconductor is given by

$$V_H = V_{24} = -\frac{I_{13}B_z}{ptq_e}. \tag{2.9}$$

For a freshly exfoliated sample of GaTe, we found a hole concentration around $2.4\text{x}10^{16}$ cm^{-3} and mobility around 19 $\text{cm}^2\text{V}^{-1}\text{s}^{-1}$. Surprisingly, as the sample was exposed to air, no major changes in the transport properties were observed. After a couple of months, the hole concentration only increased by $2\text{x}10^{15}$ cm^{-3} and the mobility decreased by 2 $\text{cm}^2\text{V}^{-1}\text{s}^{-1}$; it is important to note that these changes are within error as they only reflect a negligible change of 3% increase in the resistivity. The observed behavior in the optical properties, suggested that the transformation started at the surface followed by growth inward where the pristine material is still available. To remove any contribution from the underlying pristine GaTe to the measured transport properties, a fully-transformed sample was obtained. We found that the fully transformed sample remains p-type with a hole concentration and mobility of $9\text{x}10^{15}$ cm^{-3} and 17 $\text{cm}^2\text{V}^{-1}\text{s}^{-1}$, respectively.

2.3.2 Variable-temperature resistance

Four-point van der Pauw-geometry resistance measurements were performed as explained above, in a recirculating liquid-helium low-temperature chamber from 50 K – 300 K. As it can be seen in Figure 2.5, even after 7 weeks the resistance of the sample increases by five to six orders of magnitude, as the temperature is decreased. This is indicative that the sample remains behaving as a semiconductor.[80,106] It can also be seen, how there isn't a significant change in the resistance between 1 and 7 weeks of exposure to air, in contrast to the large

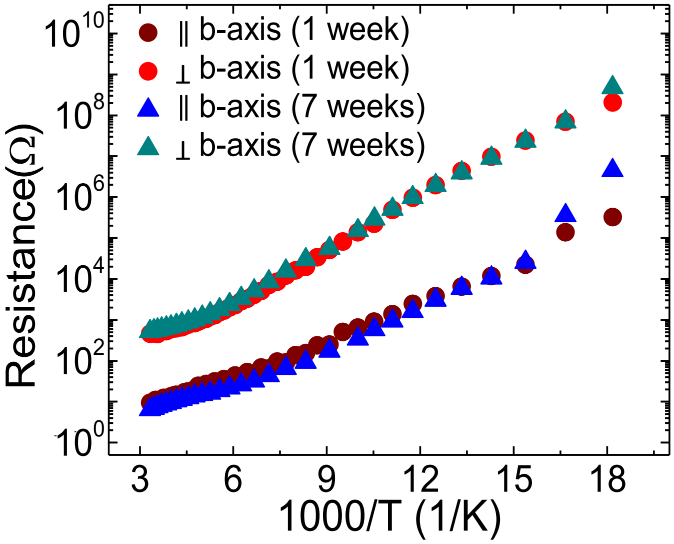

Figure 2.5. Low-temperature resistance of GaTe after 1 and 7 weeks of air exposure. The in-plane electrical anisotropy of GaTe is evident as the resistance of the direction parallel to the *b*-axis is around two to three orders of magnitude lower.

changes observed in the optical properties. This means that the observed transformation is responsible for drastic changes in the optical properties, but not in the electrical properties. Finally in this figure, it is clear the large difference in resistance between the direction parallel and perpendicular to the *b*-axis on the layer plane. At room temperature, the resistance difference is just below two orders of magnitude, while at lower temperatures it can exceed the three orders of magnitude.

2.4 Surface properties

The surface properties of GaTe throughout the transformation process were also studied. It was found that GaTe remains smooth and layered after extended exposure to air as reflected by only a small increase in root mean square (RMS) roughness from 0.3 to 0.7 nm. Unlike the oxidation process of other layered materials that exhibit a large increase in surface roughness.[107] The oxidation state of the surface was probed with x-ray photoelectron spectroscopy (XPS) after different periods of air exposure. XPS results were obtained mainly by one of our collaborators Dr. Changhyun Ko, a postdoctoral researcher at University of California, Berkeley. Details on the measurement and analysis can be found in Appendix A.2. Spectra show the partial oxidation of Te and Ga, which can be attributed to the formation of a native oxide at the surface and/or to the participation of oxygen in the proposed transformation.[108,109] Importantly, even upon extended exposure to air, the peaks associated with unoxidized Te (at 583.5 and 573.5 eV) persist.

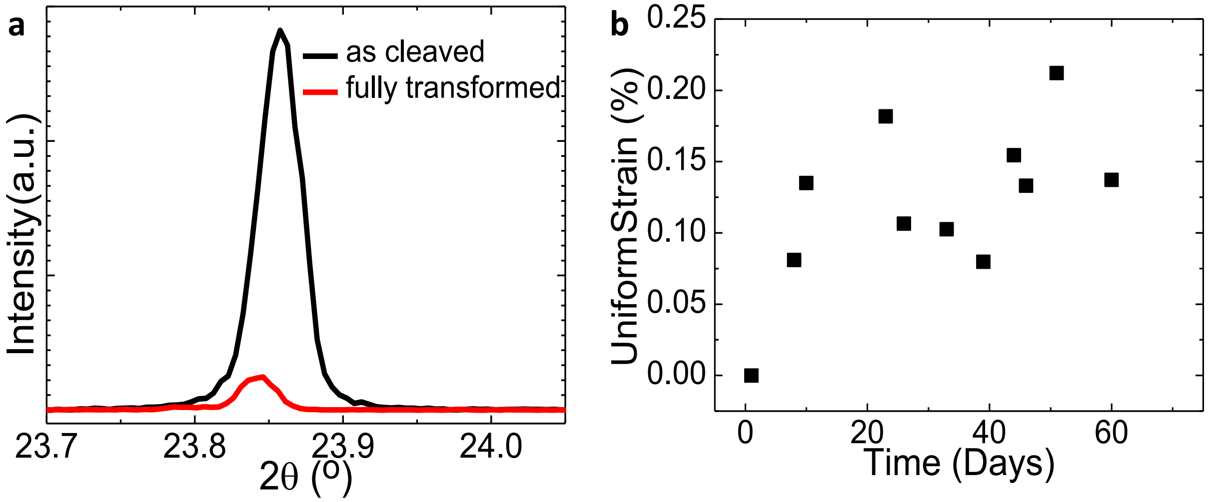

Figure 2.6. (a) ($\bar{4}$ 0 2) X-ray diffraction peak before (black) and after (red) sample transformation in air. **(b)** Uniform lattice strain along the *c*-plane as a function of time for several samples.

2.5 Structural evolution

The structural changes in GaTe as a function of exposure time were studied by x-ray diffraction (XRD). The crystals were oriented with the {$\bar{2}$ 0 1} family of planes scattering in the instrument's out-of-plane direction. Given the layered nature of GaTe, we expect these planes to demonstrate the greatest structural change should species from air incorporate between layers. As a result, we focused on the most intense peak of this family, the ($\bar{4}$ 0 2) peak. These results were obtained mainly by our collaborator Annabel R. Chew, a graduate student in the Salleo group at Stanford University. Further details on the experimental procedures can be found in the Appendix B.1.

2.5.1 Uniform strain evolution

For the fully transformed sample, the ($\bar{4}$ 0 2) peak displays a diffraction intensity one order of magnitude lower than as-cleaved GaTe (Figure 2.6.a). The loss in intensity is indicative of some structural transformation. Simultaneously, the ($\bar{4}$ 0 2) peak of the fully transformed sample is shifted to smaller 2θ values by 0.01°, suggesting that the transformation results in a small increase in interplanar spacing. High-resolution XRD scans of the ($\bar{4}$ 0 2) peak in multiple samples were measured as a function of sample exposure time to air. The data demonstrate a clear increase in the out-of-plane lattice spacing that reaches a lattice strain as high as 0.2% (Figure 2.6.b). This suggests the incorporation of species between GaTe layers, expanding the lattice in the [$\bar{2}$ 0 1] direction.

2.5.2 Non-uniform strain evolution

Detailed analysis of the evolution of interplanar strain can be achieved by studying the strain depth profile and the non-uniform strain in the samples with increased air exposure time. Nondestructive depth profiling of the samples was carried out by monitoring the ($\bar{4}$ 0 2) peak

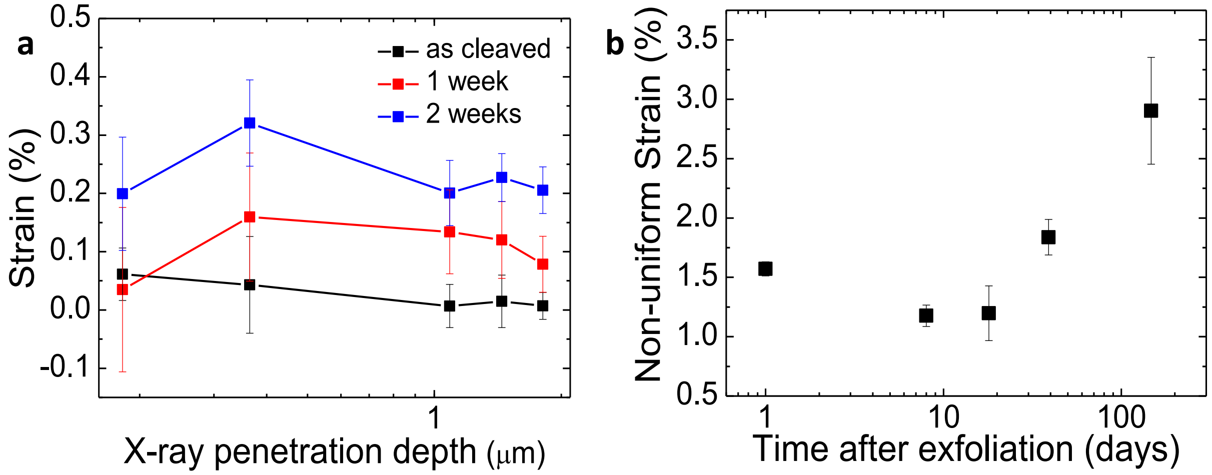

Figure 2.7. (a) Lattice strain present in the GaTe flake upon further oxygen intercalation with time, as a function of x-ray penetration depth. **(b)** Non-uniform lattice strain along the *c*-plane as a function of time.

through grazing incidence x-ray diffraction (GIXD).[110,111] Varying the x-ray incident angle allowed the probing of different depths in the GaTe sample. From Figure 2.7.a, it is seen that in a freshly cleaved sample only a small amount of strain is observed right at the surface, with no strain in the bulk. The surface strain can be caused by defects created during exfoliation (e.g. stacking defects, step edges, etc.) and the initial incorporation of air species into the interlayer spacing, through such defects. After a week of air exposure, the peak strain in the sample is no longer at the surface but between 300 – 400 nm below the surface, indicating an accumulation of air species in the subsurface of the material. The strain relaxation right at the surface could imply some type of surface reconstruction. For depths beyond 1 μm, the strain profile seems relatively uniform with a constant increase in strain over time, where the species diffusion and the transformation are considerably slower. The strain values measured at these depths perfectly agree with the uniform strain values presented above.

Peak broadening analysis on the $\{\bar{2}\ 0\ 1\}$ family of planes, showed a linear increase in peak width with increasing peak order, details in Appendix B.1.[112,113] This relation is indicative of non-uniform strain–variation in interplanar spacing between adjacent regions. The non-uniform strain was determined with the Williamson-Hall analysis and presented in Figure 2.7.b.[113] Initial non-uniform strain could have similarly been caused by surface defects created during exfoliation and local stacking defects during crystal growth. After 1 to 2 weeks of air exposure, the non-uniform strain decreases as the air species incorporate through the layers, reducing the local strains and increasing the average strain at different depths. After prolonged exposure to air, when the uniform strain saturates, the non-uniform strain increases up to twice the initial value. Meaning that after about 20 days, the air species start accumulating in specific areas increasing the local strain to over one order of magnitude higher than the uniform strain.

2.5.3 Long-term grain reorientation

To better visualize the reason for the loss in $(\bar{4}\ 0\ 2)$ diffraction intensity, reciprocal space maps in samples of different exposure times to air were obtained (Figure 2.8.a-c). Reciprocal

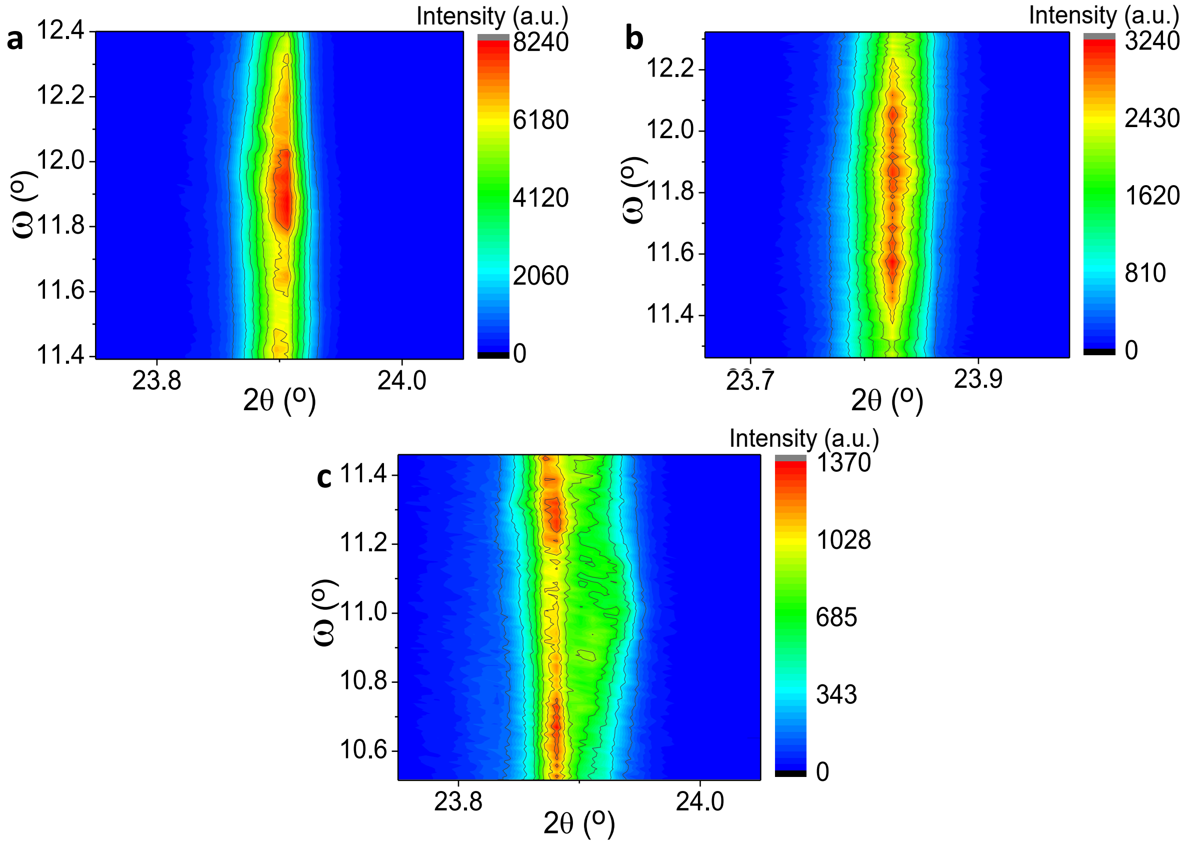

Figure 2.8. Reciprocal space maps of the $(\bar{4}\ 0\ 2)$ diffraction peak for **(a)** as-cleaved sample, **(b)** sample expose to air for 3 weeks and **(c)** for one year.

space maps provide additional information about the orientation of the surface (ω) and distribution of lattice spacing within the crystal (2θ).[114] We observed broadening of the surface orientation with increasing exposure time, creating an almost bimodal distribution after one year. Such redistribution of orientation signifies typically an increase in structural disorder as well as buckling, or rippling. It was estimated that the degree of surface reorientation after one month was less than 2 %, while for the fully transformed sample was above 50 %.

2.6 Density functional theory calculations

The intercalation of species in air was demonstrated with the XRD measurements. To identify which specie is responsible for the observed transformation, we have done density functional theory (DFT) calculations predicting the effects of the intercalation and chemisorption of species like molecular oxygen, water and hydroxyl groups on the bandstructure of GaTe. As a starting point, the bandstructure and partial density of states (PDOS) of GaTe were calculated first. The calculated bandstructure of GaTe has a direct bandgap of 1.72 eV at the *M*-point (Figure 2.9.a). This value is still below the extrapolated 1.8 eV at 0 K[115] but is a better approximation than those reported elsewhere.[58,65,116] The contribution of the orbitals to the PDOS of GaTe can be seen in Figure 2.10.a, where the valence band is composed mostly of Ga-4*p* and Te-5*p* orbitals, while the conduction band is composed mostly of Ga-4*s*, Te-5*p* and

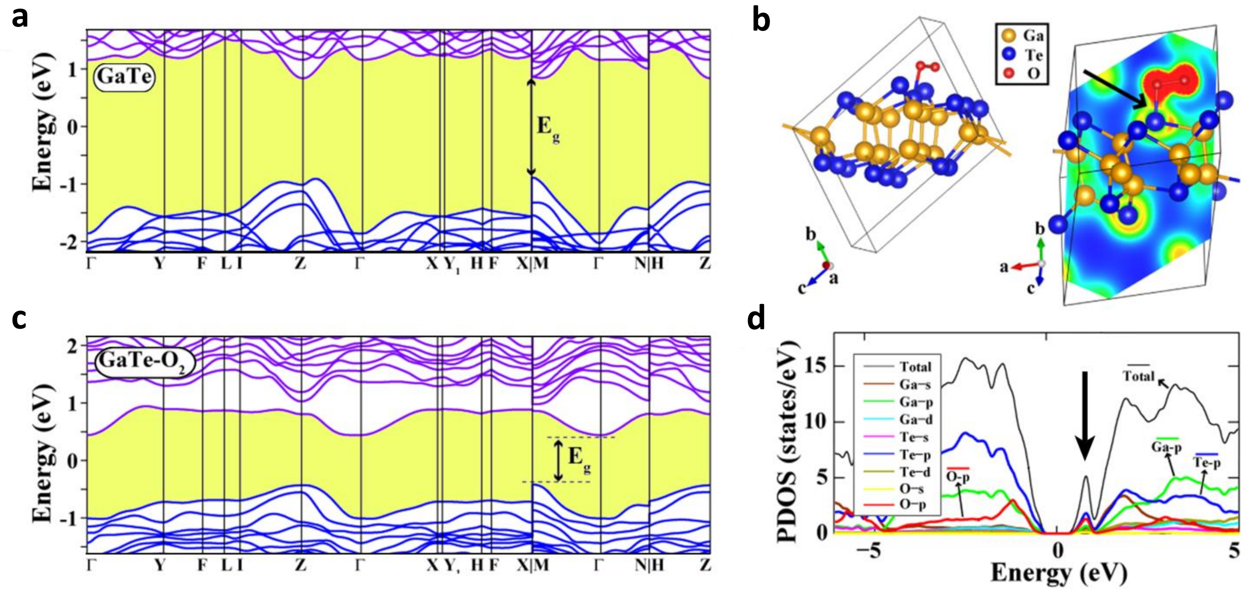

Figure 2.9. (a) Calculated bandstructure of monoclinic GaTe along high-symmetry lines. Bandgap as a function of direction is shaded. The zero of energy was set to Fermi level. Calculations were performed in 2x1x1 supercell. **(b)** Atomic structure and charge density profile of oxygen molecule chemisorbed to GaTe. The new bond formed between a Te atom and an oxygen molecule is indicated by an arrow. **(c)** Calculated band structure for O_2-chemisorbed GaTe. **(d)** Total and orbital projected density of states of GaTe–O_2 near the band gap, showing the new conduction sub-band.

some Ga-4*p* orbitals. In addition, the GaTe Raman-active modes were calculated and agree with our experimental data (see Appendix A.3) as well as published values.[60,61] These results were obtained mainly by one of our collaborators Dr. Mehmet Topsakal. Further details on the experimental procedures can be found in the Appendix B.2.

2.6.1 Bandstructure and density of states of GaTe–O_2 phase

The incorporation of molecular oxygen to the GaTe structure was studied first. This structure from hence forward will be referred to as GaTe–O_2. The optimized GaTe–O_2 structure, shows that O_2 binds preferentially to the Te atoms whose lone pairs are less hindered (perpendicular to the layer, Te_3 in Figure 1.4.b) as depicted in Figure 2.9.b. Isosurface charge density of GaTe–O_2 for a plane passing through the oxygen atoms and their nearest neighbor Te clearly shows the interaction between GaTe and O_2. In order to simplify the calculations, one chemisorbed oxygen molecule was added to each unit cell (GaTe–O_2) although a less-concentrated random distribution of oxygen molecules would be expected. Figures 2.9.c,d show the corresponding bandstructure and PDOS for GaTe–O_2, where a significant restructuring of the conduction band takes place. The new conduction band minimum is now located at the *Γ*-point, making GaTe–O_2 a semiconductor with an indirect bandgap of 0.86 eV.

As shown in Figures 2.9.c,d and 2.10.b, the hybridization of the O-2*p* states with the valance orbitals in GaTe contributes to the formation of two new sub-bands associated with the conduction band. These two new sub-bands are most relevant in giving GaTe–O_2 its distinct

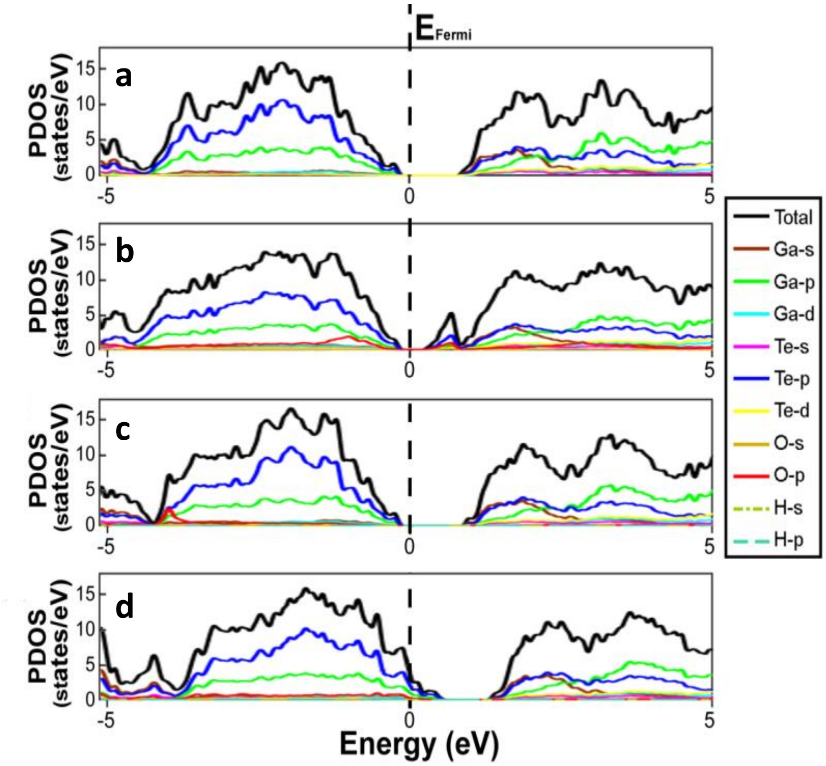

Figure 2.10. DFT calculation of total and atom partial density of states of **a,** GaTe, **b,** GaTe–O_2, **c,** GaTe–H_2O and **d,** GaTe–OH. Zero of the energy was set to the Fermi level.

optical properties. The low-lying sub-band, which gives rise to the new conduction band minimum at the *Γ*-point, is composed mainly of Te-5*p* and O-2*p* states. Because oxygen chemisorption most strongly affects the conduction band, the oxygen-chemisorbed phase would display electrical p-type properties similar to as-exfoliated GaTe. While it is rather fortuitous that the calculated gap for GaTe and GaTe–O_2 match remarkably well with the measured gaps, we focus on the consistency of the calculated and experimental bandgaps in indicating a transformation from direct to indirect and a reduction in the magnitude by about half. Further, although we expect that oxygen molecules chemisorb randomly over a Te-terminated surface, the salient features of our calculations are not expected to change with such randomness.

The Raman-active modes of GaTe–O_2 were also calculated. Three of the Raman-active modes found, located around 130, 146 and 183 cm^{-1}, are in excellent agreement with the three Raman peaks observed in the samples after the transformation (see Appendix A.3). The measured peaks are broad, suggesting that oxygen induces a high level of disorder even as the transformed film remains layered. This is consistent with XRD as discussed above.

2.6.2 Density of states of functionalized GaTe

Based on the previous results, the observed transformation in GaTe seems to be caused by the intercalation and chemisorption of oxygen, forming the GaTe–O_2 phase. To discard any other possible specie present in air (that can also form the Te–O bonds observed by XPS), the

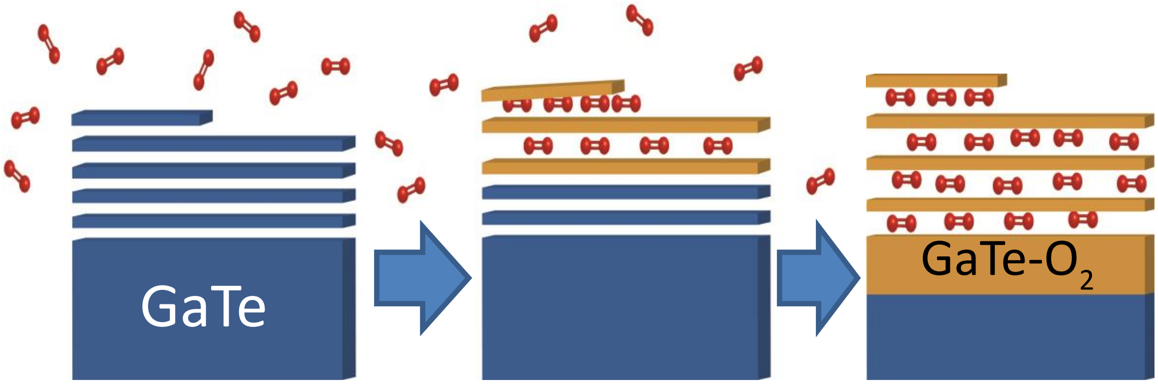

Figure 2.11. Proposed mechanism for the intercalation and chemisorption of oxygen, inducing the formation of the GaTe–O_2 phase.

effect of the chemisorption of water and hydroxyl groups on the PDOS was calculated. Similarly, these structures will be referred to as GaTe–H_2O and GaTe–OH, respectively. We note that DFT calculations for GaTe–H_2O did not revealed any major changes to the bandstructure of GaTe (Figure 2.10.c), indicative of a weak electronic interaction. On the other hand, calculations for GaTe–OH reveal a metallic phase where the Fermi energy lies within the valence band, as seen Figure 2.10.d. However, as indicated in Section 2.3.2 and shown in Figure 2.5, the transformed samples remain semiconducting, consistent with the GaTe–O_2 structure and not the metallic GaTe–OH phase.

2.7 Proposed mechanism

Here, I discuss the proposed mechanism responsible for the transformation of GaTe after prolonged exposures to air. We start with a mechanically exfoliated sample that exhibits optical, electrical and surface properties characteristic of pristine GaTe. However, during the mechanical exfoliation, stacking and surface defects were generated–like the one illustrated at the surface of the schematic in Figure 2.11 (left)–resulting in the surface strain observed by XRD for a freshly cleaved sample. These defects will facilitate the intercalation and diffusion of gas species in air through the layers. This would imply that GaTe samples with pristine surfaces should be more resistant to the transformation, which will be discussed in the following chapter. As oxygen starts intercalating and chemisorbing, the new indirect band edge starts forming. Throughout the first couple of weeks, the oxygen concentrates around 300 – 400 nm below the surface, while slowly diffusing inward (Figure 2.11 (center)). During this period, the increasing amount of intercalated oxygen helps to reduced localized strains–possibly the result of defects generated during crystal growth–by uniformly increasing the interlayer spacing. Finally, after a couple of weeks, oxygen starts accumulating in different areas, creating pockets of high local strain. By this time, the GaTe–O_2 layer is thick enough to quench the PL from the underlying GaTe and the new indirect absorption edge at around 0.8 eV is readily measurable, as represented by Figure 2.11 (right).

Chapter 3

Controlling the transformation of gallium telluride in air

In the previous chapter we presented the transformation that occurs in GaTe when it is exposed to air for prolonged periods of time. This transformation is responsible for a direct-to-indirect gap transition, reducing the bandgap from 1.67 eV to about 0.77 eV. This new phase, formed after the intercalation and chemisorption of oxygen between the layers of GaTe, is referred to as GaTe–O_2. Given that the transformation occurs with at least the presence of oxygen in air and it's facilitated by surface defects, the rate of transformation could be controlled by adjusting the ambient conditions and surface quality. Other species present in air might also play a role in the transformation; in fact, it will be shown that oxygen alone cannot carry out the transformation and some water is needed to catalyze the reaction. This chapter will focus in the study of different approaches to control the transformation. Section 3.1 centers in several methods capable of substantially delaying the transformation. In contrast, Section 3.2 discusses a method to accelerate the transformation process. Finally, Section 3.3 showcases the capability to partially reverse the transformation, recovering regions with properties similar to pristine GaTe.

3.1 Delaying the transformation

Being able to delay the transformation is of upmost importance if GaTe is intended to be used in a real life application subject to environmental conditions. While the electrical properties don't seem to change significantly, the optical properties do; this could greatly affect the performance of a device where GaTe is being employed. The most common approach to prevent environmental degradation of multiple materials is to physically isolate the material from any potential reacting specie.[117–120] As it can be seen in the red curves in Figures 3.1.a,b, storing the GaTe sample in vacuum ($<1x10^{-7}$ torr) substantially delays the transformation. After 2 weeks in vacuum, no noticeable change in either the PL intensity or Raman spectrum is seen, in clear contrast with the changes observed in Figures 2.2 and 2.3. However, keeping the sample continuously in vacuum is not practical for real life applications. This hurdle is commonly overcome by physically capping the material. Environmentally sensitive materials in different applications (e.g. lithium in Li-ion batteries, perovskites in solar cells) are continuously used in real life by sealing them from the environment.[117,118] It has been shown that by capping GaTe flakes with thin-films, such like aluminum oxide (Al_2O_3), the pristine GaTe properties are preserved.[120]

It was also found that by storing the GaTe samples in a flowing dry nitrogen environment at ambient pressure, the transformation was delayed. While no vacuum was used to remove the oxygen present, the constant flow of nitrogen flushed most of the air out of the chamber, preventing the transformation. Similar results were observed when humid nitrogen was flowed

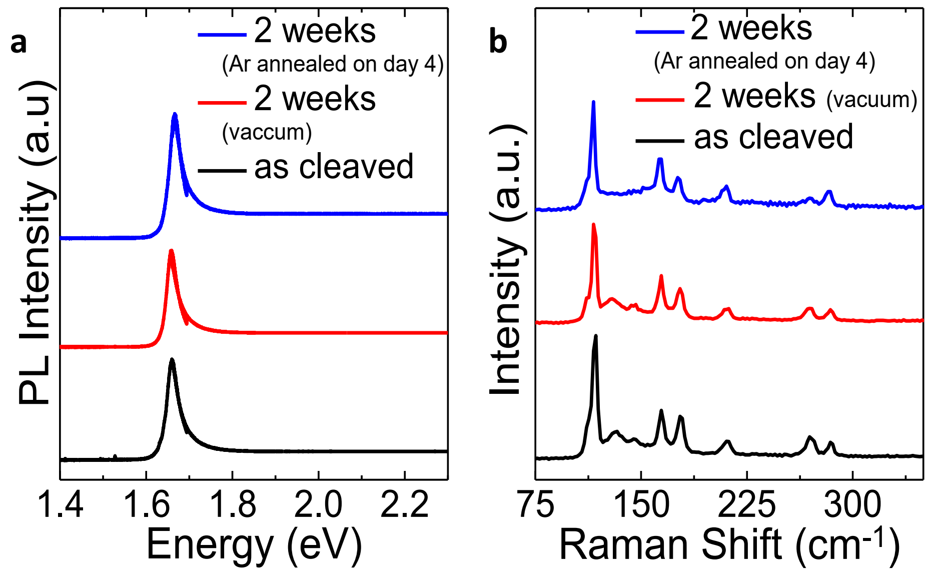

Figure 3.1. (a) PL spectra and **(b)** Raman spectra of freshly cleaved GaTe (black), GaTe stored in vacuum for 2 weeks (red) and GaTe stored in air for 2 weeks after being annealed in argon on the fourth day.

into the storage chamber. The humid nitrogen was obtained by flowing dry nitrogen through a bubbler with deionized water (diH_2O); after about 45 minutes of purging the dissolved oxygen from the water, the humid nitrogen was then flowed into the chamber.[121] This result clearly indicates that water vapor alone isn't responsible for the transformation. Surprisingly, flowing dry air into the chamber did not result in any observable transformation either. From these results, we can conclude that the transformation needs both oxygen and water to takes place, similar to other oxidation mechanisms.[107] Therefore, while oxygen seems to be responsible for the changes to the bandstructure and optical properties, water appears to catalyze the transformation reaction.

As mentioned above, it is suspected that surface defects–mainly generated during the mechanical exfoliation–facilitate the intercalation and diffusion of oxygen molecules between the GaTe layers, accelerating the transformation. This would imply that higher-quality surfaces would delay or prevent the transformation to occur. Mechanically exfoliated GaTe samples were annealed in argon at 250 °C for 5 hours, four days after being exfoliated and stored in air. Figures 3.1.a,b show the PL and Raman spectra (blue) of these samples after 2 weeks of being exfoliated. The strong PL peak and the characteristic GaTe Raman peaks are still visible. In fact, the intensity of the PL peak was higher than that of the freshly cleaved sample and the small 131 and 145 cm^{-1} GaTe–O_2 Raman peaks observed in the freshly cleaved sample have disappeared. This shows that by annealing the samples earlier on the transformation, the surface and stacking defects are being healed, significantly delaying the transformation. Even more, it seems that the annealing process is able to reverse the initial transformation by driving the gas species out of the material. In Chapter 5, I discuss the vapor growth of GaTe and $GaSe_xTe_{1-x}$ alloys, but it is important to note here that vapor-grown GaTe crystals exhibit strong photoluminescence at 1.65 eV up to seven months after growth. The as-grown GaTe crystals would have higher-quality

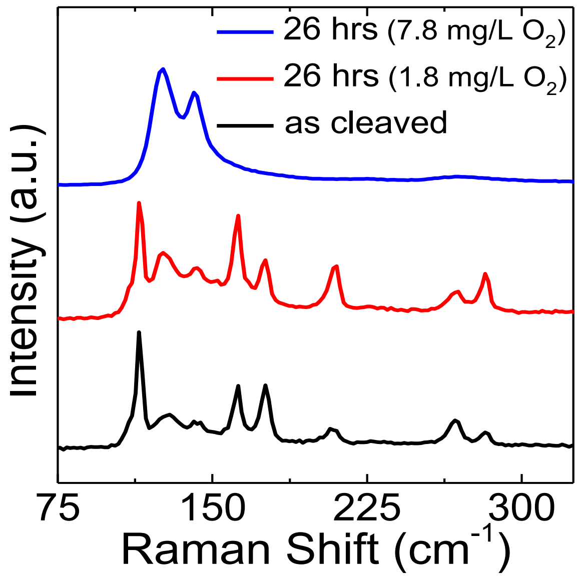

Figure 3.2. Raman spectra of GaTe stored in de-ionized water with different concentrations of dissolved oxygen. Samples submersed for 26 hours in more oxygenated (blue) and less oxygenated (red) water are compared to as-cleaved GaTe (black). A difference in oxygen concentration between 1.82 and 7.82 mg of O_2 per liter of water results in a significant change in Raman spectrum.

surfaces than mechanically exfoliated samples, thus confirming the role of defects in facilitating the transformation.

3.2 Accelerating the transformation

GaTe–O_2 behaves as a p-type semiconductor with an indirect bandgap around 0.77 eV and similar electronic transport properties as GaTe. These properties can be attractive for certain applications in the near-IR spectrum. As such, methods to accelerate the transformation might be ideal for the design of GaTe–O_2 devices. It was determined above, that both oxygen and water are essential for the transformation to occur. Here we explore the approach of submerging GaTe in water with different dissolved-oxygen concentrations, as a direct method to accelerate the transformation process. Deionized water and nitrogen-purged diH_2O were used for these experiments. It has been shown that after 40 - 50 minutes of nitrogen purging at room temperature, the decay of dissolved-oxygen content in water plateaus.[121] Thus for the nitrogen-purged diH_2O, an initial purging period of 45 minutes was allowed before submerging the samples. The samples were then kept in water under constant nitrogen purging to maintain the current dissolved-oxygen level. The oxygen content in water was determined with a polarographic dissolved-oxygen meter electrode. It was determined that the oxygen content in diH_2O and nitrogen-purged diH_2O were about 7.8 mg/L and 1.8 mg/L, respectively. This work was performed in collaboration with group member Alan Lin.

Figure 3.2 shows the difference in transformation rate between the samples submerged in both environments after just 1 day. It is clear that the transformation of GaTe displays a strong dependence on the concentration of dissolved-oxygen in water. A lower level of dissolved-

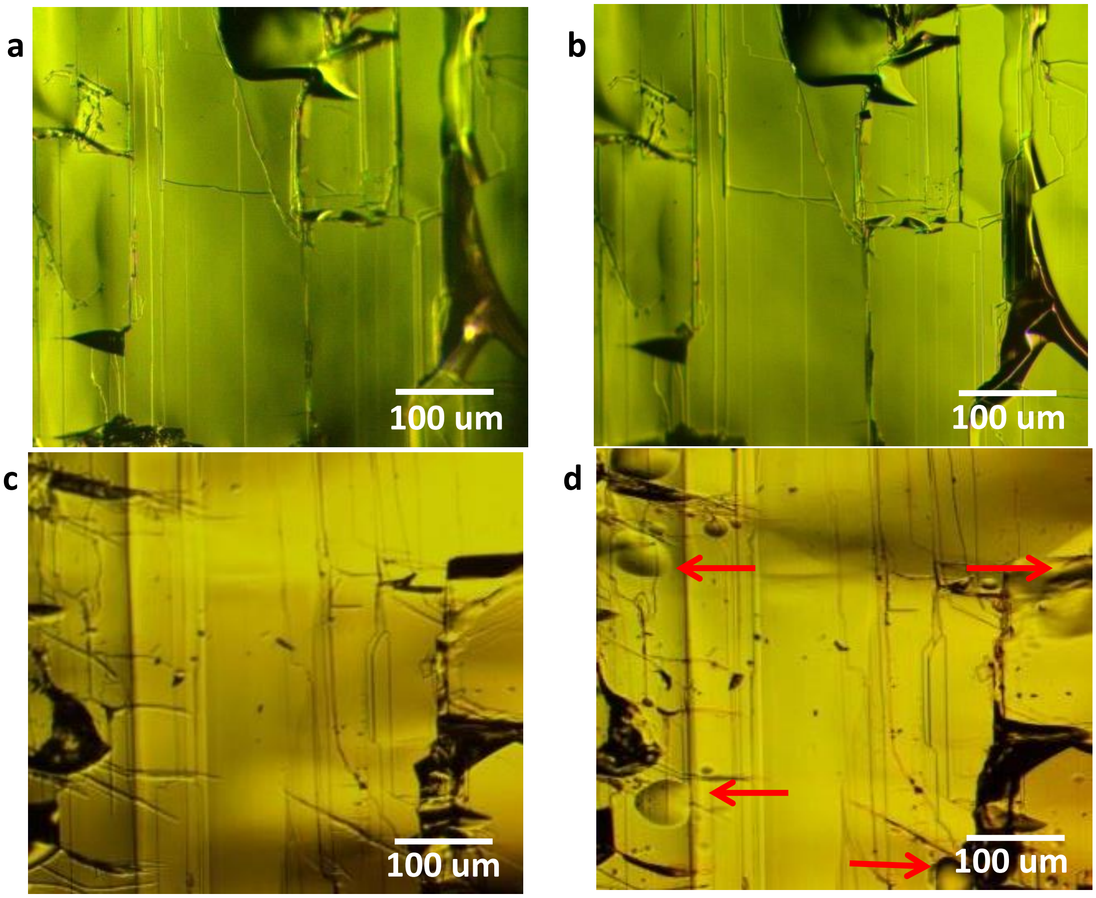

Figure 3.3. Optical micrographs of freshly cleaved GaTe **(a)** before and **(b)** after rapid thermal annealing at 300 °C for 5 min in nitrogen. No major change is observed. Optical micrographs of transformed GaTe **(c)** before and **(d)** after rapid thermal annealing at 300 °C for 5 min in nitrogen. Several bubbles under the surface (indicated with red arrows) were formed during thermal annealing.

oxygen leads to a slower rate of change in optical properties. When compared to the transformation rate observed for GaTe samples stored in air, it was found that samples submerged in nitrogen-purged diH_2O transformed about 60 % faster, while samples stored in regular diH_2O transformed about 46 times (4,500 %) faster. These results prove the effectivity of the proposed method to accelerate the transformation process of GaTe. However, greater control on the dissolved-oxygen level would be ideal to precisely tune the transformation rate.

3.3 Partial reversibility

Bandgap engineering methods, like the ones discussed in Section 1.3, typically are fixed and non-reversible. Semiconductor alloys and quantumly confined structures can’t recover their original properties once they have been grown. Reversible strain engineering can be achieved through setups similar to the one shown in Figure 1.5.a, where the curvature of the substrate can be controlled and reversed. Naturally, reversible bandgap engineering is most commonly employed on switching applications, where metallic-to-insulator or metallic-to-semiconductor transitions are desired.[122,123] These transitions are triggered by some external stimulus like

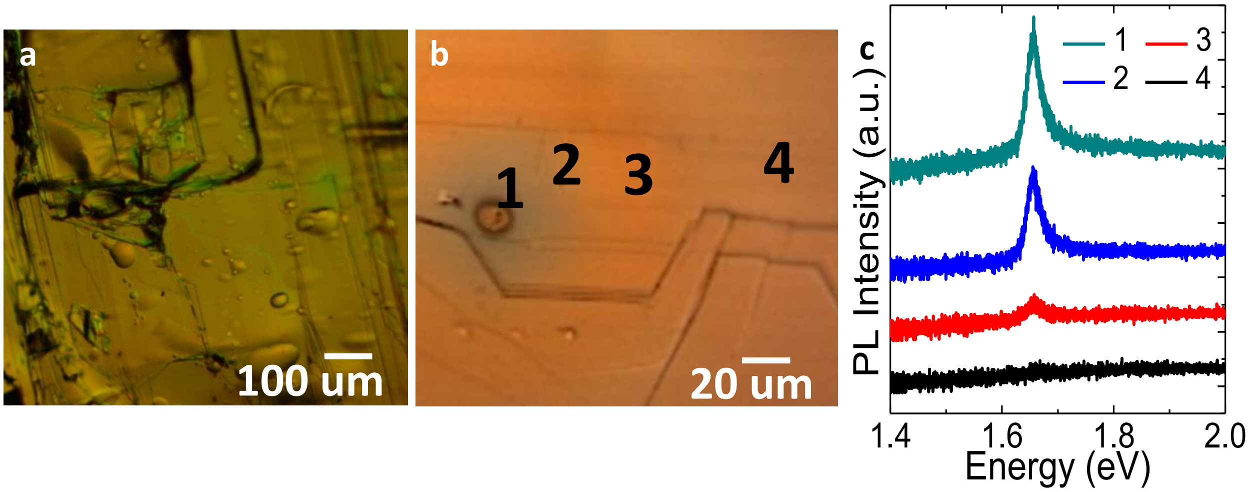

Figure 3.4. (a) Optical micrograph of transformed GaTe, exposed to air for 3 weeks, after rapid thermal annealing at 500 °C for 5 min in nitrogen gas. Numerous bubble-like features and green-colored regions at cracks and other imperfections are observed. **(b)** Optical micrograph of an area around a bubble that formed and burst upon annealing. The burst bubble is surrounded by a green "halo". **(c)** Micro-PL spectra in different regions near the burst bubble in **(b)**. The radius of the PL spot was 1.3 µm.

stress, temperature or electrical potential.[122,124,125]

Here I explore the possibility of reversing the transformation process from GaTe–O_2 back to GaTe. If a species such as oxygen has been adsorbed between the layers of GaTe, one may expect thermal annealing to drive out such species, thus restoring the properties of the sample to its as-cleaved state. As discussed in Section 3.1, this is precisely what it seems to occur when the GaTe samples are annealed in argon at 250 °C for 5 hours, four days after being exfoliated and stored in air. This annealing process not only helped healing the defects present on the surface delaying the reaction, but it appeared to reverse the initial transformation improving the photoluminescence emission and Raman spectrum quality. We expect that just as the thermal annealing was able to reverse the transformation at the initial stages, some degree of the transformation should also be reversed after prolonged exposure to air.

Rapid thermal annealing was done on several GaTe samples to observe the effects of annealing between a freshly cleaved sample and a transformed one. Figures 3.3.a,c show optical microscope images of the surface of a freshly cleaved sample and a transformed one, respectively. The green color is characteristic of pristine GaTe when observed under an optical microscope with the default settings and without filters; similarly, the yellow color is characteristic of transformed GaTe–O_2. Figures 3.3.b,d show the same samples right after rapid thermal annealing at 300 °C for 5 minutes in nitrogen. For the freshly cleaved sample, no major change is observed. On the transformed sample, we observe the formation of several bubble-like gas pocket areas, confirming the presence of gas species–like oxygen–intercalated and trapped between the GaTe layers. In the proposed scenario—in which oxygen chemisorbs to Te—bubbles may form by the unbinding and collection of oxygen present between the GaTe layers. Figure 3.4.a shows the result of rapid thermal annealing a transformed sample at a higher temperature (500 °C) for 5 minutes in nitrogen. Now one observes a larger density of bubble-like features in the surface as well as the emergence of green-colored regions near cracks, step edges, burst bubbles and other surface imperfections. As mentioned above, the green color is characteristic of pristine GaTe, suggesting that partial reversibility of the transformation was achieved. At this higher temperature, a larger concentration of oxygen desorbed resulting in a large density of bubble-like features and the partial reversibility of the transformation due to the local release of the adsorbed species through surface imperfections.

In an attempt to increase the local areas that exhibit the partial reversibility, an extended thermal annealing was carried out at 450 °C for 12 hours in argon. As expected, the annealing process revealed green-colored areas around surface defects and burst bubbles. Figure 3.4.b shows one of such burst bubbles and the surrounding green-colored halo-like area. The optical microscope image shown in Figure 3.4.b was taken with a different microscope and settings causing the differences in colors. Measurement of the PL spectrum in the vicinity of the burst bubble reveals the partial recovery of the 1.65 eV peak, that increases in intensity as it approaches the center of the burst bubble. The recovery of the PL peak is indicative of the partial reversibility of the transformation. While the reversibility of the transformation is still constrained to localized areas near surface imperfections or burst bubbles, the results presented here should prove the viability of such reversible process. In the future, it would be of interest to find the ideal annealing conditions that would maximize the reversibility, and to determine if there is a critical air-exposure time threshold that prevents completion of the process.

Chapter 4

Band-edges alignment and shallow-defects levels

Gallium telluride is an attractive direct-gap layered semiconductor with p-type transport properties. However, the successful integration of GaTe in devices will also depend on the alignment of its bandstructure with the bandstructures of other components in the device. In general, the band edges alignment and position of the Fermi energy will determine the behavior of the heterojunctions in devices.[80] These energy levels can help predict whether a metal-insulator junction will have ohmic or rectifying behavior and the magnitude of the Schottky barrier at the interface. Similarly, they can also influence the electrical and optical performance of heterojunction diodes. Besides the bandstructure alignment, defects will also influence the electrical and optical performance of GaTe in devices. Defects can increase or compensate the carrier concentration in the material; as well as behave as traps or recombination centers, reducing the carrier lifetime and mobility.[80,95] This chapter will focus on the determination of the band-edges alignment and the energy levels of shallow defects in GaTe. Section 4.1 explains our approach to determine the band-edges alignment–based on ion irradiation and the amphoteric native defect model–and presents our experimental results. Meanwhile, Section 4.2 centers on the determination of shallow-defect levels by low-temperature photoluminescence spectroscopy.

4.1 Band-edges alignment

The band-edges alignment of GaTe has been previously reported by two different groups.[73,126,127] In both cases, the reported values were calculated from the relative barrier height at the interface of a p-n heterojunction. Katerinchuk *et al*. reported the values measured from their p-GaTe/n-InSe junctions.[126] They observed a 0.59 eV difference between the conduction band minimum (CBM) of InSe and the valence band maximum (VBM) of GaTe. Using the previously reported value of the CBM–also referred to as electron affinity–of InSe (χ = 4.55 eV),[128] the VBM of GaTe was calculated to be at 5.14 eV below the vacuum level. Assuming a 1.67 eV bandgap of GaTe at room temperature, the CBM was determined at 3.47 eV below vacuum. Similarly, Wang *et al*. reported the GaTe band-edges to be around 3.2 and 4.9 eV for the CBM and VBM, respectively, using a p-GaTe/n-Si junctions.[73] It is clear that the reported values differ by about 0.2 eV. In addition, it is well known that GaTe generally shows strong Fermi level pinning at the surface,[129] which can result in inaccurate calculations based on the barrier height of heterojunctions. Here, we will determine the band-edges alignment based on the amphoteric native defect model.

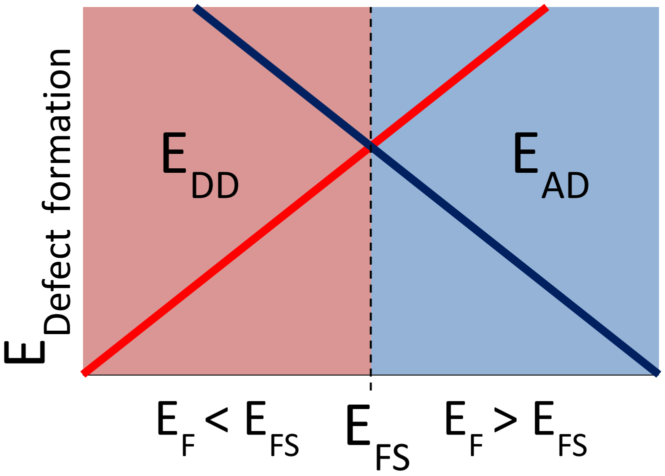

Figure 4.1. Schematic representation of the amphoteric native defect model. Dependence of native defects formation energy on the energy difference between the Fermi energy (E_F) and the Fermi stabilization energy (E_{FS}).

4.1.1 Amphoteric native defect model

The amphoteric native defect model (ANDM), developed by Walukiewicz, relates the electronic behavior of native point defects with the bandstructure of the host semiconductor.[130,131] Specifically, it states that the formation energy of charged point defects will depend on the position of the Fermi energy (E_F) relative to the Fermi stabilization energy (E_{FS}). E_{FS} is a universal energy level for all semiconductors, regardless of bandstructure, localized around 4.9 eV below the vacuum level and marks the Fermi energy position in which the formation energy of both donor-like and acceptor-like defects is the same.[127]

The formation energy of charged point defects will vary linearly with E_F, with the slope proportional to their charge state.[131] When E_F is below E_{FS}, the donor-like defect formation energy (E_{DD}) is lower than the acceptor-like defect formation energy (E_{AD}), preferentially driving the formation of donor-like defects. Analogous, when $E_F > E_{FS}$, the formation of acceptor-like defects is preferred, these behaviors are shown in Figure 4.1. The ANDM helps explain why many semiconductors preferentially exhibit either n-type or p-type transport properties when unintentionally doped. For example, MoS_2 and InSe typically show n-type behavior due to their CBMs being 4.3 and 4.55 eV below the vacuum level, while their bandgaps are 1.8 and 1.25 eV, respectively.[128,132,133] As it can be seen, E_{FS} (4.9 eV) is much closer to the CBM than the VBM in both semiconductors, resulting in the preferred formation of donor-like defects during crystal growth and the n-type behavior. In contrast, unintentionally-doped p-type WSe_2 and GaSe have VBMs around 5.2 and 5.8 eV below the vacuum level and respective bandgaps around 1.65 and 2.0 eV, corresponding to E_{FS} being closer to the VBM.[133,134] Given that GaTe typically shows good p-type behavior, we expect E_{FS} to be closer to the VBM while remaining within the bandgap. If E_{FS} were to be right at the VBM–like reported by Wang *et al.*[73]–or within the valence band, we would expect to see higher hole concentrations, resembling a degenerately doped semiconductor.[93]

The ANDM can also explain the effect of intentionally-generated native point defects on

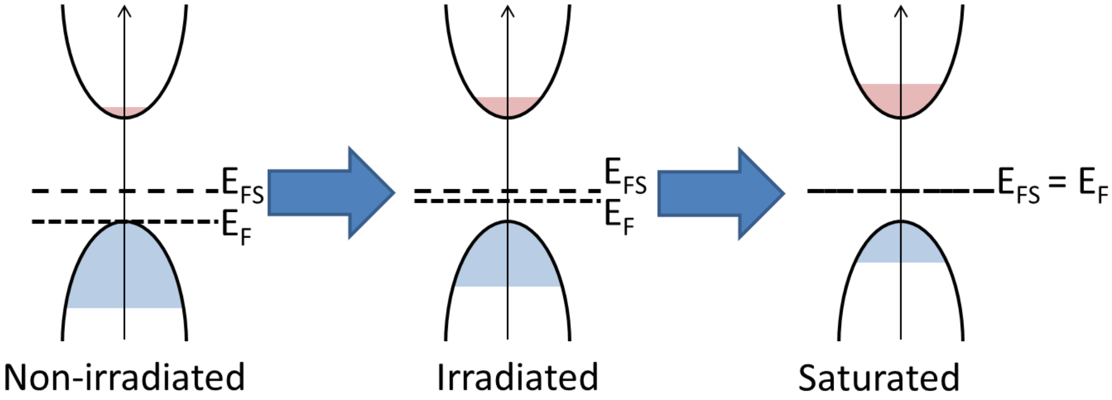

Figure 4.2. Effect of ion irradiation on a p-type semiconductor with $E_F < E_{FS}$, based on the amphoteric native defect model. The formation of donor vacancies is energetically favorable, compensating the initial hole concentration and driving E_F closer to E_{FS}, until saturated.

the carrier concentration of a semiconductor. Native point defects can be generated by irradiating a material with charged particles or γ-rays.[135] If $E_F < E_{FS}$, as shown in Figure 4.2, irradiating the material will cause the preferred formation of donor-like defects, increasing the electron concentration or compensating the hole concentration.[131] This change in carrier concentration will move E_F higher in energy and closer to E_{FS}. As irradiation continues, E_F will reach E_{FS} and the carrier concentration will saturate as donor-like and acceptor-like defects generate at the same rate.[130] The saturated carrier concentration relates E_{FS} with either the CBM or VBM, depending on the carrier concentration identity. For a semiconductor that shows nondegenerate p-type properties at saturation, the saturated hole concentration (p_{sat}), the VBM (E_V) and E_{FS} are related by the following Boltzmann distribution

$$p_{sat} = N_V exp\left(-\frac{E_{FS}-E_V}{k_B T}\right), \tag{4.1}$$

where k_B is the Boltzmann constant, T is the temperature and N_V is the effective density of state in the valence band.[80] N_V is given by

$$N_V = 2\left(\frac{2\pi m_h^* k_B T}{h^2}\right)^{3/2}, \tag{4.2}$$

where m_h^* is the density-of-state effective mass of the valence band and h is the Plank constant. Thus, by knowing the density of states and measuring the saturated carrier concentration, the band-edges alignment can be calculated.

4.1.2 Ion irradiation and band-edges calculation

GaTe flakes, in the order of 4 – 5 μm thick, were obtained by mechanically exfoliation from a bulk ingot grown by the Bridgman method. Evaporated Cr/Au contacts were deposited in the van der Pauw geometry for the Hall effect measurements.[105] The samples were irradiated with helium ions (He^+) at accelerating energy of 4 MeV. Vacancy formation rate and end-of-

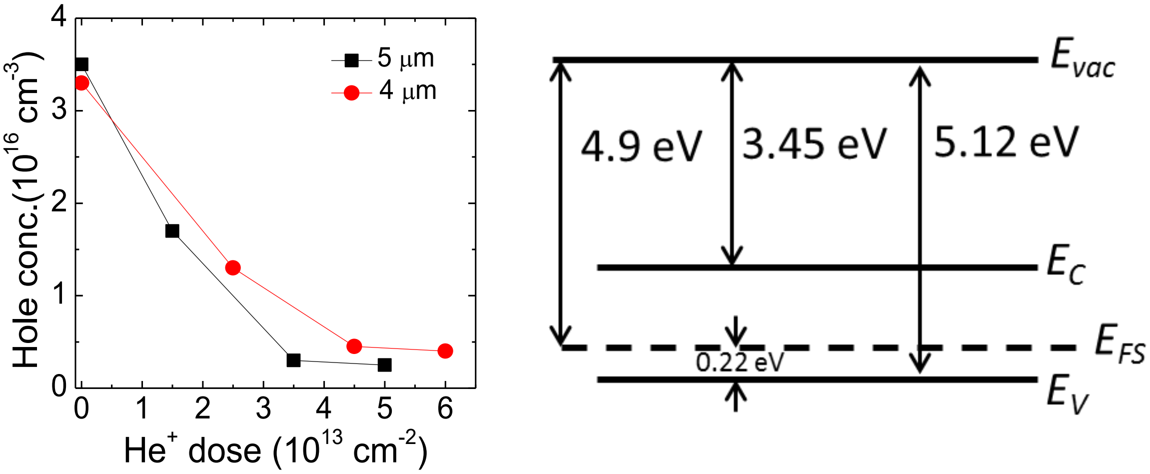

Figure 4.3. **(a)** Hole concentration as a function of 4 MeV He$^+$ irradiation dose, for samples 4 and 5 μm thick. **(b)** Illustration of GaTe's band edges alignment relative to vacuum in real space.

damage depth simulations can be seen in Appendix A.4. The samples were irradiated with multiple 1.5 x10^{13} – 2.5x10^{13} He$^+$ cm^{-2} doses, until the charge carrier concentration saturated, as shown in Figure 4.3.a. It was found that the hole concentration in GaTe dropped from about 3.4x10^{16} cm^{-3} (before irradiation) to about 3.3x10^{15} cm^{-3} at saturation, a decrease of over one order of magnitude. Work performed in collaboration with group member Alex Tseng and LBNL staff scientist Jeffery Beeman.

For the calculations, we will assume the hole effective mass $m_h^* = 0.6m_e$ reported by Gouskov *et al.*, where m_e is the electron mass.[134] The effective density of states was calculated to be N_V = 1.15x10^{19} cm^{-3}, using Equation 4.2. With Equation 4.1, it was calculated that the VBM was just 0.22 eV below E_{FS}, meaning that the VBM of GaTe is about 5.12 eV below the vacuum level. Subtracting the 1.67 eV bandgap from the VBM position gives a CBM around 3.45 eV below vacuum. Figure 4.3.b, shows an illustration of the alignment of GaTe's band edges. We note that our experimental values strongly agree with those reported by Katerinchuk *et al.*, with only a small difference of 0.02 eV.[126]

4.2 Shallow-defect spectroscopy

The shallow defect energy levels and radiative recombination mechanisms of GaTe were studied by low-temperature photoluminescence. GaTe flakes were obtained in a similar fashion as described in the previous section. Low-temperature photoluminescence was obtained at 12 K, by putting the GaTe samples in a recirculating liquid-He chamber. Samples were excited with a 488 nm argon-ion laser with excitation intensities ranging from 1.6 – 600 mW. This work was performed in collaboration with group member Dr. Alex Luce. Figure 4.4, shows the measured PL spectra for excitation intensities up to 50 mW. The spectra can be divided into three main regions: a sharp single peak at 1.778 eV, an asymmetric peak around 1.65 – 1.76 eV and a couple of weak peaks below 1.6 eV. The single peak at 1.778 eV corresponds to the free exciton (*FX*) recombination.[63] The energy of the free exciton peak is given by

$$FX = E_g - E_X, \tag{4.3}$$

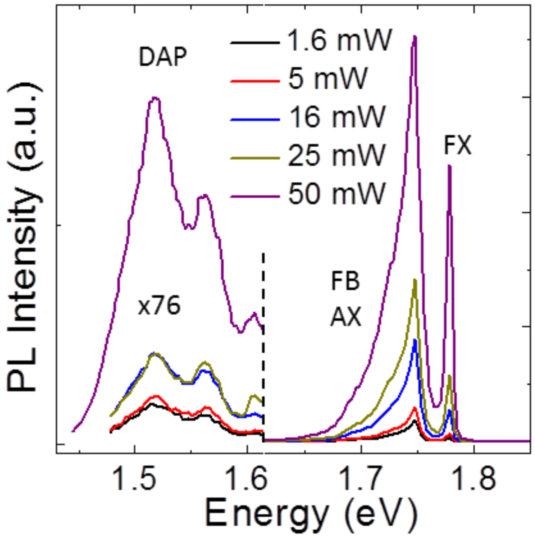

Figure 4.4. Low-temperature photoluminescence spectra of GaTe with different excitation intensities, at 12 K. The relative PL intensities for energies below 1.62 eV are increased 76 times for easier observation.

where E_g is the bandgap and E_X is the exciton binding energy.[135] As mentioned in previous chapters, the exciton binding energy in GaTe is E_X = 18 meV, meaning that the bandgap of GaTe at 8 K is around 1.796 eV, agreeing with values published.[63]

In the second region, between 1.65 – 1.76 eV, the asymmetric peak is actually composed by at least three different peaks around 1.694, 1.735 and 1.748 eV. These peaks correspond to the ones previously reported by Zubiaga *et al*. at 1.70, 1.72 and 1.73 eV.[63,135] Based on their temperature and excitation intensity dependence, the peaks at 1.72 and 1.73 eV were assigned to be acceptor-bound exciton recombination (*AX*), corresponding to shallow acceptor levels of 150 and 110 meV, respectively. Meanwhile, the peak at 1.70 eV was assigned to be free-to-acceptor-bound (FB_A) recombination, into the acceptor level at 110 meV. However, the FB_A energy is given by

$$FB_A = E_g - E_A, \tag{4.4}$$

where E_A is the activation energy of the acceptor. This would result in bandgap energy of 1.81 eV, higher than their measured 1.795 eV bandgap.[63] Now, if we assign the 1.694 eV peak as FB_{A1} recombination, we can use Equation 4.4 to solve for E_A. From this, the first shallow acceptor level is E_{A1} = 102 meV, similar to reported values.[63] The *AX* energy is given by

$$AX = E_g - E_X - E_{BA}, \tag{4.5}$$

where E_{BA} is the binding energy of the exciton to the acceptor and is given by Hayne's rule

$$E_{BA} = b \times E_A, \tag{4.6}$$

where b is the Hayne's constant.[136] The Hayne's constant for GaTe has been previously determined to be b = 0.3.[135] Therefore for E_{A1} = 102 meV, we obtained the values of E_{BA1} = 0.031 eV and A_1X = 1.747 eV, agreeing with our measured peak at 1.748 eV. Finally, if the 1.735

Table 4.1. Calculated energies for recombination processes with acceptor levels at 102 and 146 meV, donor level at 131 meV was assumed for the DAP transitions. Experimental transitions observed are indicated in parenthesis.

E_A (meV)	**FB_A (meV)**	**E_{BA} (meV)**	**AX (meV)**	**DAP**
102	1.694	0.031	1.747	1.563
	(1.694)		(1.748)	(1.563)
146	1.650	0.044	1.734	1.519
	(1.653)		(1.735)	(1.518)

eV peak is assigned as the second acceptor-bound exciton recombination (A_2X), then E_{BA2} = 0.043 eV, E_{A2} = 143 meV and FB_{A2} = 1.653 eV.

In the third region, the peaks below 1.6 eV correspond to the donor-acceptor pair (DAP) recombination. In previous reports, only one peak was observed with the peak energy ranging from 1.57 – 1.60 eV.[62,63,135,137] This peak has been attributed for the recombination from donor levels between 30 – 170 meV below CBM to acceptor levels between 56 – 150 meV above VBM. In our experimental results, we observed two distinct peaks at 1.518 and 1.563 eV, and a possible third peak around 1.61 eV. The 1.563 eV peak was assigned to be the DAP recombination associated with the lowest acceptor level (DA_1P), E_{A1} = 102 meV. The DAP peak energy is given by

$$DAP = E_g - E_D - E_A, \tag{4.7}$$

where E_D is the activation energy of the donor. Solving Equation 4.7 for E_D, using DA_1P and E_{A1}, results in a donor activation energy of E_D = 131 meV. This value is higher than most of the reported donor levels, but it maintains consistency with the other calculated values.[62,63] Lastly, the 1.518 eV peak is assigned to an additional DAP recombination process. Solving Equation 4.7 for E_A, with the calculated E_D value, gives an acceptor activation energy of E_A = 148 meV. This activation energy corresponds to the E_{A2} value of 143 meV and the reported 150 meV acceptor level.[52,62,63,135,138] Averaging the calculated 143 and 148 meV values, results in E_{A2} = 146 meV. Table 4.1, summarizes the relation between the acceptor levels at 102 and 146 meV and the observed PL transitions. Figure 4.5, in turn, shows the shallow-defects energy levels reported here, and their relative arrangement within the GaTe bandgap. The acceptor levels are commonly attributed to Ga vacancies, while the donor level has been previously attributed to either Te vacancies, Te anti-sites or other donor impurities. Additional data and analysis is available in Appendix A.5, including the low-temperature PL of the ion-irradiated samples.

In summary, the ion irradiation of GaTe resulted in the generation of donor-like native defects that partially compensated the as-grown hole concentration. With the saturated hole concentration, the conduction and valence band edges alignment were calculated to be 3.45 and 5.12 eV below vacuum, respectively. Two acceptor levels around 102 and 146 meV–commonly attributed to Ga vacancies–were found responsible for the as-grown p-type behavior. These energy levels were identified through the FB_A, AX and DAP recombination process. Consequently, the DAP transitions also involved a donor level around 131 meV.

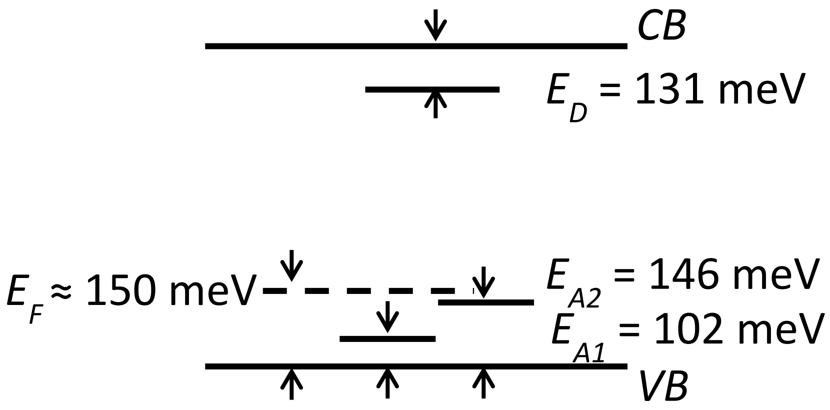

Figure 4.5. Illustration of GaTe's shallow-defects alignment relative to band edges in real space. Two acceptor levels at 102 meV and 146 meV, and one donor level at 131 meV were found.

Chapter 5

Growth and characterization of $GaSe_xTe_{1-x}$ alloys

The alloying of semiconductors is a common and powerful method capable of precise tuning of the bandgap. Semiconductor alloys are of great interest as they can merge the desirable properties of the individual components into a new material.[6,84,87,139,140] As mentioned in Section 1.4.1, alloys of layered semiconductors have been demonstrated with the capability of finely tuning the bandgap, adjusting carrier concentration, passivating surface defects and controlling the semimetallic-to-semiconductor transition.[6,78,85,141] While most of the research on layered semiconductor alloys has focused on TMDs, some efforts have been done in the III-VI monochalcogenide family. These efforts have focused mainly in the alloying of GaSe with other III-VI layered semiconductors, as GaSe possesses the closest structural and chemical properties to every other member in the family (GaS, InSe and GaTe).[30,36,88,142,143]

GaSe-GaTe alloys ($GaSe_xTe_{1-x}$) have been grown and characterized in multiple occasions. Traditionally, the alloys were grown in bulk ingots through the Bridgman method, followed by a series of characterization techniques like XRD, optical absorption, photoluminescence, Raman spectroscopy, resistivity and Hall effect measurements.[30,92,142,144] However, it was found that single-phase alloy crystals weren't able to grow along the complete composition range. Alloy compositions with $x \leq 0.35$ would typically grow as single-phase monoclinic (GaTe-like) crystals, while compositions with $x \geq 0.70$ would typically crystallize in single-phase hexagonal (GaSe-like) ingots. For $0.35 < x < 0.70$, the crystals would phase separate into both monoclinic and hexagonal structures with $x \approx 0.35$ and $x \approx 0.70$, respectively.

Optical absorption and photoluminescence spectroscopy of the single-phase compositions revealed the bandgap dependency on composition.[30,92,142,145] It was demonstrated that the monoclinic phase exhibits a linear increase in bandgap with increasing Se content, from 1.67 eV (pure GaTe) to 1.80 eV for $x = 0.35$. Similarly, it was reported that the hexagonal phase exhibited a linear decrease in bandgap with Te content from 2.01 eV (pure GaSe) to 1.79 eV for $x = 0.70$. Assumption of virtual crystal approximations for both phases, would allow for bandgap extrapolations of 2.07 eV for monoclinic GaSe and 1.14 eV for hexagonal GaTe. From the PL spectra, it was also confirmed that the exciton binding energy remained within 20 meV–similar to pure GaTe and GaSe–making the PL peak energy a good approximation for the alloy bandgap.[142] Resistivity and Hall-effect measurements showed that both hole concentration and mobility dropped as selenium was added to the monoclinic structure, while only the mobility dropped as tellurium was added to the hexagonal structure.[30,144] Instead, the carrier concentration increased by over an order of magnitude for $x = 0.70$, compared to pure GaSe.

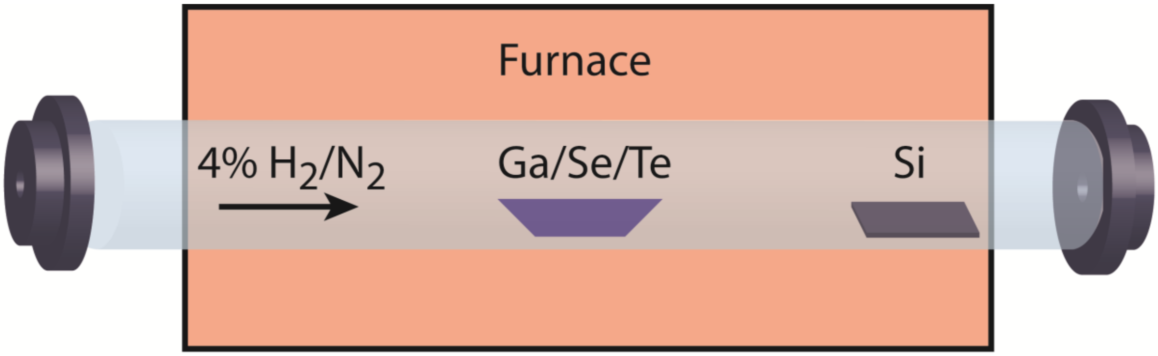

Figure 5.1. Schematic of the vapor growth process arrangement inside the tube furnace.

In this chapter I demonstrate the growth and characterization of the $GaSe_xTe_{1-x}$ alloy by vapor deposition. Section 5.1 discusses the general growth parameter utilized and comments on the shape and sizes of the grown crystals. Sections 5.2 and 5.3 focus on the chemical and structural characterization of the alloy crystals. Meanwhile, Section 5.4 centers on determining the bandgap dependency on composition along the whole compositional range. Finally, Section 5.5 presents density functional theory calculations that give an explanation to the observed behavior.

5.1 Vapor deposition growth

The $GaSe_xTe_{1-x}$ alloys were grown inside a one-zone quartz tube reactor. Selenium and tellurium powders were placed together with molten gallium droplets (≈ 80 °C) in an alumina crucible at the center of the tube furnace, similar to Figure 5.1. The composition was controlled by changing the selenium-to-tellurium ratio, while maintaining the gallium amount in excess (about 3:1 gallium/chalcogenide mole ratio). Nominal concentrations of $x = 0$, 0.03, 0.10, 0.25, 0.50. 0.65, 0.75 and 1 were grown. Silicon substrates decorated with 20 nm gold nanoparticles were placed 16 – 18 cm downstream from the powder crucible. The procedure used to deposit the gold nanoparticles on the silicon substrate is available in Appendix B.3. Forming gas (4% H_2 in N_2) was flown at a rate of 300 sccm to minimize possible oxidation reactions. The powder crucible temperature was increased to 1030 °C at a ramping rate of 20 °C/min.[71] The substrates temperature varied from about 600 °C to 800 °C, with most of the growth occurring near the hotter end. The furnace temperature profile is shown in Appendix A.6. After growth, crystals were transferred, by physical contact, to clean substrates for characterization.

5.1.1 Grown crystals

Figure 5.2 shows some examples of the general shapes of the crystals grown. For nominally tellurium-rich compositions ($x \leq 0.10$), the crystals tended to grow in either of three morphologies: triangles, elongated crystals or nanowires where the nanowires generally grew out of the base of the triangles, as seen in Figures 5.2.a,c. We note that triangular-shaped crystals have been previously reported for the vapor growth of monoclinic GaTe, suggesting a similar crystal structure for alloys of such shape.[72] For nominally higher selenium content compositions ($x \geq 0.10$), the crystals grew in zig-zagged or serrated shapes (Figures 5.2.b and 5.1.d). Both of

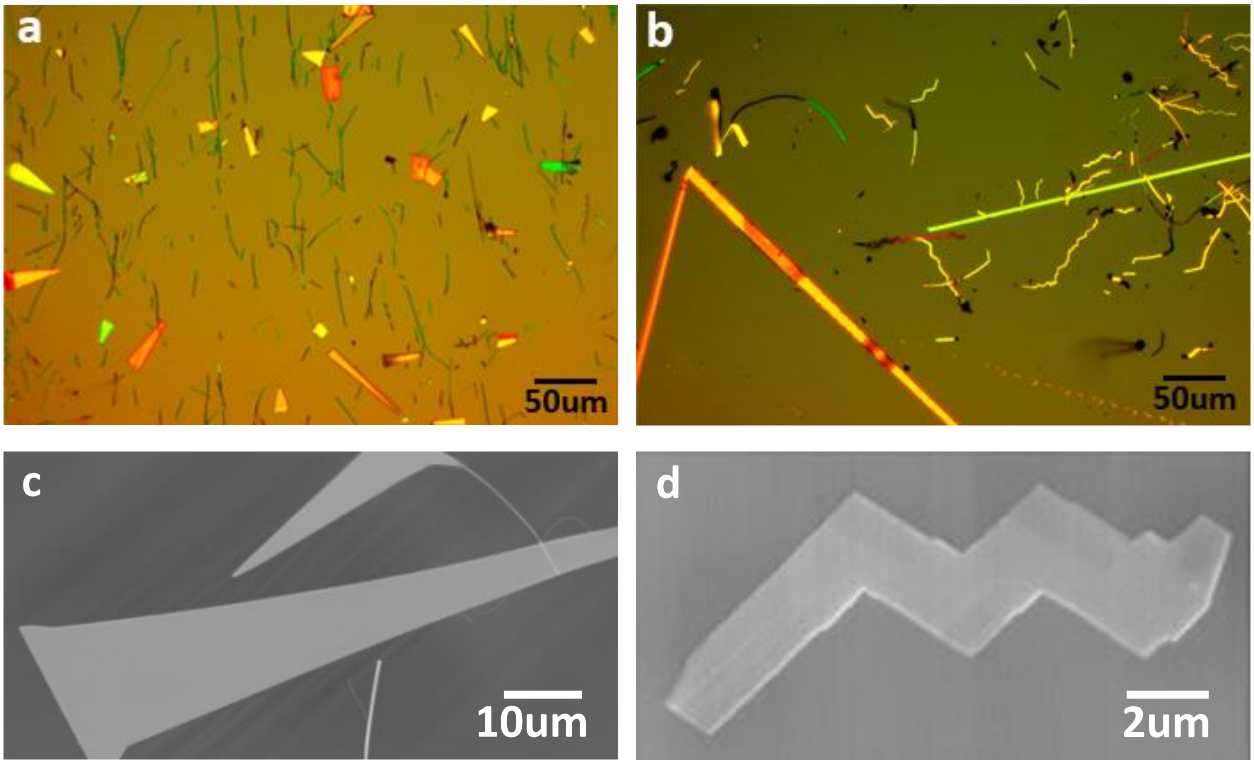

Figure 5.2. Optical micrographs of crystals grown for nominally **(a)** x = 0.10 and **(b)** x = 0.75, after being transferred to a Si substrate. Isosceles triangular crystals and wires were grown in **(a)** while zig-zagged and serrated crystals were grown in **(b)**. Scanning electron micrographs of crystals grown with **(c)** triangular and **(d)** zig-zagged shapes. Nanowires can also be seen in **(c)**.

Table 5.1. Comparison between nominal composition and actual composition range.

Nominal composition (x fraction)	Actual composition (x fraction)
0	0
0.03	0.09 – 0.23
0.10	0.20 – 0.32
0.25	0.37 – 0.49
0.50	0.64 – 0.73
0.65	0.82 – 0.92
0.75	0.92 – 0.96
1	1

these morphologies have been previously reported for the vapor growth of hexagonal GaS and GaSe, with angles around 120° characteristic of the hexagonal structure.[146,147] Interestingly, the growth of nominally x = 0.10 resulted in a mixture of crystal morphologies, with triangular and zig-zagged crystals growing next to each other. With the exception of the nanowires, most of the grown crystal dimensions ranged around the tens to hundreds of micrometers in length, single-digit to tens of micrometers in width and tens to hundreds of nanometers in thickness. The

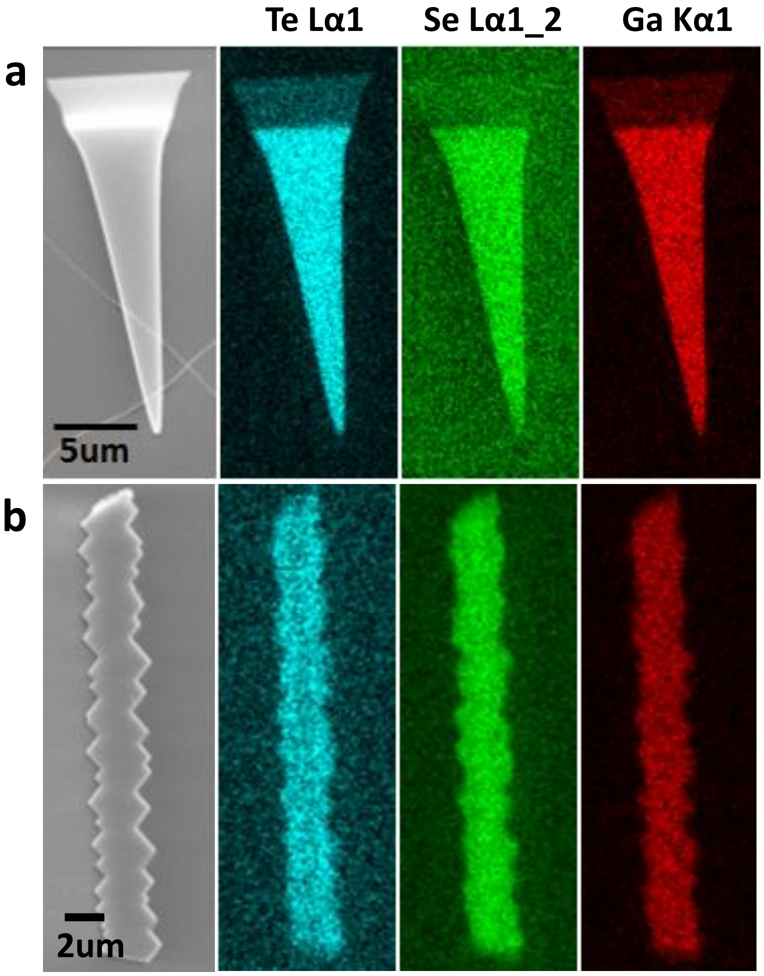

Figure 5.3. Scanning electron micrographs and EDS chemical maps for representative crystals with **(a)** x = 0.32 and **(b)** x = 0.65. Smooth surfaces and chemical uniformity are evident. Thin nanowires can also be seen crossing over the larger crystal in **(a)**.

nanowires dimensions, instead, ranged around tens of micrometers in length, hundreds of nanometers in width and tens of nanometers in thickness. Overall, larger crystals were generally found in nominally Se-rich growths, where nucleation at the quartz-tube's wall was also observed.

5.2 Chemical composition analysis

The actual chemical composition of the grown alloys was determined by x-ray energy dispersive spectroscopy (EDS) inside a scanning electron microscope (SEM). EDS spectra were obtained with an electron accelerating voltage of 20 keV. Results showed that the selenium content in the crystals tended to be higher than the nominal composition, as seen in Table 5.1. This behavior could be due to either the higher vapor pressure of Se compared to Te, the fact that tellurium evaporates as Te_2 making it harder to react with other components or the growth of the

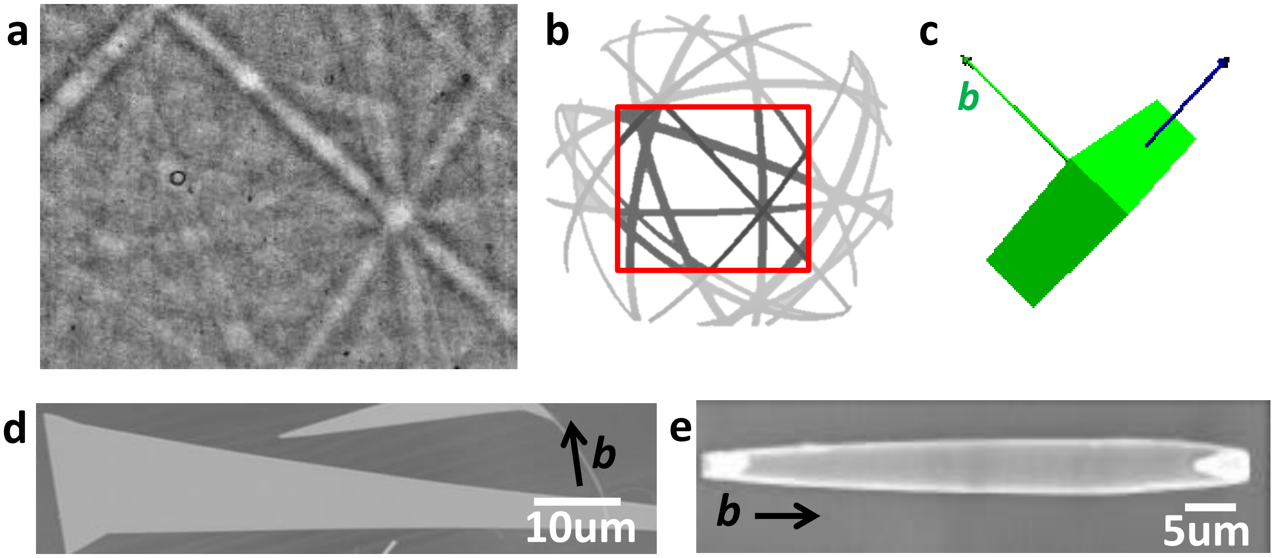

Figure 5.4. (a) Experimental EBSD pattern for triangular crystal with x = 0.30 (crystal shown in Figure 5.2.c and 5.4.d). **(b)** Simulated EBSD pattern for monoclinic GaTe oriented as shown by unit cell in **(c)**. The simulated pattern matches the experimental data. **(d)** Triangular and **(e)** elongated crystals with monoclinic structure. The orientation of the in-plane *b*-axis is indicated with black arrows.

hexagonal phase being preferred over the monoclinic, among others.[148–150] In Figures 5.3.a,b, we observe a triangular crystal (x = 0.32) and a serrated crystal (x = 0.65) with their corresponding chemical composition maps, showing chemical uniformity. We note that the serrated crystal with x = 0.65 grew with a composition that wasn't possible through the bulk methods.

5.3 Crystal structure analysis

The crystal structures of the grown alloy crystals were determined by electron backscattering diffraction (EBSD) inside a SEM. The EBSD patterns were also obtained with an accelerating voltage of 20 keV, similar to EDS. The patterns were compared with crystallographic data of monoclinic GaTe, hexagonal β-GaTe, hexagonal β-GaSe and hexagonal ε-GaSe, obtained from the Inorganic Crystal Structure Database (153456-ICSD, 43328-ICSD, 63122-ICSD and 71082-ICSD, respectively). Additional Raman spectra characterization is shown in Appendix A.7.

5.3.1 Monoclinic phase

The monoclinic-grown crystals were identified by the EBSD pattern until a clear distinction between crystal shape and crystal structure was established. Figure 5.4.a shows the typical EBSD pattern observed for the monoclinic crystals. The monoclinic nature of the experimental pattern can be easily confirmed when comparing it to the simulated pattern of monoclinic GaTe, seen in Figure 5.4.b. The orientation of the monoclinic GaTe unit cell, corresponding to the simulated pattern, can be seen in Figure 5.4.c. As expected, the monoclinic crystals grew preferentially along the layer plane. With the EBSD measurements, it was confirmed that the triangular and elongated crystals had, in fact, the monoclinic structure as

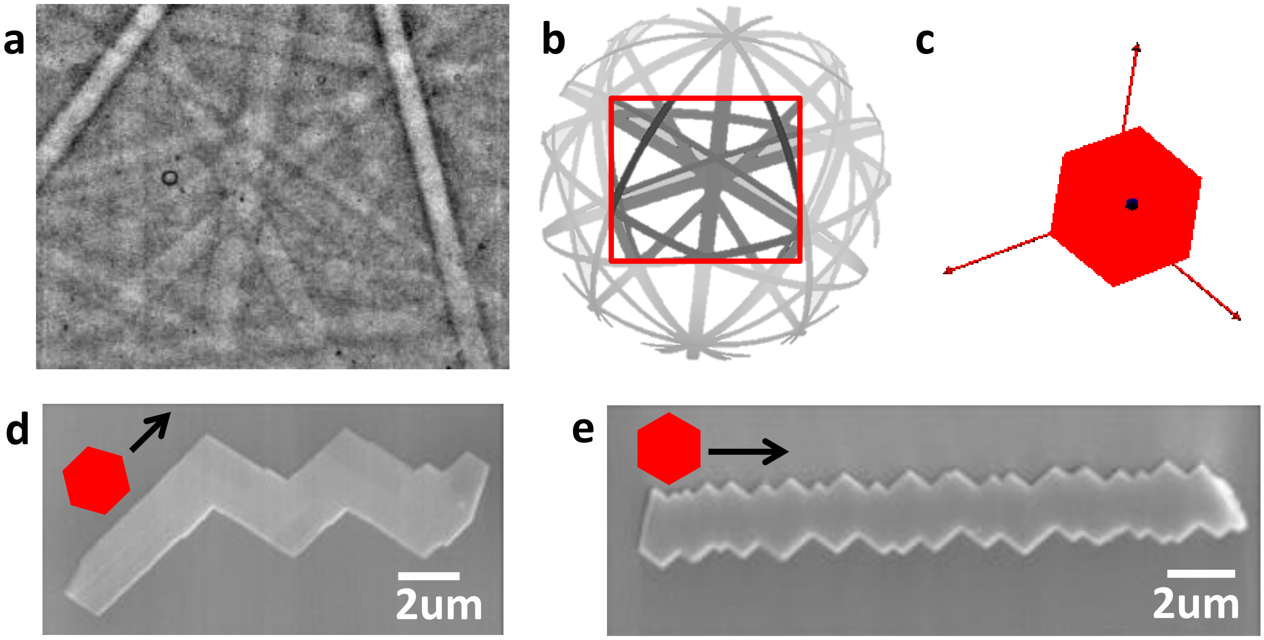

Figure 5.5. (a) Experimental EBSD pattern for serrated crystal with x = 0.49. **(b)** Simulated EBSD pattern for the hexagonal ε-GaSe crystal structure oriented as shown by unit cell in **(c)**. The simulated pattern matches the experimental data. **(d)** Zig-zagged and **(e)** serrated crystals with hexagonal structure. The orientation of the hexagonal lattice is indicated with black arrows.

suspected. Figure 5.4.d shows that the triangular crystals preferentially grew perpendicular to the *b*-axis (along the in-plane Ga-Ga bonds), with the base of the triangle aligned to it. In contrast, the elongated crystals grew exclusively along the *b*-axis. The difference in orientation between these two morphologies could be explained by different growth mechanisms at specific conditions. Overall, it was observed that monoclinic crystals only grew in tellurium-rich conditions with compositions ranging from pure GaTe to x = 0.32, similar to what was previously observed in bulk.[30]

5.3.2 Hexagonal phase

Analogous to the analysis for the monoclinic phase, EBSD was used to identify the alloy crystals with the hexagonal structure. Figure 5.5.a shows the experimental EBSD pattern of a serrated crystal with x = 0.49. This pattern was confirmed to correspond to the hexagonal structure by the simulated pattern of ε-GaSe at the indicated unit cell orientation (Figures 5.5.b and 5.4.c, respectively). As expected, it was confirmed that the zig-zagged and serrated crystals had the hexagonal structure and grew along the hexagonal layer plane, as seen in Figures 5.5.d,e. It can also be seen that zig-zagged crystals grew preferentially along the armchair direction, while the serrated crystals grew along the zig-zag direction. Similarly, the difference in growth orientation might have been caused by slight differences in localized growth conditions. Remarkably, we observed the growth of hexagonal alloy crystals within the range of x = 0.28 to pure GaSe in clear contrast to the results observed for the bulk growth.[30] Growing thin crystals with high surface-to-volume ratios allows for the relaxation of some of the stress generated by the incorporation of tellurium into the hexagonal lattice.[22,104,151] Note that the average size of

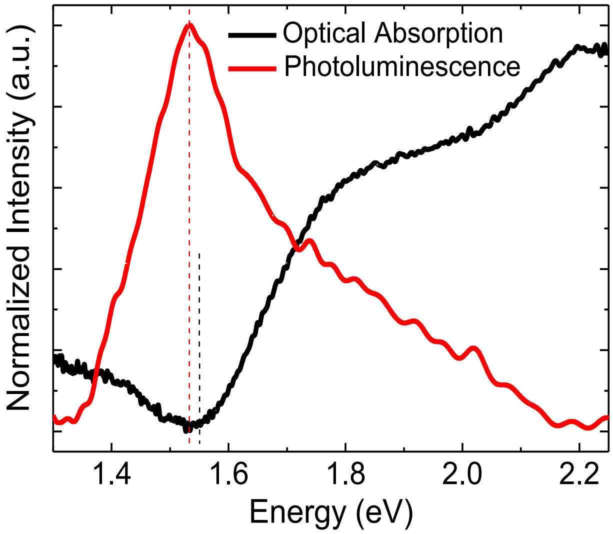

Figure 5.6. Micro-optical absorption and photoluminescence spectroscopy of a hexagonal crystal with x = 0.48. The exciton binding energy remains around 20 meV.

the hexagonal crystals decrease with tellurium content, agreeing with the previous analysis. Interestingly, while there was a phase-separation gap around $0.35 < x < 0.70$ for the bulk growth,[30] we observe an overlap region around $0.27 < x < 0.35$ for the vapor growth. Within the overlap region, both single-phase monoclinic and hexagonal alloy crystals are able to grow simultaneously. Mixed-phase crystals have also been observed and will be discussed in Appendix A.8.

5.4 Bandgap determination

The bandgaps of Bridgman-grown $GaSe_xTe_{1-x}$ alloys had been previously determined by optical absorption and photoluminescence spectroscopy.[92,142] It was also demonstrated that the binding energy of the exciton remained around 18 – 20 meV, similar to GaTe and GaSe.[39,137,142,145] This would allow for the simple approximation of the bandgap with the PL peak energy.

5.4.1 Micro-optical absorption spectroscopy

Micro-optical absorption was carried out on selected crystals to confirm that the approximation of the bandgap with the PL peak energy holds for the middle compositions–compositions not grown through the Bridgman method. These measurements were performed in collaboration with Prof. Jie Yao and his student Kyle Tom. Details on the experimental setup for the micro-optical absorption can be found on Appendix B.4. Figure 5.6 shows the absorption spectrum (black) of a hexagonal crystal with x = 0.48. The absorption edge of the crystal was determined to be around 1.55 eV. The corresponding PL spectrum for the same crystal is also shown (red). The peak energy of the PL spectrum is observed at 1.53 eV. The energy difference between the absorption edge and the PL peak, 20 meV, is the exciton binding energy.[137] Thus, the approximation holds for the middle compositions.

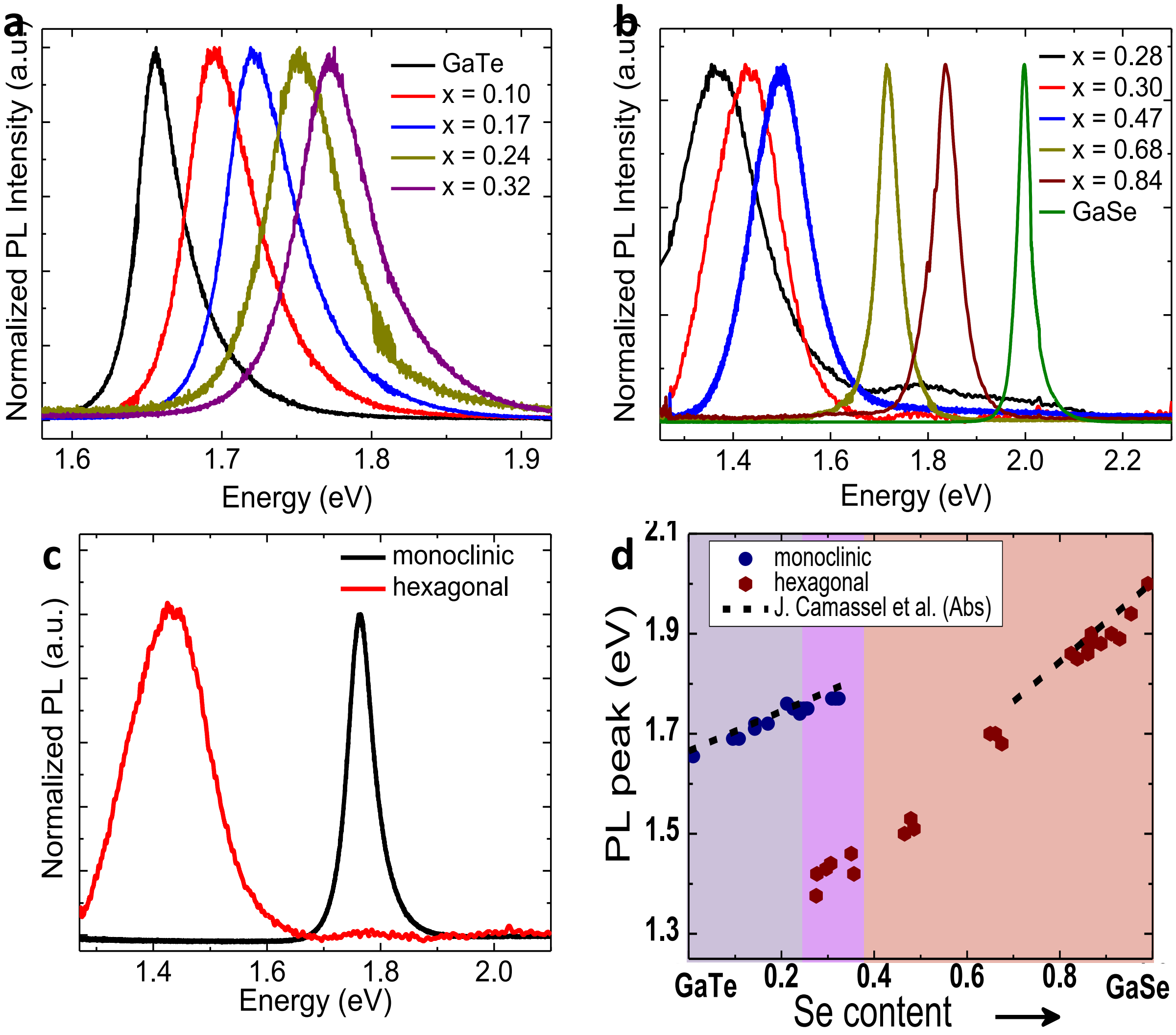

Figure 5.7. Selected photoluminescence peaks for **(a)** monoclinic and **(b)** hexagonal crystals, the PL energy increases with selenium content in both structures. **(c)** Normalized PL spectra for monoclinic (x = 0.32) and hexagonal (x = 0.30) crystals within the overlap range. The PL emission of the monoclinic crystal is about 17 times stronger. **(d)** PL peak dependence on the selenium content and crystal structure. Dotted lines represent the linear trends observed for the bulk crystals.

5.4.2 Photoluminescence spectroscopy

The evolution of the PL spectra with increased selenium content for the monoclinic and hexagonal phases are shown in Figures 5.7.a and 5.7.b, respectively. For the monoclinic phase, the room temperature PL peak of GaTe is at 1.65 eV. As selenium is incorporated, the bandgap increases up to 1.77 eV for x = 0.32. Broadening and intensity loss of the PL peak is also observed with the addition of selenium to the monoclinic phase. On the other hand, the hexagonal phase exhibits a decrease in PL peak energy from 2.00 eV for GaSe to 1.38 eV for x = 0.28 with tellurium incorporation. Similarly, the addition of tellurium to the hexagonal phase also results in the broadening and intensity loss of the PL peak. Note that the 1.38 eV PL peak corresponds to a bandgap that is about 0.27 eV smaller than that of GaTe and about 0.63 eV smaller than the band gap for GaSe.

Within the overlap region ($0.27 < x < 0.35$), one observes a bandgap difference of about 0.30 – 0.35 eV for crystals with the same composition but different crystal structure. The magnitude of this difference is evident in Figure 5.7.c, where the PL peak energy of a monoclinic crystal with $x = 0.32$ is about 0.35 eV greater than the PL peak energy for a hexagonal crystal with $x = 0.30$. It is also evident that the PL peak of the hexagonal crystal is broader. The hexagonal PL peak intensity was about 17 times weaker than the PL of the monoclinic crystal. In the overlap region, based on the crystal sizes (i.e. monoclinic crystals are considerably larger than the hexagonal ones) and PL intensities, the monoclinic crystals appear to be more energetically favorable with the higher-energy hexagonal structure stabilized only by the high surface-to-volume ratio morphologies.

The dependence of the PL peak–and the bandgap–on the alloy composition and crystal structure is plotted in Figure 5.7.d. Three main regions, separated by the background color, are observed. The blue background ($0 \leq x \leq 0.27$) indicates the compositions where only monoclinic crystals were grown, the purple background indicates the overlap region and the red background ($x \geq 0.35$) indicates the region where only hexagonal crystals were grown. The dotted lines represent the bandgaps determined by optical absorption of the bulk crystals.[92] As it can be seen, the linear trend of the monoclinic bandgap perfectly agrees with the previously reported behavior and seems to correspond to a virtual crystal approximation. For the hexagonal phase, the selenium-rich crystals agree with the reported linear trend, but the values start to deviate toward the middle compositions. To explain the observed trends and the possible bandgap bowing in the hexagonal phase, theoretical calculations will be discussed in the next section.

5.5 Density functional theory calculations

Density functional theory (DFT) calculations were performed to explain the observed bandgap dependence on crystal structure and alloy composition. The results presented here were obtained mainly by our collaborator Dr. Matthew K. Horton at Lawrence Berkeley National Lab. Details on the theoretical calculations can be found in the Appendix B.5. Figure 5.8.a shows calculations done using the Perdew–Burke–Ernzerhof (PBE) exchange-correlation functional. Noticeably, the bandgap values were significantly underestimated as expected for the PBE functional. They exhibit a linear increase of the bandgaps for the monoclinic phase at the tellurium-rich compositions as experimentally observed. For the hexagonal phase, an apparent linear trend was obtained around the mid- to high-selenium compositions, with the direct gap slightly above the indirect gap, similar to GaSe.[42,88] For the low-selenium hexagonal compositions ($x < 0.30$), the bandgaps start deviating from the apparent linear trend, plateauing around the $0.10 < x < 0.20$ range. For compositions below $x = 0.10$, we observe that the indirect gap continues to decrease while the direct gap increases slightly, resulting in a large energy difference between the gaps.

The Tran-Blaha modified-Becke Johnson (MBJ) potential was used to better approximate the bandgap values of the hexagonal phase. Figure 5.8.b shows the obtained results with the MBJ approximation and the experimental PL peak energy values for comparison. Contrary to the PBE calculations, the bandgaps obtained with the MBJ approximation are overestimated, but considerably closer to the real values. Similar to the experimental data and the PBE calculations, the bandgap values deviate from any potential linear trend towards the middle and low-selenium

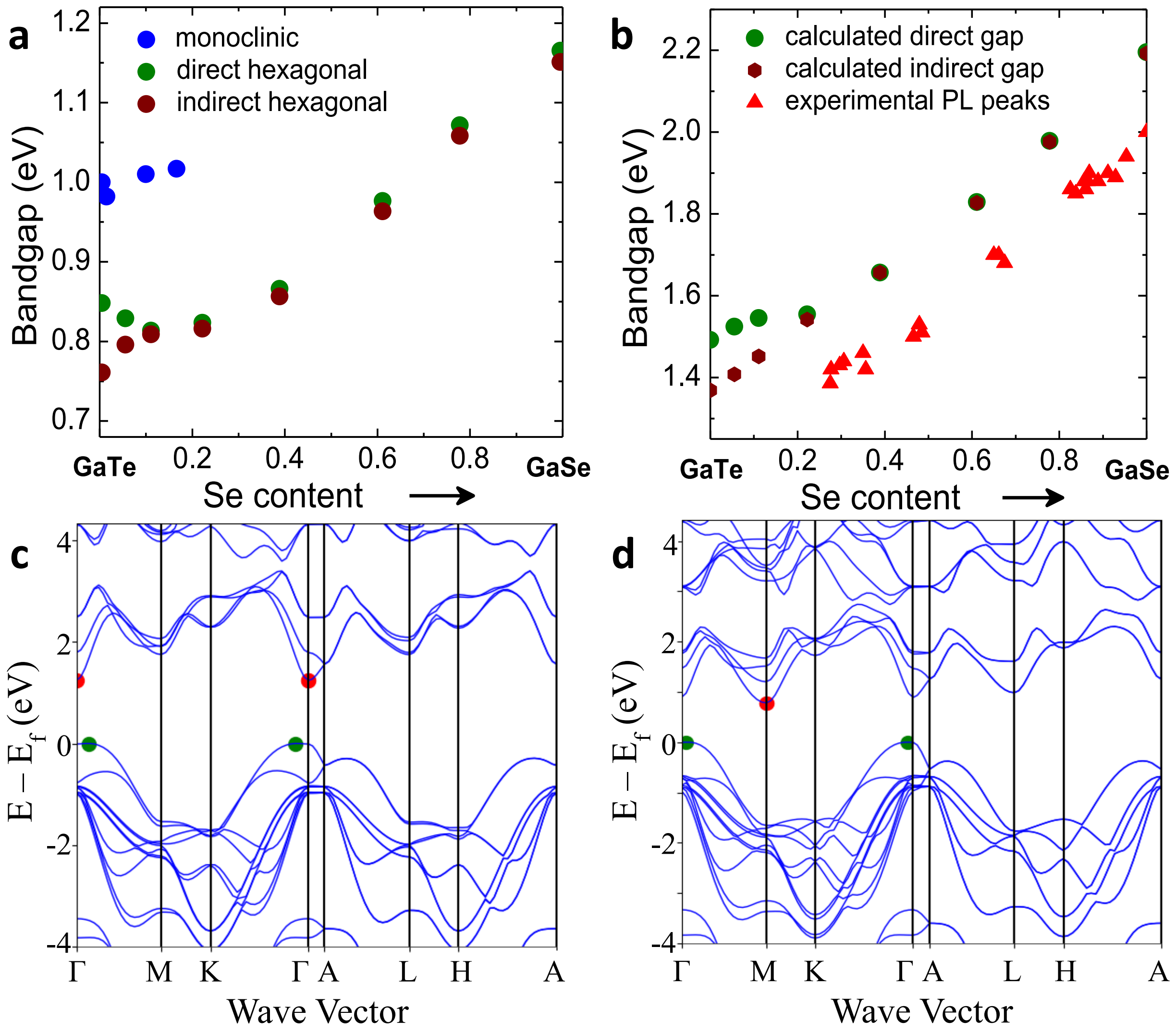

Figure 5.8. **(a)** DFT-calculated bandgaps for the GaSe$_x$Te$_{1-x}$ alloys using the PBE exchange-correlation functional. **(b)** Corrected DFT-calculated bandgaps for the hexagonal phase using the MBJ potential approximation. Experimental PL peak data presented for reference. Calculated bandstructures for the hexagonal phase endpoints **(c)** ε-GaSe and **(d)** β-GaTe, obtained from the Materials Project.[34,51,53,152] The valence band maxima are indicated with green dots and the conduction band minimum is indicated with a red dot.

compositions. For x < 0.30, the energy difference between the indirect and direct gaps also increases. However, the indirect gap continuously decreases, while only the direct gap briefly plateaus before decreasing again. Even though calculations with the MBJ potential are better at approximating the actual bandgap values,[153,154] it is generally accepted that bandgap trends are better represented by calculations with the PBE functional.

The bandstructures of the hexagonal alloys were analyzed to understand the sudden change in bandgap trend for the x < 0.30 compositions. It was found that around x = 0.20 the conduction band minimum changes from the Γ-point (like β- and ε-GaSe, Figure 5.8.c) to the *M*-

point (like β-GaTe, Figure 5.8.d).[34,51,53,152] In contrast, the valence band maximum remains degenerate and located slightly off from the Γ-point, along the $\Gamma \rightarrow M$ and $\Gamma \rightarrow K$ directions. The next chapter will be dedicated to the growth and characterization of hexagonal GaTe to confirm the calculated behavior for the tellurium-rich compositions.

Chapter 6

Growth and characterization of hexagonal GaTe

Layered semiconductors, like TMDs and III-VI monochalcogenides, are commonly associated with the hexagonal structure.[4,5] As discussed in Chapter 1, exceptions to this observation are the 1T-TMD subfamily, like SnS_2, and GaTe.[5,18] GaTe typically crystallizes in the monoclinic structure, but additional cubic and hexagonal phases have also been identified. A metallic high-pressure NaCl-like cubic structure was observed when GaTe was subjected to hydrostatic pressures above 10 GPa.[53,155] The metastable hexagonal structure has been obtained by several growth methods, quickly transforming back to the stable monoclinic structure.[53,54,55] The hexagonal structure has also been claimed to be the stable phase at the few-layer regime and after surface reconstruction in bulk with additional reports claiming otherwise.[104,156-158] Further, the reported experimental values for the hexagonal GaTe (*h*-GaTe) bandgap range from 1.1 – 1.65 eV at room temperature.[54,55,158] To reach consensus among these values, this chapter focuses on the growth and characterization of *h*-GaTe by using GaSe flakes as epitaxial substrates. Section 2.1 is a detailed review of previous works on the growth and characterization of *h*-GaTe. Section 6.2 discusses the proposed growth method and its general results, while Section 6.3 centers on the chemical and optical characterization of the grown crystals.

6.1 Hexagonal GaTe background

Hexagonal GaTe is a metastable polymorph of GaTe, first reported by Semelitov *et al.* in 1964.[53] The layer thickness of *h*-GaTe is about 8.48 Å, with Ga-Te and Ga-Ga bond lengths of 2.61 Å and 2.71 Å, respectively. The hexagonal layers stack in the β polymorph, similar to GaS, resulting in a 2H unit cell with lattice parameters a = 4.06 Å and c = 16.96 Å.[53,34] Theoretical calculations have shown that *h*-GaTe is an indirect gap semiconductor with a smaller bandgap than the monoclinic phase.[152,159] The calculations done using the PBE functional, shown in Figure 5.7.a, indicated an indirect gap of 0.76 eV, with the direct gap about 0.09 eV higher. Meanwhile, the calculations done with the MBJ approximations revealed an indirect gap of 1.37 eV, with the direct gap about 0.12 eV higher. Note that the values obtained with the PBE functional typically underestimate the bandgaps while the values obtained with the MBJ approximation overestimate them.

Given the rapid transformation to the monoclinic structure, there are only a few reports of the experimental bandgap of *h*-GaTe. Gillan *et al.* measured a 1.45 eV bandgap by optical transmission spectroscopy for a *h*-GaTe film grown by chemical vapor deposition.[54] Also by transmission spectroscopy, Kolesnikov *et al.* measured a 1.65 eV bandgap for a *h*-GaTe flake obtained from an ingot grown by high-pressure melting seemingly measuring the bandgap after the flake transformed into the monoclinic phase.[55] Finally, Galiy *et al.* measured a bandgap

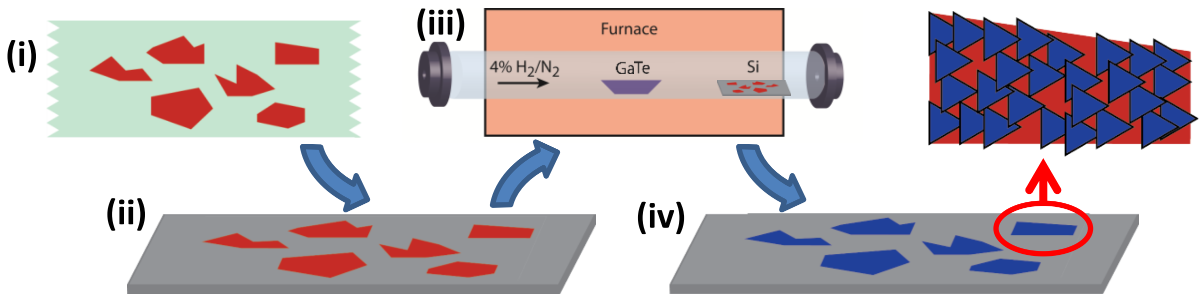

Figure 6.1. Proposed method for the growth of *h*-GaTe on GaSe flakes. **(i)** GaSe (red) flakes mechanically exfoliated with tape were **(ii)** transferred onto a silicon substrate and **(iii)** inserted in a tube furnace for epitaxial GaTe growth on GaSe, by vapor deposition. After growth, **(iv)** the grown GaTe (blue) crystals were inspected and characterized.

around 1.06 eV, by scanning tunneling spectroscopy, for a monoclinic GaTe sample with partial surface reconstruction into the hexagonal phase.[158] Note that in the same study a 1.75 eV gap was reported for monoclinic GaTe.

6.2 Growth of hexagonal GaTe

Thin-films of hexagonal GaTe have been previously grown by some form of vapor deposition.[53,54] Similar to the growth discussed in the previous chapter, the high surface-to-volume ratio of the thin crystals allows for a higher degree of in-plane strain relaxation, slightly stabilizing the hexagonal phase. In fact, it has been calculated that the hexagonal phase becomes more stable than the monoclinic phase at the monolayer regime.[104]

6.2.1 Proposed method

The growth of multilayer *h*-GaTe was induced by using substrates with hexagonal crystal structure to serve as epitaxial surfaces. The growth method consists of the use of GaSe substrates for the vapor deposition of *h*-GaTe. GaSe flakes were mechanically exfoliated with adhesive tape from a bulk ingot grown by the Bridgman method, as illustrated in the first step of Figure 6.1. For the second step, the exfoliated flakes were then transferred onto a cleaned silicon substrate. In the third step, the silicon substrates were placed inside the furnace tube reactor for the GaTe growth process. Finally, the crystals grown at the GaSe surface were inspected and characterized.

The growth was done inside a single-zone quartz tube reactor, similar to the one described in Section 5.1 and illustrated in Figure 5.1. Monoclinic GaTe powder was placed in a quartz boat at the center for the furnace tube. The substrates with the GaSe flakes were placed 13 – 16 cm downstream from the quartz boat. Forming gas was flown at a rate of 75 sccm. The quartz boat temperature was increased to 800° C at a ramping rate of 20 °C/min. The substrates temperature varied from about 500 °C – 650 °C. The furnace temperature profile is shown in Appendix A.6.

6.2.2 Results

Post-grown inspection revealed that numerous thin crystals preferentially grew around

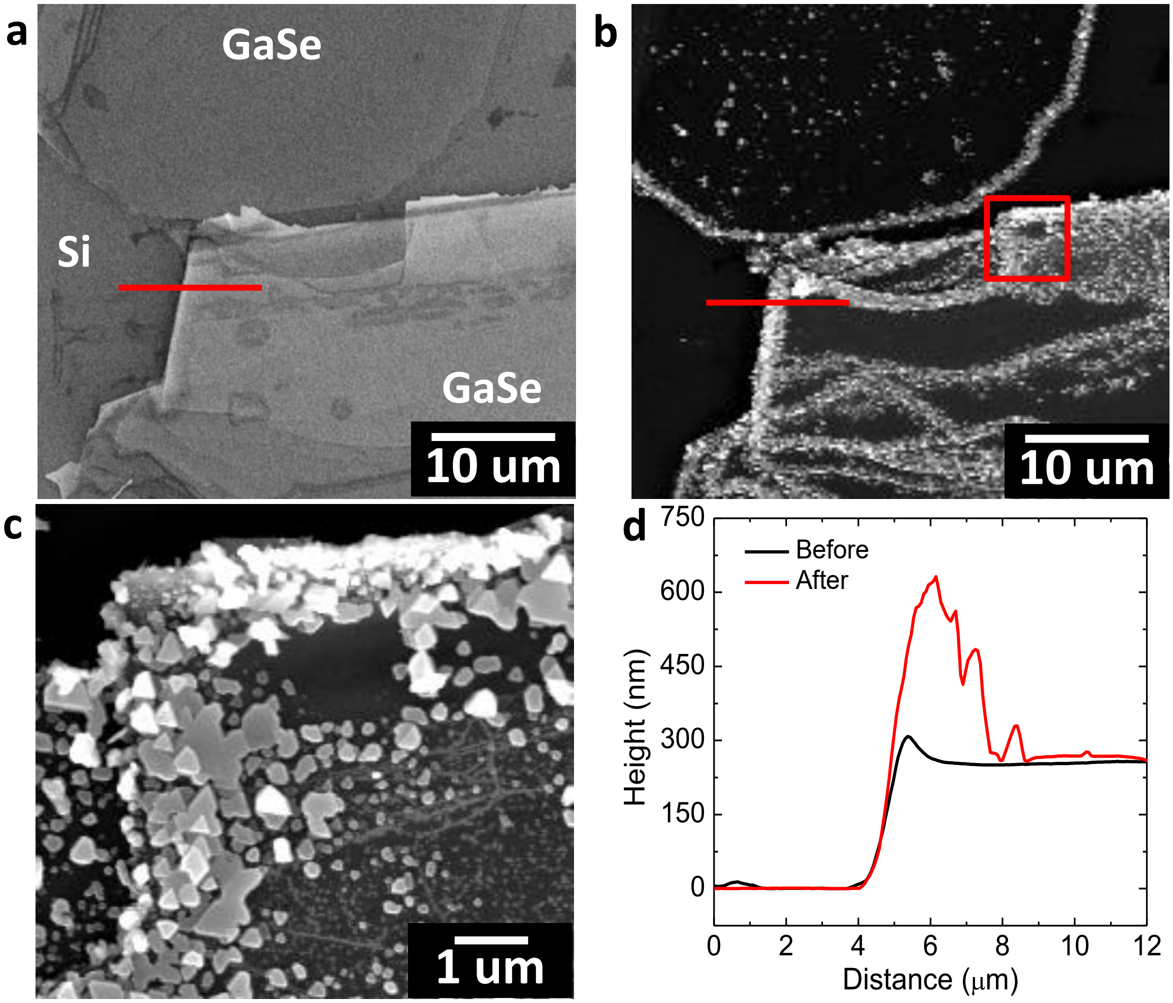

Figure 6.2. Scanning electron micrographs of GaSe flakes on a silicon substrate **(a)** before and **(b)** after GaTe growth. **(c)** Higher magnification micrograph of region marked by red square in **(b)**. Triangular and hexagonal islands grew preferentially around the GaSe edges. **(d)** Height profile of GaSe flake's edge before and after growth, scanned area indicated by red line in **(a)** and **(b)**.

the borders of the GaSe flakes, as shown in Figures 6.2.a,b. Upon further inspection (Figure 6.2.c), it was noted that the grown crystals had triangular and hexagonal shapes, well-known equilibrium morphologies for thin-crystals with hexagonal crystal structure.[6,36,147,160] Atomic-force microscopy (AFM) at the edge of the GaSe flakes (Figure 6.2.d), showed that their thicknesses didn't changed during the growth process. This suggests a low level of GaSe incorporation into the grown crystals. Overall, it was found that the grown crystals' lateral and thickness dimensions were generally around the hundreds of nanometers range.

6.3 Characterization of hexagonal GaTe

The general characterization of the grown crystals consisted in the determination of their chemical composition and bandgap. Figure 6.3.a shows a cross-sectional schematic of the

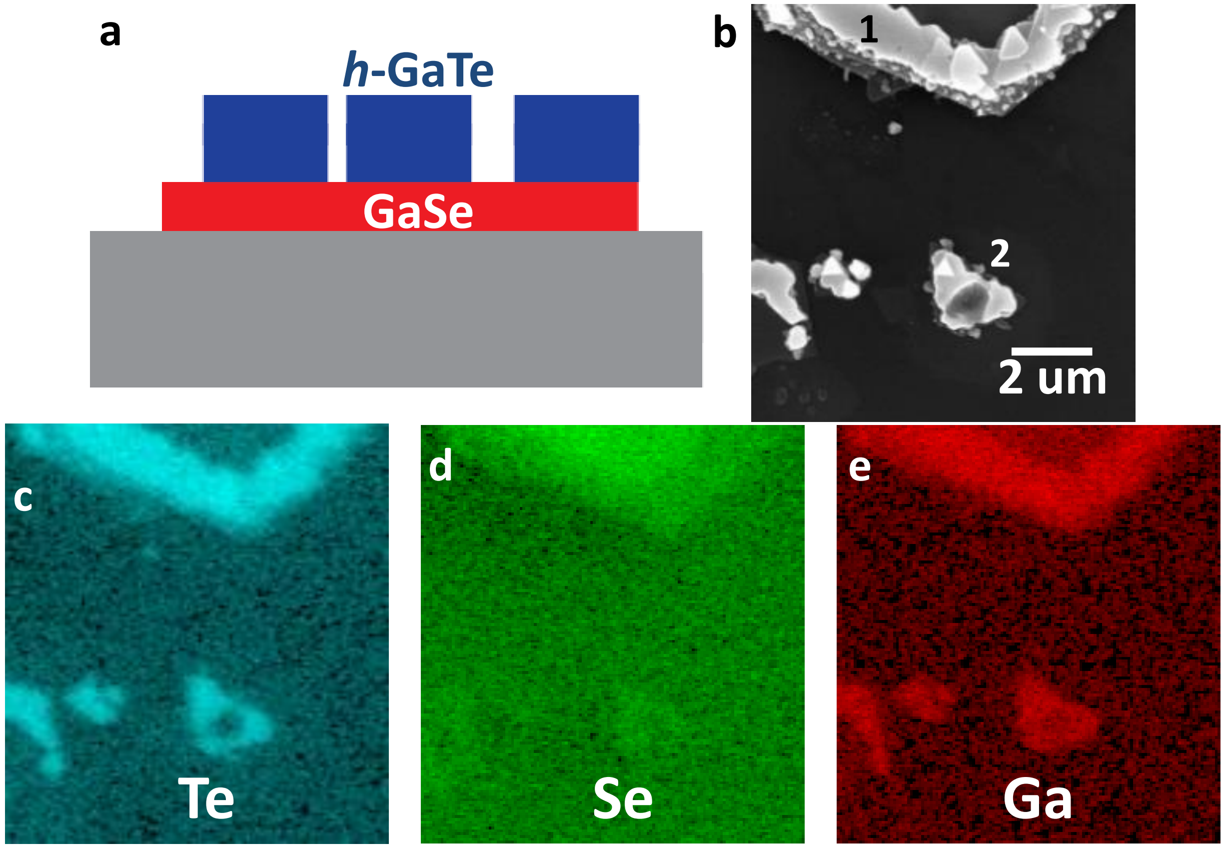

Figure 6.3. (a) Cross-sectional schematic of *h*-GaTe/GaSe/Si assembly probed by EDS. **(b)** Scanning electron micrograph and **(c)-(e)** chemical composition maps of crystals grown on GaSe flakes.

grown-crystals/GaSe/silicon assembly. Note that any characterization technique capable of probing depths larger than the grown crystals' thicknesses will also measure the properties of the underlying GaSe flakes. This will be taken into consideration when analyzing the characterization results.

6.3.1 Chemical composition analysis

The chemical composition of the grown crystals was studied by EDS with an electron accelerating voltage of 20 keV. At this accelerating voltage, the penetration depth of the EDS measurement should exceed 1 μm, which is larger than the grown-crystals and GaSe flakes thicknesses combined. The selenium signal from the underlying GaSe will overlap any potential signal from the grown crystals, overestimating the selenium content. Figure 6.3.b shows the grown crystals on the edge of a large GaSe flake (position 1) and on the surface of a smaller one (position 2). The chemical composition maps for positions 1 and 2 can be seen in Figures 6.3.c-e. It is clear that tellurium is only found at the grown crystals; on the other hand, the selenium signal weakens for the underlying GaSe, compared to the exposed surfaces. At position 1, the GaSe and grown-crystal thicknesses were around 165 nm and 455 nm, respectively. EDS determined that position 1 was 29% selenium-to-chalcogenide ratio ($x = 0.29$ for $GaSe_xTe_{1-x}$), a clear overestimation of the selenium content in the grown crystals. Similarly, an 11% selenium-

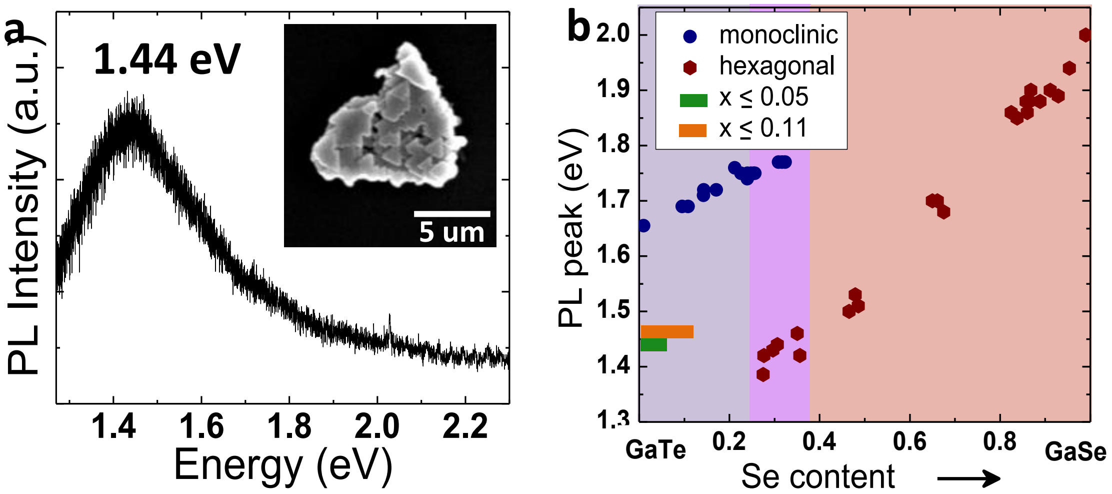

Figure 6.4. (a) PL spectrum showing an emission peak at 1.44 eV for dilute-selenide ($x \leq 0.05$) $GaSe_xTe_{1-x}$ crystals grown on GaSe. Grown crystals shown on inset. **(b)** PL peak dependence on the selenium content and crystal structure. Green bar used to indicate range of possible concentrations for the $x \leq 0.05$ sample with PL at 1.44 eV. Orange bar used to indicate range of possible concentrations for the $x \leq 0.11$ sample with PL at 1.46 eV.

to-chalcogenide ratio was estimated at position 2, where the GaSe and grown-crystal thicknesses were around 37 nm and 323 nm, respectively. The measured selenium content is an upper bound for the actual composition of the grown crystals. Thus, the hexagonal crystals at position 2 have $x \leq 0.11$, which is already an improvement from the results shown in the previous chapter.

6.3.2 Bandgap determination

The lowest selenium content measured belonged to the crystals shown in the inset of Figure 6.4.a. These hexagonal crystals have $x \leq 0.05$ and exhibited a weak PL peak at 1.44 eV, shown in Figure 6.4.a. We observed a similar PL peak for the $x \leq 0.11$ crystals in Figure 6.3.b, around 1.46 eV. This could imply that the grown crystals are pure *h*-GaTe with the selenium signal coming exclusively from the underlying GaSe, meaning that the direct bandgap of *h*-GaTe is around 1.44 – 1.46 eV. In contrast, this could also imply that the grown crystals are hexagonal dilute-selenide $GaSe_xTe_{1-x}$ alloys with a relatively constant bandgap. In either scenario, the results aim towards a direct bandgap around 1.45 eV for *h*-GaTe. Figure 6.4.b presents the PL peak dependence on the selenium content and crystal structure–similar to Figure 5.6.d–with the addition of the crystals discussed in this chapter. Elongated bars are used to represent the range of possible alloy compositions.

In Section 6.1 I discussed the theoretical calculations that indicated that *h*-GaTe was an indirect material with the direct gap about 0.1 eV larger. Photoluminescence measurements only probed the direct gap and agree very well with the reported 1.45 eV bandgap determined by optical transmission spectroscopy.[54] It is not uncommon for the smaller indirect gap to be unmeasurable through optical absorption spectroscopy in thin crystals, and the same could be true for *h*-GaTe.[93,161] The indirect gap, in turn, could be around 1.35 eV as predicted by the energy difference between the indirect and direct transitions or be as low as the 1.06 eV bandgap measured by scanning tunneling spectroscopy (STS).[158] Additionally, in Appendix A.9, the DFT calculations presented in Section 5.5 were fitted with the experimental bandgaps of the endpoints–including *h*-GaTe–with strong agreement throughout the composition range.

Chapter 7

Conclusions and future work

Layered semiconductors have shown great promise for thin optoelectronic applications beyond silicon and III-V semiconductors. The layered nature of these materials gives them unique mechanical, surface and optoelectronic properties that have attracted the interest of many researchers in the field. While the research efforts have focused mainly in just a handful of these semiconductors, several interesting and desirable properties have been also observed among the rest. Gallium telluride, for instance, possesses a direct bandgap in bulk and exhibits good unintentionally-doped p-type conductivity, and its in-layer structural anisotropy results in corresponding optoelectronic anisotropy, as mentioned in Chapter 1. This dissertation focused on some of these optoelectronic properties and on multiple mechanisms to deliberately modify them.

It was found that for GaTe a non-traditional avenue to modify the bulk properties was available. As discussed in Chapters 2 and 3, access to the interlayer space and to the layers' surfaces allows for the direct access to the semiconductor's properties. This behavior–exclusively available to layered materials–would also depend on the chemical stability of the layers' surfaces and interacting species. A tellurium-rich surface seems ideal for this, as the larger and more polarizable Te atom should be able to interact with other species despite being covalently bonded to metal atoms. In addition, this mechanism has the particular advantage that it can be reversible. Even though only partial reversibility was demonstrated in Chapter 3, it indicates that the binding energy between the interacting specie (oxygen) and the Te atom is weak. In fact, given that the partial reversibility was only observed near surface defects, the problem might be related to kinetics which might be overcome by longer annealing process and shorter diffusion paths–smaller samples. Unfortunately, the mechanism is highly dependent on the surface-defect density of the crystal as they facilitate the diffusion of the species through the layers. Therefore, high-quality as-grown or annealed crystals might not be ideal candidates for this process.

Chapters 5 and 6 focused on the growth and characterization of the $GaSe_xTe_{1-x}$ alloy system and *h*-GaTe metastable structure. It was found that the vapor-deposited crystals would normally exhibit distinct morphologies and sizes depending on the crystal structure, chemical composition and growth direction. Such behavior allowed for the rapid identification of crystal structure and orientation, and in some instances even for the broad estimation of chemical composition. Further, this could facilitate the study of orientation-dependent properties in highly anisotropic materials like *m*-GaTe and *m*-$GaSe_xTe_{1-x}$.

The growth of alloy crystals with compositions between x = 35 and x = 0.70 was also demonstrated in Chapter 5. Bulk crystals within this composition range accumulate internal stresses resulting in phase separation. However, the growth of small and thin hexagonal crystals by vapor deposition allowed for the relaxation of such stresses, stabilizing the crystals with mid compositions. For the *h*-GaTe, in addition to the vapor deposition of small and thin crystals, an additional hexagonal substrate was needed to induce the hexagonal growth. As tellurium is added to the hexagonal structure, internal stresses increase which were evident by the decrease in crystal size and eventual need of a van der Waals epitaxial substrate.

The bandgap dependency on composition for the $GaSe_xTe_{1-x}$ alloy was also discussed. It was found that for the monoclinic structure the bandgap seemed to follow a virtual crystal approximation while the hexagonal structured exhibited an apparent bowing of the direct bandgap. Experimentally, the minimum bandgap was observed for x = 0.28 but the calculations trend predicts it to be around x = 0.15. It's clear that the $GaSe_xTe_{1-x}$ system is complicated and its alloys can have properties beyond those of the pure-compound endpoints.

There are many other important optoelectronic properties beyond the bandgap that will determine or influence a materials ability to perform in many applications. In Chapter 4, the band edges alignment and shallow-defects energy levels of unintentionally doped GaTe were determined. Two acceptor levels–generally attributed to Ga vacancies–and one donor defect–possibly Te vacancy–were observed. There are still many other interesting and essential GaTe properties that I was not able to cover in this dissertation. Hopefully, the observations and findings presented here will help to further understand the properties of GaTe and how to engineer them for our advantage. Furthermore, the ideas and methods discussed here could be applied for other layered semiconductors, contributing to the development of the field.

7.1 Future work

There's still much work to be done on the bandgap engineering of GaTe and in the field of layered semiconductors in general. We can and should build upon the accomplishments and developments presented in this work, as it will be discussed here.

There is a need to develop modern mechanisms to controllably modify the optoelectronic properties of layered materials akin to the one discussed in Chapter 2. As mentioned above, this mechanism might be best suited for layered telluride semiconductors–GaTe and 2H-$MoTe_2$–but can be adapted for other materials. The prolonged exposure of certain layered materials to species with different chemical properties might result in the modification of their properties, similar to the GaTe–O_2 transformation or to surface-transfer doping.[162]

The alloying of GaTe with other layered semiconductors would significantly contribute to the understanding of these materials, similar to the results found in the $GaSe_xTe_{1-x}$ alloy system. Current efforts to grow and characterize the GaS_xTe_{1-x} alloy system are being made by fellow group member Edy Cardona. In this system, the large size and electronegativity difference between sulfur and tellurium atoms might result in a highly mismatched alloy with extreme bandgap bowing.[84,90] Interestingly, alloying GaTe with the remaining III-VI monochalcogenide, InSe, might be as or even more promising. As discussed in Chapter 1, InSe tends to exhibit unintentionally-doped n-type behavior, but it has also been successfully doped n-type and p-type with high carrier mobilities.[47-50] This should allow for the growth of n-type and p-type $(InSe)_x(GaTe)_{1-x}$ pseudo-binary alloys, and possibly p-n homojunctions. Structurally, InSe has longer bond lengths and thicker layers than GaSe which should better accommodate the larger Te atoms, further stabilizing the hexagonal-layer structure–rhombohedral layer assembly.[45] Further fine tuning of the bandgap and doping levels can also be achieved by independently adjusting the compositions, treating $In_yGa_{1-y}Se_xTe_{1-x}$ as a quaternary alloy instead of a pseudo-binary.

Beyond the III-VI monochalcogenides, GaTe could be alloyed with other layered and perhaps some non-layered semiconductors. Specifically, it is of interest to study the behavior of alloys between GaTe and other telluride semiconductors like $MoTe_2$, WTe_2 and MnTe. Alloys with the layered transition-metal ditellurides could result in significant bandgap, doping and phase changes, especially considering that most of them exhibit semimetallic behavior.[22,78] However, the difference in stoichiometry and crystal structure will difficult the growth of the alloy beyond the dilute compositions, needing approaches similar to the ones used in this dissertation to stabilize stressed and metastable structures. Other interesting properties like thermopower and magnetism could also be explored with these alloys. For example, it has been shown that the thermopower of $MoTe_2$ can be significantly enhanced by alloying it with other layered telluride semiconductors, which could apply to GaTe as well.[163] On the other hand, MnTe is a non-layered semiconductor with the same stoichiometry as GaTe that has been shown to possess magnetic properties.[164] It would be of great interest to determine the capacity of incorporation of a non-layer material into a layered structure and the extent of the contribution of its properties to the layered alloy. In the small picture, this could result in giving $Ga_{1-x}Mn_xTe$ magnetic properties; while in the larger picture, it would open a whole new class of possible combinations and properties for layered semiconductors.

In Chapter 6, thin *h*-GaTe crystals were grown on the surface of GaSe flakes resulting in as-grown p-p heterojunctions. Similarly, the mixed-phase $h\text{-}GaSe_xTe_{1-x}/m\text{-}GaSe_xTe_{1-x}$ alloy crystals presented in Appendix A.8 also correspond to p-p heterojunctions. These as-grown devices still need further characterization of their optoelectronic properties, but even now could serve as models for more interesting and complicated assemblies. By replacing the GaSe flakes for InSe in order to grow *h*-GaTe, p-n heterojunctions with improved electronic transport properties could be designed. The same would hold true by replacing the GaSe flakes with any of the numerous hexagonal TMD semiconductors. There are still many questions to be answered and opportunities to be explored about GaTe and layered semiconductors. Knowing that these materials will play an important role on the future of electronic devices, I'm grateful that this dissertation will contribute to broaden the knowledge on this field.

Appendix A

Additional figures and data

A.1 Photomodulated Reflectance

Photomodulated reflectance (PR) spectroscopy is a technique that can be used to determine the direct optical transitions in a semiconductor. This is done by measuring the wavelength-dependent difference in reflectance before and after increasing the free-carrier concentration with a laser pump. The change in free-carrier concentration will modify the dielectric constant, specifically around the energies corresponding to direct transitions.

Figure A.1 shows the PR spectra of freshly cleaved and transformed GaTe flakes, at room temperature. For the freshly cleaved sample, the direct transition corresponding to the bandgap is observed around 1.67 eV. The spin orbit (SO) transition is observed at higher energies, around 2.3 eV. In contrast, no clear direct transition is observed for the transformed sample. These measurements were taken by pumping the samples with a 442 nm HeCd laser, and the signal is detected by a Si detector using the lock-in technique. These measurements were taken together with Dr. Alex Luce.

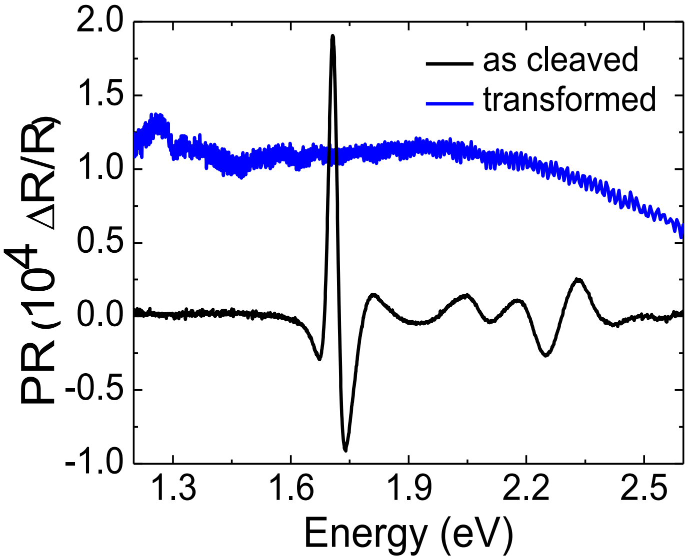

Figure A.1. Photomodulated reflectance spectra of freshly cleaved (black) and transformed (blue) GaTe. The direct transition can be observed at around 1.67 eV.

A.2 X-ray photoelectron spectroscopy

X-ray photoelectron spectroscopy (XPS) is a technique that probes the chemical environment of atoms at and near the surface of a material. This technique takes advantage on the photoelectric effect to determine the binding energy of the emitted electron, excited by an x-ray source. The binding energy of the electron will depend on the chemical identity and the oxidation state of the atom. The higher the oxidation state of an atom, the higher the binding energy.

Figure A.2 shows the high-resolution XPS spectra of the tellurium and oxygen core levels. The evolution of the tellurium and oxygen peaks is observed over time. It is noted that even after two weeks of air exposure, some of the tellurium atoms exhibit no change on their oxidation condition. This means that some tellurium atoms at the surface remain in a similar chemical environment as in pristine GaTe. These measurements were carried out by using a non-monochromatic Al Kα X-ray source (1486.6 eV) and a hemispherical-type multi-channel analyzer in vacuum (base pressure of $\approx 1\times10^{-10}$ torr). The binding energies are referenced by direct electrical contact to the Fermi energy of the spectrometer whose work function is 4.5 eV. These measurements were taken by Dr. Changhyun Ko at the Molecular Foundry.

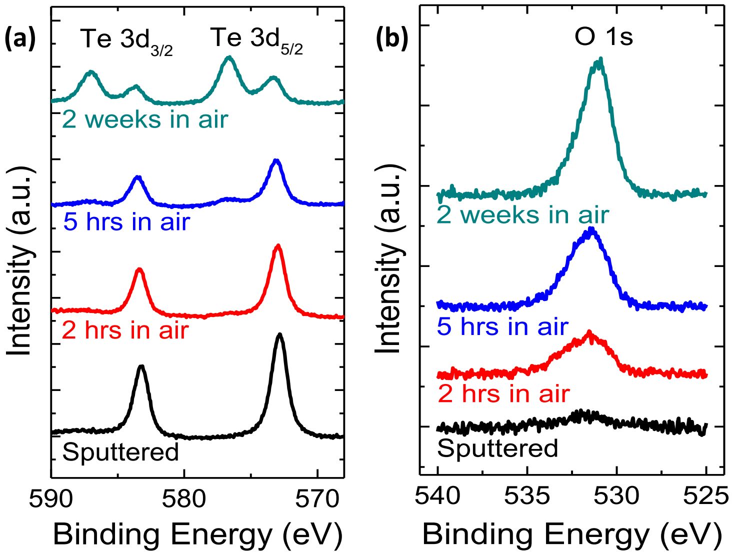

Figure A.2. X-ray photoelectron (XPS) spectroscopy of GaTe. High-energy-resolution XPS of the **(a)** tellurium and **(b)** oxygen core levels at different times of the GaTe transformation. The “sputtered” sample was sputtered in the ultra-high vacuum chamber to remove any native oxide. These spectra show that even after 2 weeks in air, not all the Te atoms near the surface are oxidized, meaning that some are still in a similar chemical environment as in pristine GaTe.

A.3 Raman active modes

Figure A.3 shows the experimental Raman spectra of freshly cleaved and transformed GaTe, and the calculated Taman-active modes for GaTe and GaTe–O_2. It can be seen that the Raman peaks observed in the as-cleaved samples match with some of the active modes of GaTe, similar for the Raman peaks of the transformed samples and the Raman-active modes of GaTe–O_2. Details on the calculation of the Raman modes are shown in Appendix B.2.

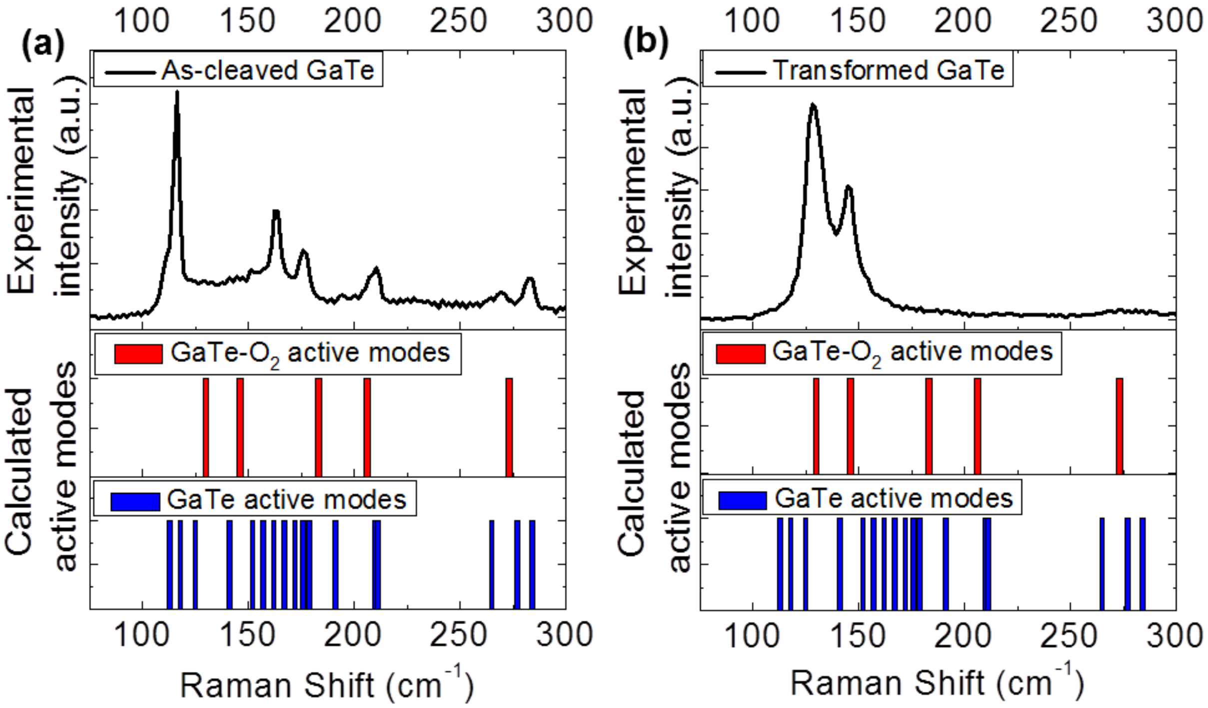

Figure A.3. Calculated Raman-active modes of GaTe and GaTe–O_2, compared to the experimental Raman spectra of **(a)** as-cleaved GaTe and **(b)** transformed (air-exposed) GaTe

A.4 Ion irradiation simulation

Figure A.4 shows a cross-sectional schematic of the ion-irradiation process and range-of-damage simulations. For the ion irradiation studies, He^+ ions were irradiated normal to the GaTe layers, and samples surface. To guarantee that the vacancy formation along the samples thickness was relatively constant and that the range of maxiumum damage occurred far from the sample, Monte-Carlo simulations were done. The Stopping and Range of Ions in Matter (SRIM) software was used to simulate the number of vacancies formed in GaTe after ion irradiation.[165] The curves are a sum of independent Ga and Te vacancies, which were equal in magnitude. The curves for both 3 and 4 MeV He^+ irradiation energies are shown to illustrate the range difference caused by a shift in energy and the possible variance of ion energy due to the instrument. The ion irradiation process was done by Jeffrey W. Beeman at Lawrence Berkeley National Lab.

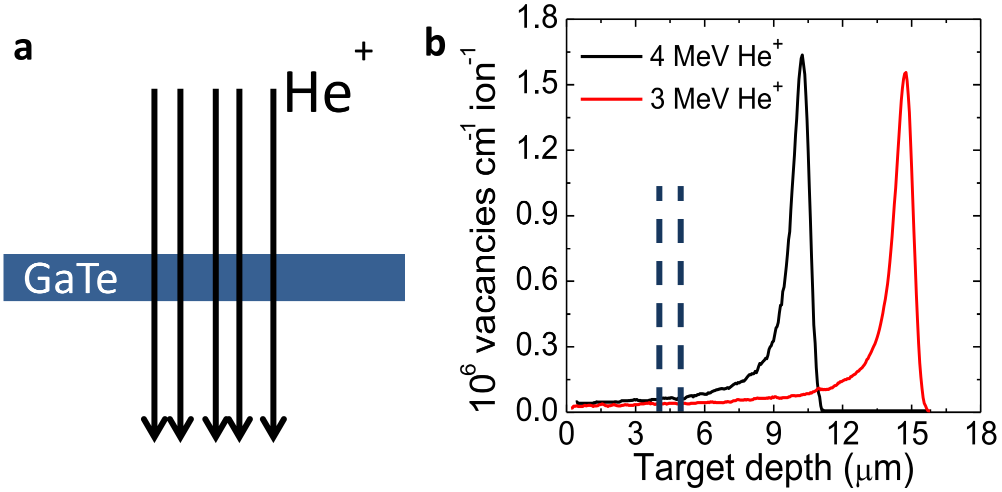

Figure A.4. (a) Cross-sectional representation of He^+ ion irradiation studies. Ions irradiated normal to GaTe's layer planes and transmitting through the sample's thickness. **(b)** Monte-Carlo simulations, done with the Stopping and Range of Ions in Matter (SRIM) software, of vacancies formed in GaTe as a function of target depth caused by 3 and 4 MeV He^+ irradiation. The range of sample width is illustrated by the dashed lines.

A.5 Additional low-temperature photoluminescence of GaTe

Complementary data to that shown in Figure 4.4 and discussed in Section 4.2 is shown below.

A.5.1 High excitation-intensity photoluminescence

Figure A.5.a shows the PL spectra of GaTe for excitation intensities greater than 50 mW. At these higher intensities, local heating occurs, resulting in the broadening and red-shift of the free-exciton (*FX*) peak. Quenching of the acceptor-bound exciton (*AX*) peaks with increasing intensity is also observed. Figure A.5.b, instead, shows that the donor-acceptor pair (*DAP*) and the free-to-acceptor-bound (FB_A) peaks remain even at higher excitation intensities and at about the same energy. This observation is expected as neither of these two transitions involve an exciton. However, for the 600 mW excitation PL we observe that the *DAP* peaks have started to quench and the FB_A peaks have almost completely quenched, which is expected at even higher temperatures, where only the free-exciton peak is observed.

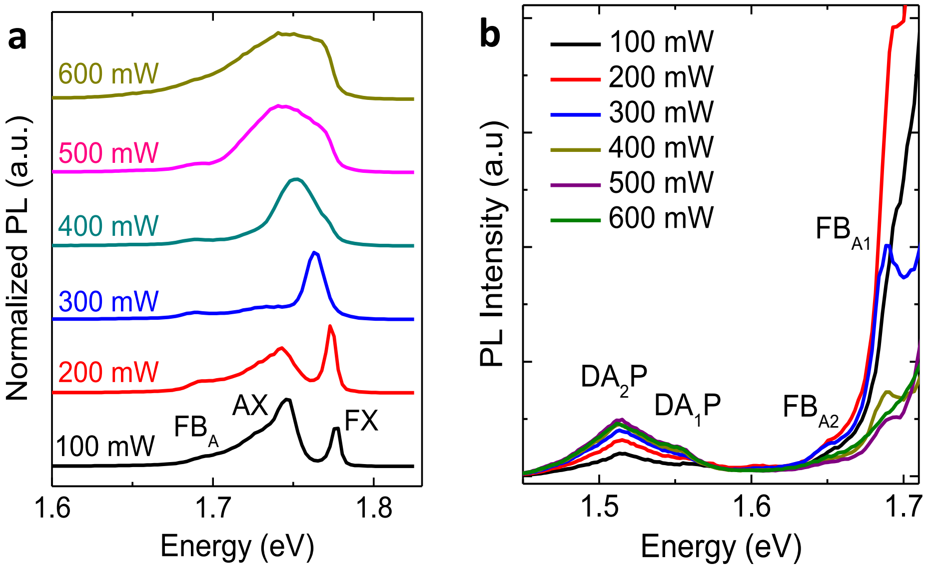

Figure A.5. Low-temperature photoluminescence spectra of GaTe with excitation intensities from 100 – 600 mW, at 12 K. **(a)** Normalize PL spectra from 1.60 – 1.83 eV. **(b)** PL spectra from 1.45 – 1.70 eV.

A.5.2 Photoluminescence of ion-irradiated GaTe

Figure A.6 shows the low-temperature PL spectra of He^+ irradiated GaTe for excitation intensities between 1.6 – 50 mW, similar to Figure 4.4. As discussed in Section 4.1, the ion irradiation of GaTe resulted in the generation of donor-like native defects that partially compensated the hole concentration by an order of magnitude. This considerable increase in point defects and decrease in crystal quality had significant effects on the PL spectra of GaTe. The most noticeable change in the PL spectra is the disappearance of the *DAP* transitions. In addition, the *FX* peak is now at 1.769 eV, about 9 meV lower than the non-irradiated samples, which would imply an exciton binding energy (E_X) of 27 meV, instead of 18 meV. In contrast, we observe that the FB_A peaks remain relatively constant in energy, meaning that the Ga vacancy acceptor levels do not change. When taking into account the new exciton binding energy, the measured energy values of the *AX* peaks agree with the ones calculated using Equation 4.5 in Section 4.1.

Given the lack of *DAP* transitions, it is difficult to determine whether the donor-like native defects created by ion irradiation are similar in nature to the donor defects present in the non-irradiated sample. In Section 4.2, it was determined that the donor level in the non-irradiated samples was around 130 meV below the conduction band minimum. This energy level would correspond to a free-to-donor-bound (FB_D) and a donor-bound exciton (*DX*) transitions around 1.668 and 1.731 eV, respectively, which overlap with FB_{A2} and A_2X.

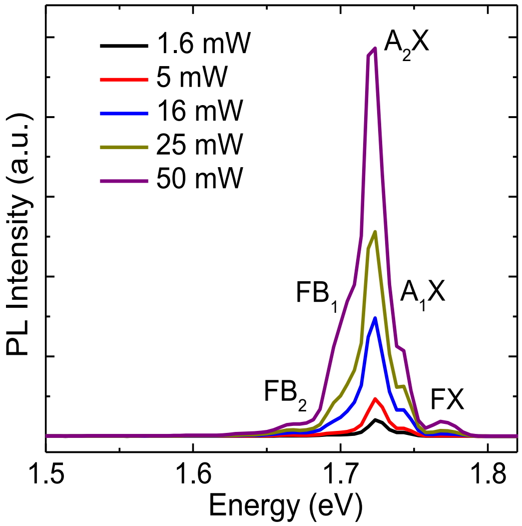

Figure A.6. Low-temperature photoluminescence spectra of ion-irradiated GaTe with different excitation intensities, at 12 K.

A.6 Furnace temperature profile

Figure A.7 shows the temperature profile of the one-zone quartz tube reactor used for vapor-deposition growth. Different colored-curves correspond to different setpoint temperatures. Measurements were taken with an external Type-K thermocouple in a closed secondary-quartz-tube sleeve, without touching the tube reactor walls.

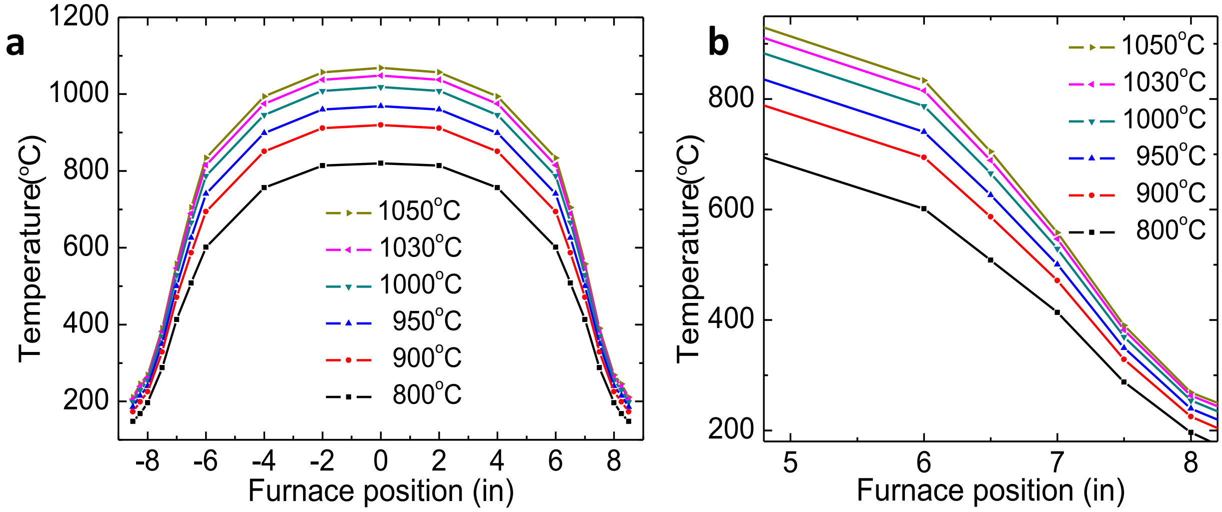

Figure A.7. **(a)** Furnace temperature profile for given temperature setpoints: 800 °C, 900 °C, 950 °C, 1000 °C, 1030 °C, 1050 °C. **(b)** Closer look at the temperature profile around the substrates position.

A.7 Raman spectra of GaSe$_x$Te$_{1-x}$

The observed Raman spectra for monoclinic and hexagonal GaSe$_x$Te$_{1-x}$ is shown in Figures A.8.a,b, respectively. It can be seen how the sharp peaks observed near the pure compounds, tend to broaden towards the the mid-compositions. Figure A.8.c shows the peaks dependence on crystal structure and composition, similar to the behavior previously reported.[102] In the monoclinic structure, with the exception of the peaks at 116 and 284 cm^{-1}, the Raman peaks are not heavily dependent of composition. For the hexagonal structure, most peaks are noticeably dependent on composition, as they tend to soften with the addition of tellurium.

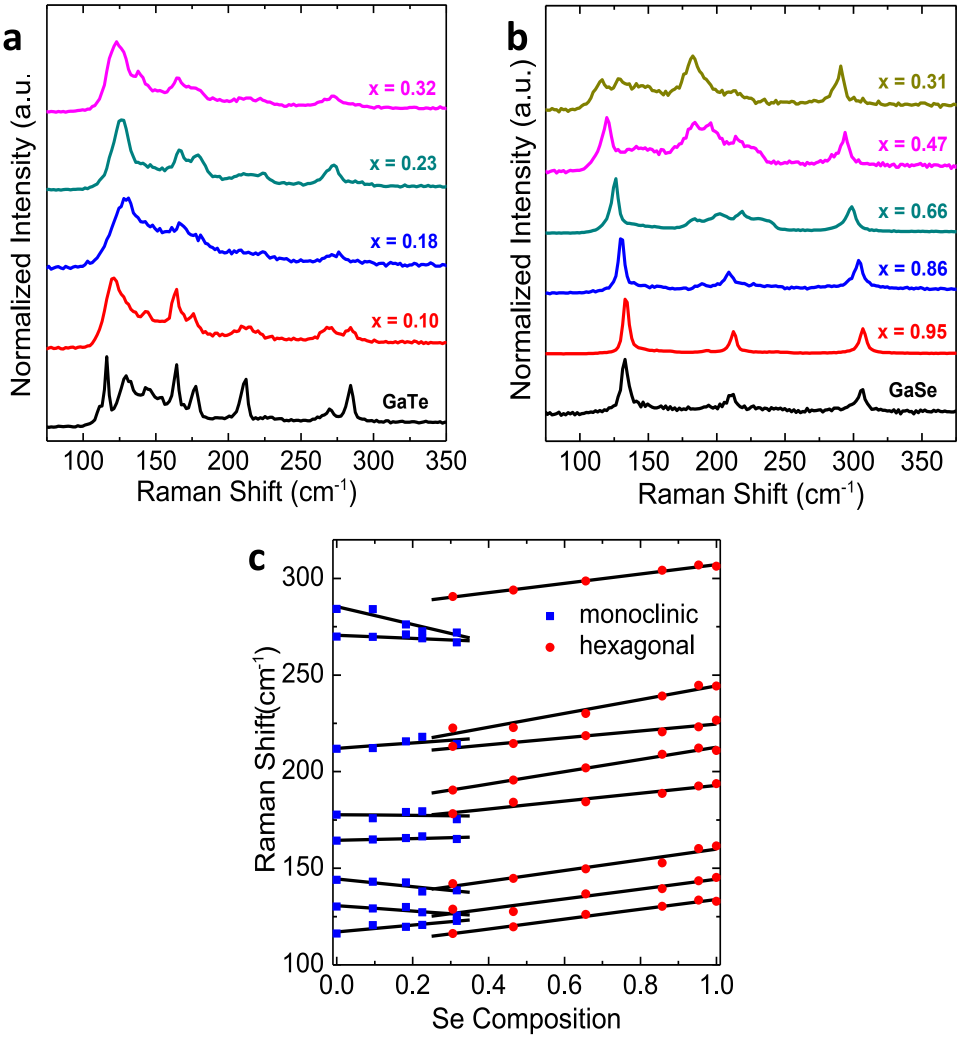

Figure A.8. Raman spectra of **(a)** monoclinic and **(b)** hexagonal GaSe$_x$Te$_{1-x}$. **(c)** Raman peaks position dependence on crystal structure and composition.

A.8 $GaSe_xTe_{1-x}$ mixed-phase crystals

In addition to the single-phase $GaSe_xTe_{1-x}$ crystals discussed in Chapter 5, we were also able to grow some mixed-phase crystals, as seen in Figures A.9.a,b. In all of the mixed-phase crystals found, it was observed that the hexagonal phase grew on top and near the center of a monoclinic crystal, as indicated in Figures A.9.c,d. Interestingly, it seems that the hexagonal phase grows in the serrated structure–along the zig-zag direction–regardless if the monoclinic crystal grew along the $b_{\perp}$- or $b_{\parallel}$-axis, Figures A.9.a and A.9.b, respectively. The chemical composition measured for the mixed-phase crystals ranged from $0.14 < x < 0.31$, which is comparable to the overlap region. Specifically, the compositions measured for the crystals shown in Figures A.9.a and A.9.b are $x = 0.31$ and $x = 0.29$, respectively. However, it is worth noting that, just as stated in Chapter 6, it is difficult to deconvolute the contributions of each layer to the chemical composition measurements in these multi-phase vertical assemblies.

Figures A.9.e,f show the PL spectra of the crystals shown in Figures A.9.a and A.9.b, respectively. In Figure A.9.e, a weak PL signal at 1.79 eV is obtained for the monoclinic layer, while a significantly stronger signal from the thicker hexagonal layer is measured at 1.36 eV. In contrast, in Figure A.9.f, only a weak PL signal is obtained from the thin hexagonal layer at 1.37 eV and a strong signal at 1.75 eV from the monoclinic layer underneath. The dependence of the PL peak energies of the mixed-phase crystals, on the crystal structure and composition, can be seen in Figure A.10a,b–illustrated by open pink squares. The dependence appears to be in good agreement with that of the single-phase crystals; the slight deviations should be corrected with more accurate composition measurements in each phase.

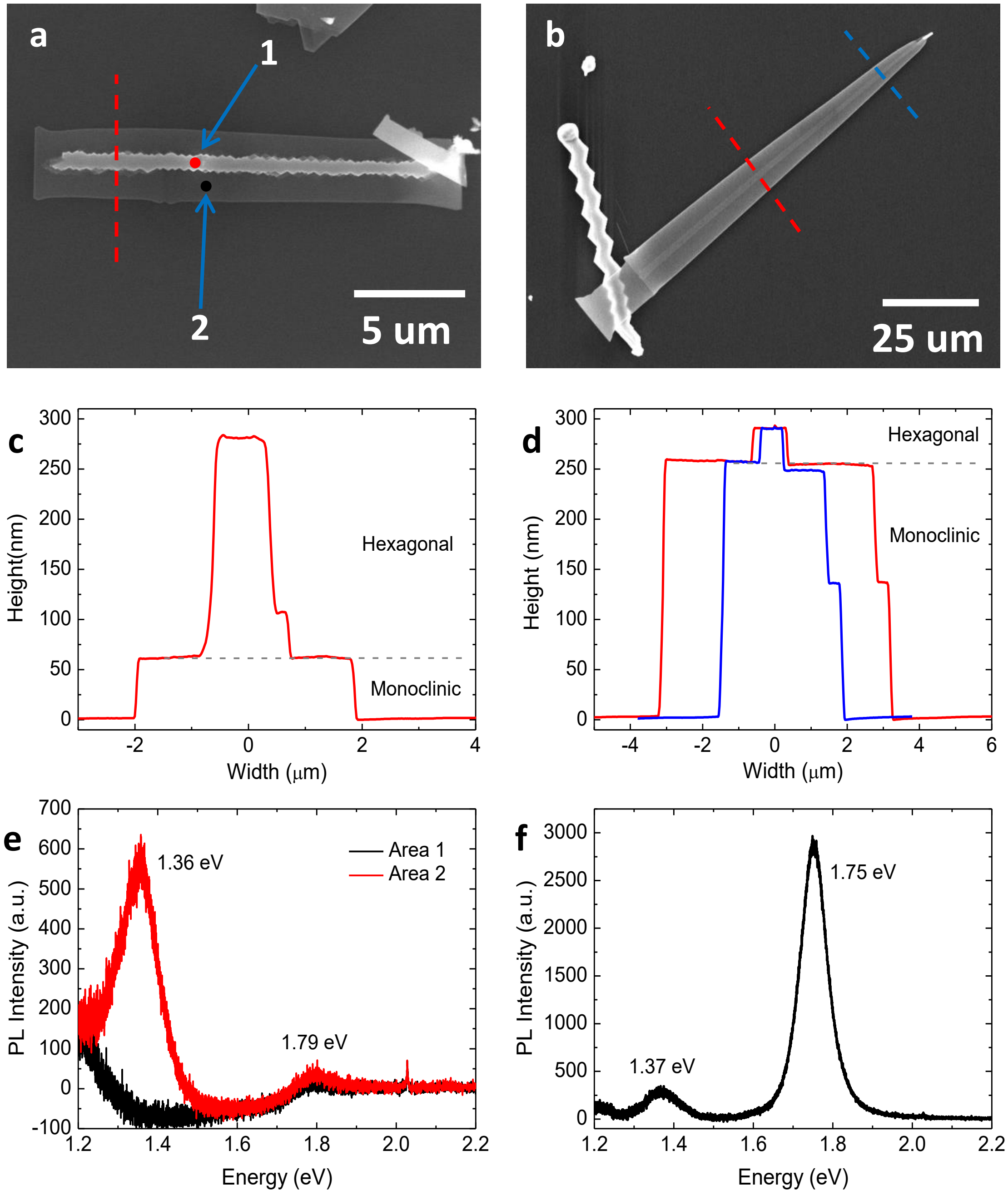

Figure A.9. Scanning electron micrographs of GaSe$_x$Te$_{1-x}$ mixed-phase crystals with **(a)** thicker hexagonal layer and **(b)** thicker monoclinic layer. **(c)-(d)** Height profiles of **(a)** and **(b)**, respectively, illustrating the difference in thickness between the monoclinic and hexagonal parts. **(e)-(f)** PL spectra of crystals in **(a)** and **(b)**, respectively. PL spectra shown in **(e)** correspond to bare monoclinic layer (area 1) and mixed-phase crystal with thick hexagonal layer (area2). PL peaks energies are indicated in **(e)** and **(f)**.

A.9 GaSe$_x$Te$_{1-x}$ DFT calculations fitting

It is known that DFT calculations with the PBE fuctional commonly underestimate the bandgap energy of semiconductors, while appropriately representing the bandgap trends, as mentioned in Section 5.5. To improve the bandgap estimation, linear fittings were done taking into account only the endpoints of the alloys. Figure A.10.a shows the fitting obtain by only taking into account the two hexagonal endpoints, *h*-GaTe and GaSe. Figure A.10.b shows the fitting obtain by only taking into account all three endpoints, *m*-GaTe, *h*-GaTe and GaSe. The linear fits obtain for each figure are $y = 1.735x - 0.0213$ and $y = 1.740x - 0.0460$, respectively. Overall, the fitting in Figure A.10.b seemed more accurate, and it predicted an indirect bandgap of *h*-GaTe around 1.28 eV. It can be seen that even the experimental PL peaks obtained for the mixed-phase crystals are in good agreement with the fitting, even with the uncertainty on their composition.

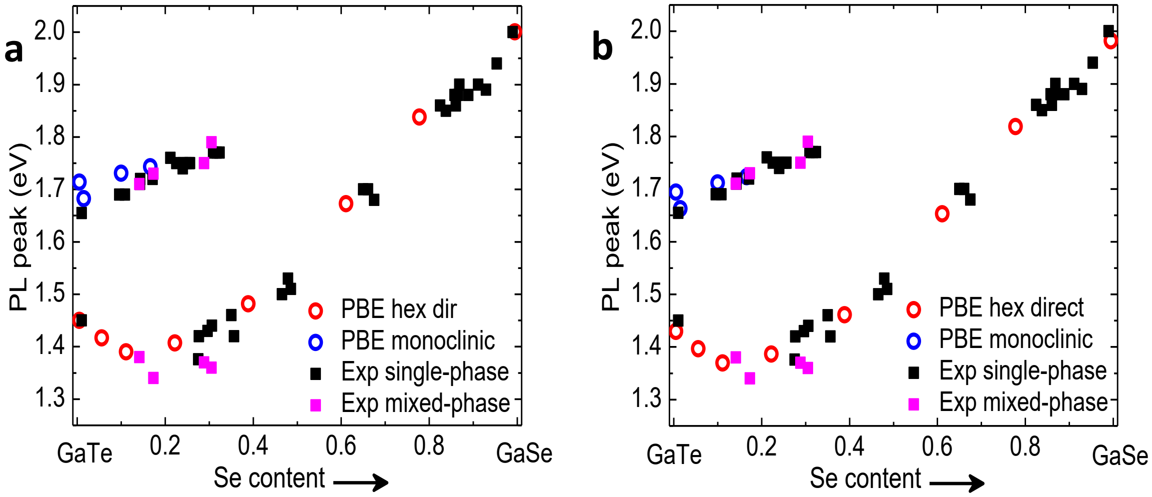

Figure A.10. DFT-calculated bandgaps for the GaSe$_x$Te$_{1-x}$ alloys using the PBE exchange-correlation functional fitted using the experimental bandgaps of **(a)** the two hexagonal endpoints and **(b)** all three endpoints. Experimental PL peak data of single-phase (closed black squares) and mixed-phase (open pink squares) crystals presented for reference.

Appendix B

Additional methodology and analysis

B.1. X-ray diffraction

The XRD measurements were performed in collaboration with Annabel R. Chew from the Salleo group at Stanford University. For the measurements, as-exfoliated GaTe flakes were mounted on silicon wafers using copper tape. X-ray measurements were periodically carried out on the flakes to study the GaTe-O2 transformation process, using a laboratory-based PANalytical X'Pert PRO diffractometer. In the diffractometer, a Cu K_α X-ray (8.04 keV) source was used to study the samples under room temperature conditions. A monochromator was used to filter out the Cu $K_\alpha 2$ line. All measurements were carried out at room temperature.

B.1.1. GIXD penetration depth calculation

The penetration depth of the X-rays used in the grazing incidence XRD is defined as the depth at which the intensity drops by a factor of 1/e.[110,111] The thickness of the GaTe flake studied in Figure 2.7.a was determined by the following equations and constants using the PANalytical HighScore X-ray Diffraction software.

$$I_L = I_o e^{-\mu L} \tag{B.1}$$

$$d = \sin(\omega)/\mu \tag{B.2}$$

I_L is the diffracted intensity at a given depth L, I_0 is the diffracted intensity right at the surface, μ is the linear absorption coefficient of GaTe for 8.04 keV x-rays (1.105×10^3 cm^{-1}), and d is the penetration depth.

Table B.1. Corresponding X-ray penetration depths based on the measured grazing angle of incidence using the GIXD geometry.

Grazing angle, ω (^{o})	Penetration depth, d (μm)
0.1	0.036
0.3	0.109
0.5	0.182
1	0.364
2	0.727
3	1.091
5	1.816

B.1.2. Peak broadening analysis

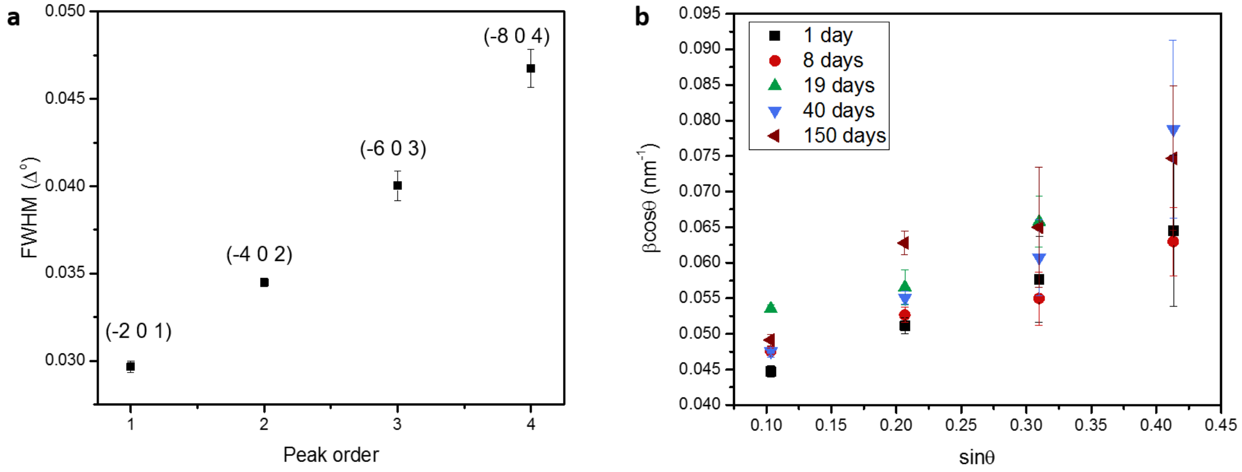

Figure B.1. (a) Representative plot showing peak broadening to peak order. The measured full-width at half maximum (FWHM) of the {-2 0 1} family of peaks versus peak order for the GaTe flakes. The data shown here is for the sample measured one day after exfoliation. **(b)** Williamson-Hall plot for each sample, labeled according to the number of days after exfoliation at which the measurement was taken.[112,113] Error bars on both the x and y axes are shown.

Table B.2. Linear fit parameters obtained for the Williamson-Hall plots shown in Figure B.1.b.

Time (days after exfoliation)	Slope	Intercept
1	0.1562 ± 0.0001	0.03825 ± 0.00006
8	0.012 ± 0.001	0.0428 ± 0.0005
19	0.012 ± 0.002	0.041 ± 0.001
40	0.018 ± 0.001	0.040 ± 0.001
150	0.029 ± 0.005	0.037 ± 0.002

B.2. GaTe–O_2 DFT calculations

GaTe–O_2 DFT calculations were performed in collaboration with Dr. Mehmet Topsakal at University of Minnesota. Structural relaxations and phonon calculations were carried out using the Perdew–Burke–Ernzerhof (PBE) exchange-correlation functional including van der Waals corrections.[166,167] For band structure and density-of-states (DOS) calculations the Heyd–Scuseria–Ernzerhof (HSE) functional was used, which is a screened hybrid functional introduced by Heyd, Scuseria, and Ernzerhof.[168] One quarter of the PBE short-range exchange is replaced by exact exchange while the full PBE correlation energy is included. This hybrid functional was shown to yield improved band gaps compared to PBE functional.[169] The interaction between the ions and valence electrons are described by the projected augmented wave (PAW) method with a plane wave cutoff of 340 eV.[170]

Brillouin-zone integrations were performed using (4x4x4) Monkhorst-Pack grids. All atomic positions and lattice constants are optimized using the conjugate gradient method in which total energy and atomic forces are minimized. Effects of oxygen intercalation are simulated by adding an oxygen molecule into 2x1x1 supercell of monoclinic GaTe structure (which we denote henceforth as GaTe–O_2) containing 12 Ga and 12 Te atoms. The same simulation cell is retained for pristine GaTe. The character of phonon modes, whether infrared (IR) or Raman active, is determined according to IR-active mode intensities. DFT calculations were performed using Vienna Ab-initio Simulation Package (VASP) code.[171]

B.3. Gold nanoparticles deposition

Gold nanoparticles (20 nm, Sigma-Aldrich) were deposited on the silicon substrates by the procedire indicated by Patolsky, et al.[172] First, the silicon substrates were solvent cleaned in a mixture of acetone and isopropyl alcohol for 20 minutes in a sonicator bath. The substrates were then rinsed with diH_2O and blowed-dry with nitrogen. The surfaces were then plasma cleaned with oxygen for 5 minutes, making the surface hydrophilic. After, the substrates were covered with a thin liquid film 0.1% w/v aqueous poly-L-lysine (Ted Pella) for 2 minutes. The poly-L-lysine was rinsed with diH_2O and blowed-dry with nitrogen, leaving a positively-charged self-assembled layer. A diluted gold nanoparticle solution (1:4 v/v with diH_2O) was used to cover the silicon substrates surfaces for 10 seconds, before rinsing with diH_2O and blow-drying with nitrogen. The dilution of the gold nanoparticles before deposition helps to disperse the particles and break any clusters formed during storage. The negatively charged gold nanoparticles are electrostatically atracted to the poly-L-lysine, improving nanoparticle adsorption. Finally, the silicon substrates are oxygen-plasma cleaned again for 5 minutes, to remove any organics including the poly-L-lysine. Soon after, the substrates were introduced into the quartz-tube reactor for vapor-deposition growth.

B.4. Micro-optical absorption

The micro-optical absorption was performed in collaboration with Kyle Tom from the Yao group at UC Berkeley. The absorption edge was calculated from the transmission and reflection spectra. White light from a quartz tungsten source (LSH-100, Horiba) was reflected by a sapphire beam splitter and focused on the surface of samples by a 40× objective lens. A cutting edge aperture was placed at the image plane behind the beam splitter to select sample area (~50 mm diameter) from the reflected light. Then the selected light is focused into a spectrometer (iHR320, Horiba) and normalized to the reflection spectrum of a 100 nm gold film. Transmission measurements were performed with a similar setup, but with the light passing through a separate lens that focuses on the sample through the glass substrate before being focused into the spectrometer. Transmission measurements were normalized to the transmission spectrum of glass.

B.5. GaSe$_x$Te$_{1-x}$ DFT calculations

GaSe$_x$Te$_{1-x}$ DFT calculations were performed in collaboration with Dr. Matthew K. Horton at Lawrence Berkeley National Lab. The calculations are performed using VASP and the PAW method, with pseudopotentials treating Ga 3d electrons as valence electrons.[170,173] A plane-wave cut off of 520 eV and a k-point mesh of 500 k-points per reciprocal volume for density of states calculations. Geometry optimisations were performed using the PBE exchange-correlation functional and lattice parameters obtained by Vegard's law with relaxed structures.

Bandstructures and density of states were also calculated using the Tran-Blaha modified-Becke Johnson potential.[153] This potential is known to give more accurate results than the PBE functional, and comparable results to quasiparticle GW calculations without the computational overhead.[154] The potential has one free parameter, c, which is calculated self-consistently as a function of the calculated electron density, not adding extra empiricism.

For the alloy compositions, a supercell containing a random alloy configuration was used, with a (3,3,1) supercell containing 72 atoms in the hexagonal phase (P6$_3$/mmc). This approach has been found to be robust even in the case of smaller supercells, with < 0.05 eV difference compared to the more complex quasirandom supercell method.[174,175] For each composition, two separate calculations were performed and averaged. Crystal structures for the end-points were obtained from the Materials Project,[152] and random supercells were constructed with the aid of the Python package pymatgen.[176]

References

[1] M. Schulz, *Nature* **1999**, *399*, 729.

[2] R. R. Schaller, *Spectrum, IEEE* **1997**, *34*, 52.

[3] R. Puers, L. Baldi, M. van de Voorde, S. E. van Nooten, Eds. , *Nanoelectronics: Materials, Devices, Applications*, Wiley-VCH, **2017**.

[4] K. F. Mak, C. Lee, J. Hone, J. Shan, T. F. Heinz, *Phys. Rev. Lett.* **2010**, *105*, 136805.

[5] M. Chhowalla, H. S. Shin, G. Eda, L.-J. Li, K. P. Loh, H. Zhang, *Nat. Chem.* **2013**, *5*, 263.

[6] J. Mann, Q. Ma, P. M. Odenthal, M. Isarraraz, D. Le, E. Preciado, D. Barroso, K. Yamaguchi, G. von Son Palacio, A. Nguyen, T. Tran, M. Wurch, A. Nguyen, V. Klee, S. Bobek, D. Sun, T. F. Heinz, T. S. Rahman, R. Kawakami, L. Bartels, *Adv. Mater.* **2014**, *26*, 1399.

[7] Y. Chen, J. Xi, D. O. Dumcenco, Z. Liu, K. Suenaga, D. Wang, Z. Shuai, Y. S. Huang, L. Xie, *ACS Nano* **2013**, *7*, 4610.

[8] K. S. Novoselov, A. K. Geim, S. V. Morozov, D. Jiang, Y. Zhang, S. V. Dubonos, I. V. Grigorieva, A. A. Firsov, *Science (80-.).* **2004**, *306*, 666.

[9] a K. Geim, K. S. Novoselov, *Nat. Mater.* **2007**, *6*, 183.

[10] K. I. Bolotin, K. J. Sikes, Z. Jiang, M. Klima, G. Fudenberg, J. Hone, P. Kim, H. L. Stormer, *Solid State Commun.* **2008**, *146*, 351.

[11] C. Lee, X. Wei, J. W. Kysar, J. Hone, *Science (80-.).* **2008**, *321*, 385.

[12] Y. Zhang, T.-T. Tang, C. Girit, Z. Hao, M. C. Martin, A. Zettl, M. F. Crommie, Y. R. Shen, F. Wang, *Nature* **2009**, *459*, 820.

[13] M. Y. Han, B. Özyilmaz, Y. Zhang, P. Kim, *Phys. Rev. Lett.* **2007**, *98*, 206805.

[14] J. T. Robinson, J. S. Burgess, C. E. Junkermeier, S. C. Badescu, T. L. Reinecke, F. K. Perkins, M. K. Zalalutdniov, J. W. Baldwin, J. C. Culbertson, P. E. Sheehan, E. S. Snow, *Nano Lett.* **2010**, *10*, 3001.

[15] Q. H. Wang, K. Kalantar-Zadeh, A. Kis, J. N. Coleman, M. S. Strano, *Nat. Nanotechnol.* **2012**, *7*, 699.

[16] K. F. Mak, J. Shan, *Nat. Photonics* **2016**, *10*, 216.

[17] Y. Li, K.-A. N. Duerloo, K. Wauson, E. J. Reed, *Nat. Commun.* **2016**, *7*, 10671.

[18] S. Z. Butler, S. M. Hollen, L. Cao, Y. Cui, J. A. Gupta, H. R. Gutie, T. F. Heinz, S. S.

Hong, J. Huang, A. F. Ismach, E. Johnston-halperin, M. Kuno, V. V Plashnitsa, R. D. Robinson, R. S. Ruoff, S. Salahuddin, J. Shan, L. Shi, O. M. G. Spencer, M. Terrones, W. Windl, J. E. Goldberger, *ACS Nano* **2013**, *7*, 2898.

[19] C.-H. Lee, E. C. Silva, L. Calderin, M. A. T. Nguyen, M. J. Hollander, B. Bersch, T. E. Mallouk, J. A. Robinson, *Sci. Rep.* **2015**, *5*, 10013.

[20] D. H. Keum, S. Cho, J. H. Kim, D.-H. Choe, H.-J. Sung, M. Kan, H. Kang, J.-Y. Hwang, S. W. Kim, H. Yang, K. J. Chang, Y. H. Lee, *Nat. Phys.* **2015**, *11*, 482.

[21] A. Splendiani, L. Sun, Y. Zhang, T. Li, J. Kim, C.-Y. Chim, G. Galli, F. Wang, *Nano Lett.* **2010**, *10*, 1271.

[22] J. C. Park, S. J. Yun, H. Kim, J. H. Park, S. H. Chae, S. J. An, J. G. Kim, S. M. Kim, K. K. Kim, Y. H. Lee, *ACS Nano* **2015**, *9*, 6548.

[23] M. Amani, D.-H. Lien, D. Kiriya, J. Xiao, A. Azcatl, J. Noh, S. R. Madhvapathy, R. Addou, S. Kc, M. Dubey, K. Cho, R. M. Wallace, S. Lee, J. He, J. W. Ager III, X. Zhang, E. Yablonovitch, A. Javey, *Science (80-.).* **2015**, *350*, 1065.

[24] K. M. McCreary, A. T. Hanbicki, G. G. Jernigan, J. C. Culbertson, B. T. Jonker, *Sci. Rep.* **2016**, *6*, 19159.

[25] D. N. Bhavsar, A. R. Jani, *J. Optoelectron. Adv. Mater.* **2014**, *16*, 215.

[26] L. Zhou, K. Xu, A. Zubair, A. D. Liao, W. Fang, F. Ouyang, Y. H. Lee, K. Ueno, R. Saito, T. Palacios, J. Kong, M. S. Dresselhaus, *J. Am. Chem. Soc.* **2015**, *137*, 11892.

[27] M. Moustafa, T. Zandt, C. Janowitz, R. Manzke, *Phys. Rev. B* **2009**, *80*, 35206.

[28] C. Gaiser, T. Zandt, A. Krapf, R. Serverin, C. Janowitz, R. Manzke, *Phys. Rev. B* **2004**, *69*, 75205.

[29] R. H. Williams, A. J. McEvoy, *Phys. Status Solidi* **1972**, *12*, 277.

[30] A. Gouskov, J. Camassel, L. Gouskov, *Prog. Cryst. Growth Charact.* **1982**, *5*, 323.

[31] T. J. Wieting, M. Schluter, *Electrons and Phonons in Layered Crystal Structures*, **2015**.

[32] F. Jellinek, H. Hahn, *Zeitschrift fur Naturforsch. - Sect. B J. Chem. Sci.* **1961**, *16*, 713.

[33] A. Kuhn, A. Chevy, R. Chevalier, *Phys. Status Solidi* **1975**, *31*, 469.

[34] G. Bergerhoff, R. Hundt, R. Sievers, I. D. Brown, *J. Chem. Inf. Model.* **1983**, *23*, 66.

[35] V. H. Hahn, G. Frank, *Zeitschrift fur Anorg. und Allg. Chemie* **1955**, *278*, 340.

[36] C. S. Jung, F. Shojaei, K. Park, J. Y. Oh, H. S. Im, D. M. Jang, J. Park, H. S. Kang, *ACS Nano* **2015**, *9*, 9585.

[37] S. Shigetomi, K. Sakai, T. Ikari, *Jpn. J. Appl. Phys.* **2005**, *44*, 1306.

[38] D. J. Late, B. Liu, J. Luo, A. Yan, H. S. S. R. Matte, M. Grayson, C. N. R. Rao, V. P. Dravid, *Adv. Mater.* **2012**, *24*, 3549.

[39] V. Capozzi, *Phys. Rev. B* **1981**, *23*, 836.

[40] V. Capozzi, M. Montagna, *Phys. Rev. B* **1989**, *40*, 3182.

[41] V. G. Voevodin, O. V. Voevodina, S. a. Bereznaya, Z. V. Korotchenko, A. N. Morozov, S. Y. Sarkisov, N. C. Fernelius, J. T. Goldstein, *Opt. Mater. (Amst).* **2004**, *26*, 495.

[42] N. C. Fernelius, *Prog. Cryst. Growth Charact. Mater.* **1994**, *28*, 275.

[43] K. R. Allakhverdiev, M. Ö. Yetis, S. Özbek, T. K. Baykara, E. Y. Salaev, *Laser Phys.* **2009**, *19*, 1092.

[44] W. Shi, Y. J. Ding, N. Fernelius, K. Vodopyanov, *Opt. Lett.* **2002**, *27*, 1454.

[45] P. Gomes de Costa, R. G. Dandrea, R. F. Wallis, M. Balkanski, *Phys. Rev. B* **1993**, *48*, 14135.

[46] G. W. Mudd, M. R. Molas, X. Chen, V. Zólyomi, K. Nogajewski, Z. R. Kudrynskyi, Z. D. Kovalyuk, G. Yusa, O. Makarovsky, L. Eaves, M. Potemski, V. I. Fal'ko, A. Patanè, *Sci. Rep.* **2016**, *6*, 39619.

[47] A. Segura, F. Pomer, A. Cantarero, W. Krause, A. Chevy, *Phys. Rev. B* **1984**, *29*, 5708.

[48] D. A. Bandurin, A. V. Tyurnina, G. L. Yu, A. Mishchenko, V. Zólyomi, S. V. Morozov, R. K. Kumar, R. V. Gorbachev, Z. R. Kudrynskyi, S. Pezzini, Z. D. Kovalyuk, U. Zeitler, K. S. Novoselov, A. Patanè, L. Eaves, I. V. Grigorieva, V. I. Fal'ko, A. K. Geim, Y. Cao, *Nat. Nanotechnol.* **2016**, *12*, 223.

[49] S. Shigetomi, T. Ikari, *Jpn. J. Appl. Phys.* **2003**, *42*, 6951.

[50] J. Riera, A. Segura, A. Chevy, *Appl. Phys. A Solids Surfaces* **1992**, *54*, 428.

[51] M. Julien-Pouzol, S. Jaulmes, M. Guittard, F. Alapini, *Acta Crystallogr. Sect. B Struct. Crystallogr. Cryst. Chem.* **1979**, *35*, 2848.

[52] C. Rocha Leão, V. Lordi, *Phys. Rev. B* **2011**, *84*, 165206.

[53] S. A. Semelitov, V. A. Vlasov, *Sov. Phys. Crystallogr.* **1964**, *8*, 704.

[54] E. G. Gillan, A. R. Barron, *Chem. Mater.* **1997**, *9*, 3037.

[55] N. N. Kolesnikov, E. B. Borisenko, D. N. Borisenko, A. V Timonina, *J. Cryst. Growth* **2013**, *365*, 59.

[56] J. F. Sánchez-Royo, A. Segura, V. Muñoz, *Phys. Status Solidi* **1995**, *151*, 257.

[57] K. C. Mandal, R. M. Krishna, T. C. Hayes, P. G. Muzykov, S. Das, T. S. Sudarshan, S. Ma, *IEEE Trans. Nucl. Sci.* **2011**, *58*, 1981.

[58] A. Yamamoto, A. Syouji, T. Goto, E. Kulatov, K. Ohno, Y. Kawazoe, K. Uchida, N. Miura, *Phys. Rev. B* **2001**, *64*, 35210.

[59] S. Huang, Y. Tatsumi, X. Ling, H. Guo, Z. Wang, G. Watson, A. A. Puretzky, D. B. Geohegan, J. Kong, J. Li, T. Yang, R. Saito, M. S. Dresselhaus, *ACS Nano* **2016**, *10*, 8964.

[60] J. C. Irwin, B. P. Clayman, D. G. Mead, *Phys. Rev. B* **1979**, *19*, 2099.

[61] G. B. Abdullaev, L. K. Vodopyanov, K. R. Allakhverdiev, L. V Golubev, S. S. Babaev, E. Y. Salaev, *Solid State Commun.* **1979**, *31*, 851.

[62] S. Shigetomi, T. Ikari, H. Nishimura, *J. Lumin.* **1998**, *78*, 117.

[63] A. Zubiaga, J. A. García, F. Plazaola, V. Muñoz-Sanjosé, C. Martínez-Tomás, *Phys. Rev. B* **2003**, *68*, 245202.

[64] C. Manfredotti, R. Murri, A. Rizzo, L. Vasanelli, G. Micocci, *Phys. Status Solidi* **1975**, *29*, 475.

[65] Z. Rak, S. D. Mahanti, K. C. Mandal, N. C. Fernelius, *J. Phys. Condens. Matter* **2009**, *21*, 15504.

[66] X. Yuan, L. Tang, P. Wang, Z. Chen, Y. Zou, *Nano Res.* **2015**, *8*, 3332.

[67] Z. Wang, K. Xu, Y. Li, X. Zhan, M. Safdar, Q. Wang, F. Wang, J. He, *ACS Nano* **2014**, *8*, 4859.

[68] K. Xu, Z. Zhang, Z. Wang, F. Wang, Y. Huang, L. Liao, J. He, *Appl. Phys. Lett.* **2015**, *107*, 153507.

[69] F. Liu, H. Shimotani, H. Shang, T. Kanagasekaran, V. Zólyomi, N. Drummond, V. I. Fal'Ko, K. Tanigaki, *ACS Nano* **2014**, *8*, 752.

[70] P. Hu, J. Zhang, M. Yoon, X. F. Qiao, X. Zhang, W. Feng, P. Tan, W. Zheng, J. Liu, X. Wang, J. C. Idrobo, D. B. Geohegan, K. Xiao, *Nano Res.* **2014**, *7*, 694.

[71] G. Yu, Z. Liu, X. Xie, X. Ouyang, G. Shen, *J. Mater. Chem. C* **2014**, *2*, 6104.

[72] Z. Wang, M. Safdar, M. Mirza, K. Xu, Q. Wang, Y. Huang, F. Wang, X. Zhan, J. He, *Nanoscale* **2015**, *7*, 7252.

[73] F. Wang, Z. Wang, K. Xu, F. Wang, Q. Wang, Y. Huang, L. Yin, J. He, *Nano Lett.* **2015**, *15*, 7558.

[74] P. Lu, X. Wu, W. Guo, X. C. Zeng, *Phys. Chem. Chem. Phys.* **2012**, *14*, 13035.

[75] H. J. Conley, B. Wang, J. I. Ziegler, R. F. Haglund, S. T. Pantelides, K. I. Bolotin, *Nano Lett.* **2013**, *13*, 3626.

[76] H. Guo, N. Lu, L. Wang, X. Wu, X. C. Zeng, *J. Phys. Chem. C* **2014**, *118*, 7242.

[77] R. Kappera, D. Voiry, S. E. Yalcin, B. Branch, G. Gupta, A. D. Mohite, M. Chhowalla, *Nat. Mater.* **2014**, *13*, 1128.

[78] P. Yu, J. Lin, L. Sun, Q. L. Le, X. Yu, G. Gao, C.-H. Hsu, D. Wu, T.-R. Chang, Q. Zeng, F. Liu, Q. J. Wang, H.-T. Jeng, H. Lin, A. Trampert, Z. Shen, K. Suenaga, Z. Liu, *Adv. Mater.* **2017**, *29*, 1603991.

[79] K. A. N. Duerloo, E. J. Reed, *ACS Nano* **2016**, *10*, 289.

[80] S. M. Sze, K. K. Ng, *Physics of Semiconductor Devices*, John Wiley & Sons, **2007**.

[81] H. Xu, S. Liu, Z. Ding, S. J. R. Tan, K. M. Yam, Y. Bao, C. T. Nai, M.-F. Ng, J. Lu, C. Zhang, K. P. Loh, *Nat. Commun.* **2016**, *7*, 12904.

[82] H. Tu, V. Chikan, D. F. Kelley, *J. Phys. Chem. B* **2003**, *107*, 10389.

[83] H. D. Ha, D. J. Han, J. S. Choi, M. Park, T. S. Seo, *Small* **2014**, *10*, 3858.

[84] C. S. Schnohr, *Appl. Phys. Rev.* **2015**, *2*, 31304.

[85] H. Liu, K. Antwi, S. Chua, D. Chi, *Nanoscale* **2014**, *6*, 624.

[86] S. Tongay, D. S. Narang, J. Kang, W. Fan, C. Ko, A. V. Luce, K. X. Wang, J. Suh, K. D. Patel, V. M. Pathak, J. Li, J. Wu, *Appl. Phys. Lett.* **2014**, *104*, 12101.

[87] Q. Fu, L. Yang, W. Wang, A. Han, J. Huang, P. Du, Z. Fan, J. Zhang, B. Xiang, *Adv. Mater.* **2015**, *27*, 4732.

[88] E. Aulich, J. L. Brebner, E. Mooser, *Phys. Status Solidi* **1969**, *31*, 129.

[89] L.-Y. Gan, Q. Zhang, Y.-J. Zhao, Y. Cheng, U. Schwingenschlögl, *Sci. Rep.* **2014**, *4*, 6691.

[90] K. M. Yu, W. L. Sarney, S. V Novikov, N. Segercrantz, M. Ting, M. Shaw, S. P. Svensson, R. W. Martin, W. Walukiewicz, C. T. Foxon, *Semicond. Sci. Technol.* **2016**, *31*, 83001.

[91] T. Tanaka, K. M. Yu, A. X. Levander, O. D. Dubon, L. a. Reichertz, N. Lopez, M. Nishio, W. Walukiewicz, *Jpn. J. Appl. Phys.* **2011**, *50*, 82304.

[92] J. Camassel, P. Merle, H. Mathieu, A. Gouskov, *Phys. Rev. B* **1979**, *19*, 1060.

[93] C. A. Francis, D. M. Detert, G. Chen, O. D. Dubon, K. M. Yu, W. Walukiewicz, *Appl. Phys. Lett.* **2015**, *106*, 1.

[94] P. W. Bridgman, *Am. Acad. Arts Sci.* **1925**, *60*, 305.

[95] J. I. Pankove, *Optical Processes in Semiconductors*, Dover Publications, **1975**.

[96] O. S. Heavens, *Optical Properties of Thin Film Solids*, Dover Publications, **1991**.

[97] M. Abdel Rahman, A. E. Belal, *J. Phys. Chem. Solids* **2000**, *61*, 925.

[98] M. Mohil, G. A. Kumar, *J. Nano- Electron. Phys.* **2013**, *5*, 2018.

[99] V. M. Bermudez, *Chem. Phys.* **2006**, *323*, 193.

[100] K. Allakhverdiev, N. Ismailov, Z. Salaeva, F. Mikailov, A. Gulubayov, T. Mamedov, S. Babaev, *Appl. Opt.* **2002**, *41*, 148.

[101] D. C. Harris, M. D. Bertolucci, *Symmetry and Apectroscopy: An Introduction to Vibrational and Electronic Spectroscopy*, Dover Publications, **1989**.

[102] F. Cerdeira, E. A. Meneses, A. Gouskov, *Phys. Rev. B* **1977**, *16*, 1648.

[103] K. C. Mandal, T. Hayes, P. G. Muzykov, R. Krishna, S. Das, T. S. Sudarshan, S. Ma, *Proc. SPIE* **2010**, *7805*, 78050Q1.

[104] Q. Zhao, T. Wang, Y. Miao, F. Ma, Y. Xie, X. Ma, Y. Gu, J. Li, J. He, B. Chen, S. Xi, L. Xu, H. Zhen, Z. Yin, J. Li, J. Ren, W. Jie, *Phys. Chem. Chem. Phys.* **2016**, *18*, 18719.

[105] L. J. van der Pauw, *Philips Res. Reports1* **1958**, *13*, 1.

[106] C. R. Barrett, W. D. Nix, A. S. Tetelman, *The Principles of Engineering Materials*, Prentice-Hall, **1973**.

[107] A. Favron, E. Gaufres, F. Fossard, A.-L. Phaneuf-L'Heureux, N. Y.-W. Tang, P. L. Levesque, A. Loiseau, R. Leonelli, S. Francoeur, R. Martel, *Nat Mater* **2015**, *15*, 826.

[108] O. A. Balitskii, *Mater. Lett.* **2006**, *60*, 594.

[109] O. A. Balitskii, W. Jaegermann, *Mater. Chem. Phys.* **2006**, *97*, 98.

[110] M. Nauer, K. Ernst, W. Kautek, M. Neumann-Spallart, *Thin Solid Films* **2005**, *489*, 86.

[111] C. Ma, J. Huang, H. Chen, *Thin Solid Films* **2002**, *418*, 73.

[112] V. D. Mote, Y. Purushotham, B. N. Dole, *J. Theor. Appl. Phys.* **2012**, *6*, 1.

[113] G. K. Williamson, W. H. Hall, *Acta Metall.* **1953**, *1*, 22.

[114] S. Pereira, M. R. Correia, E. Pereira, K. P. O'Donnell, E. Alves, A. D. Sequeira, N. Franco, I. M. Watson, C. J. Deatcher, *Appl. Phys. Lett.* **2002**, *80*, 3913.

[115] C. Tatsuyama, Y. Watanabe, C. Hamaguchi, *J. Phys. Soc. Japan1* **1970**, *29*, 150.

[116] J. F. Sánchez-Royo, J. Pellicer-Porres, A. Segura, V. Muñoz-Sanjosé, G. Tobías, P. Ordejón, E. Canadell, Y. Huttel, *Phys. Rev. B* **2002**, *65*, 115201.

[117] J. F. Ribeiro, R. Sousa, J. A. Sousa, B. M. Pereira, M. F. Silva, L. M. Goncalves, M. M. Silva, J. H. Correia, *Procedia Eng.* **2012**, *47*, 676.

[118] Q. Dong, F. Liu, M. K. Wong, H. W. Tam, A. B. Djurišić, A. Ng, C. Surya, W. K. Chan, A. M. C. Ng, *ChemSusChem* **2016**, *9*, 2597.

[119] A. Avsar, I. J. Vera-Marun, J. Y. Tan, K. Watanabe, T. Taniguchi, A. H. Castro Neto, B. Özyilmaz, *ACS Nano* **2015**, *9*, 4138.

[120] J. Susoma, J. Lahtinen, M. Kim, J. Riikonen, H. Lipsanen, *AIP Adv.* **2017**, *7*, 15014.

[121] I. B. Butler, M. A. A. Schoonen, D. T. Rickard, *Talanta* **1994**, *41*, 211.

[122] J. Jeong, N. Aetukuri, T. Graf, T. D. Schladt, M. G. Samant, S. S. P. Parkin, *Science* **2013**, *339*, 1402.

[123] D. Meyers, J. Liu, J. W. Freeland, S. Middey, M. Kareev, J. Kwon, J. M. Zuo, Y.-D. Chuang, J. W. Kim, P. J. Ryan, J. Chakhalian, *Sci. Rep.* **2016**, *6*, 27934.

[124] R. Könenkamp, *Phys. Rev. B* **1988**, *38*, 3056.

[125] B. Radisavljevic, A. Kis, *Nat. Mater.* **2013**, *12*, 815.

[126] V. N. Katerinchuk, M. Z. Kovalyuk, *Tech. Phys. Lett.* **1999**, *25*, 54.

[127] W. Walukiewicz, *Phys. B Condens. Matter* **2001**, *302–303*, 123.

[128] O. Lang, A. Klein, C. Pettenkofer, W. Jaegermann, A. Chevy, *J. Appl. Phys.* **1996**, *80*, 3817.

[129] S. Kurtin, C. A. Mead, *J. Phys. Chem. Solids* **1969**, *30*, 2007.

[130] W. Walukiewicz, *Phys. Rev. B* **1988**, *37*, 4760.

[131] W. Walukiewicz, *Appl. Phys. Lett.* **1989**, *54*, 2094.

[132] V. Dhyani, S. Das, *Sci. Rep.* **2017**, *7*, 44243.

[133] Y. Liang, S. Huang, R. Soklaski, L. Yang, *Appl. Phys. Lett.* **2013**, *103*, 42106.

[134] H. Reqqass, J. P. Lacharme, C. A. Sébenne, M. Eddrief, V. Le Thanh, *Appl. Surf. Sci.* **1996**, *92*, 357.

[135] V. S. Vavilov, N. A. Ukhin, *Radiation Effects in Semiconductors and Semiconductor Apparatuses*, Freund Publishing House, **1977**.

[134] L. Gouskov, A. Gouskov, *Solid State Commun.* **1978**, *28*, 99.

[135] A. Zubiaga, J. A. García, F. Plazaola, V. Muñoz-Sanjosé, M. C. Martínez-Tomás, *J. Appl. Phys.* **2002**, *92*, 7330.

[136] J. R. Haynes, *Phys. Rev. Lett.* **1960**, *4*, 361.

[137] H. Güder, B. Abay, H. Efeoglu, Y. Yogurtcu, *J. Lumin.* **2001**, *93*, 243.

[138] Y. Cui, D. D. Caudel, P. Bhattacharya, A. Burger, K. C. Mandal, D. Johnstone, S. A. Payne, *J. Appl. Phys.* **2009**, *105*, 53709.

[139] A. Rockett, in *Mater. Sci. Semicond.*, **2008**, pp. 237–288.

[140] K. Yu, W. Walukiewicz, J. Wu, W. Shan, J. Beeman, M. Scarpulla, O. Dubon, P. Becla, *Phys. Rev. Lett.* **2003**, *91*, 246403.

[141] X. Li, M. W. Lin, L. Basile, S. M. Hus, A. A. Puretzky, J. Lee, Y. C. Kuo, L. Y. Chang, K. Wang, J. C. Idrobo, A. P. Li, C. H. Chen, C. M. Rouleau, D. B. Geohegan, K. Xiao, *Adv. Mater.* **2016**, *28*, 8240.

[142] E. A. Meneses, N. Jannuzzi, J. R. Freitas, A. Gouskov, *Phys. Status Solidi* **1976**, *78*, K35.

[143] L. Gouskov, A. Gouskov, M. H. A. J. Jar, L. Soonckindt, C. Llinares, *Phys. B+C* **1980**, *99*, 291.

[144] L. Gouskov, A. Gouskov, V. Lemos, W. May, H. Sampaio, *Phys. Status Solidi* **1977**, *39*, 65.

[145] G. M. Mamedov, M. Karabulut, H. Ertap, O. Kodolbaş, Ö. Öktü, A. Bacioğlu, *J. Lumin.* **2009**, *129*, 226.

[146] H. Peng, S. Meister, C. K. Chan, X. F. Zhang, Y. Cui, *Nano Lett.* **2007**, *7*, 199.

[147] G. Shen, D. Chen, P. Chen, C. Zhou, *ACS Nano* **2009**, *3*, 1115.

[148] L. S. Brooks, *J. Am. Chem. Soc.* **1952**, *74*, 227.

[149] A. P. Ubelis, *J. Eng. Phys.* **1982**, *42*, 309.

[150] C. J. Hawley, B. R. Beatty, G. Chen, J. E. Spanier, *Cryst. Growth Des.* **2012**, *12*, 2789.

[151] K. L. Chopra, *Phys. Status Solidi* **1969**, *32*, 489.

[152] A. Jain, S. P. Ong, G. Hautier, W. Chen, W. D. Richards, S. Dacek, S. Cholia, D. Gunter, D. Skinner, G. Ceder, K. A. Persson, *APL Mater.* **2013**, *1*, 11002.

[153] F. Tran, P. Blaha, *Phys. Rev. Lett.* **2009**, *102*, 5.

[154] J. A. Camargo-Martínez, R. Baquero, *Superf. y Vacio* **2013**, *26*, 54.

[155] U. Schwarz, K. Syassen, R. Kniep, *J. Alloys Compd.* **1995**, *224*, 212.

[156] O. A. Balitskii, B. Jaeckel, W. Jaegermann, *Phys. Lett. A* **2008**, *372*, 3303.

[157] L. V. Yashina, R. Püttner, a. a. Volykhov, P. Stojanov, J. Riley, S. Y. Vassiliev, a. N. Chaika, S. N. Dedyulin, M. E. Tamm, D. V. Vyalikh, a. I. Belogorokhov, *Phys. Rev. B* **2012**, *85*, 75409.

[158] P. Galiy, T. Nenchuk, A. Ciszewski, P. Mazur, S. Zuber, I. Yarovets, *Metallofiz. i Noveishie Tekhnologii* **2015**, *37*, 789.

[159] U. S. Shenoy, U. Gupta, D. S. Narang, D. J. Late, U. V. Waghmare, C. N. R. Rao, *Chem. Phys. Lett.* **2016**, *651*, 148.

[160] X. Li, M.-W. Lin, A. Puretzky, J. C. Idrobo, C. Ma, M. Chi, M. Yoon, C. M. Rouleau, I. I. Kravchenko, D. B. Geohegan, K. Xiao, *Sci. Rep.* **2014**, *4*, 5497.

[161] A. M. El Sayed, A. Ibrahim, *Mater. Sci. Semicond. Process.* **2014**, *26*, 320.

[162] W. Chen, D. Qi, X. Gao, A. T. S. Wee, *Prog. Surf. Sci.* **2009**, *84*, 279.

[163] H. Sakai, K. Ikeura, M. S. Bahramy, N. Ogawa, D. Hashizume, J. Fujioka, Y. Tokura, S. Ishiwata, *Sci. Adv.* **2016**, *2*, e1601378.

[164] T. Komatsubara, M. Murakami, E. Hirahara, *J. Phys. Soc. Japanhe Phys. ocie* **1963**, *18*, 356.

[165] J. F. Ziegler, J. P. Biersack, in *Treatise Heavy-Ion Sci. Vol. 6 Astrophys. Chem. Condens. Matter* (Ed.: D.A. Bromley), Springer US, Boston, MA, **1985**, pp. 93–129.

[166] J. Perdew, K. Burke, M. Ernzerhof, *Phys. Rev. Lett.* **1996**, *77*, 3865.

[167] S. Grimme, *J. Comput. Chem.* **2006**, *27*, 1787.

[168] J. Heyd, G. E. Scuseria, M. Ernzerhof, *J. Chem. Phys.* **2006**, *124*, 219906.

[169] K. Hummer, J. Harl, G. Kresse, *Phys. Rev. B* **2009**, *80*, 115205.

[170] G. Kresse, D. Joubert, *Phys. Rev. B* **1999**, *59*, 1758.

[171] G. Kresse, J. Hafner, *Phys. Rev. B* **1993**, *47*, 558(R).

[172] F. Patolsky, G. Zheng, C. M. Lieber, *Nat. Protoc.* **2006**, *1*, 1711.

[173] G. Kresse, J. Furthmüller, *Phys. Rev. B* **1996**, *54*, 11169.

[174] P. G. Moses, C. G. Van De Walle, *Appl. Phys. Lett.* **2010**, *96*, 94.

[175] C. A. Niedermeier, M. Råsander, S. Rhode, V. Kachkanov, B. Zou, N. Alford, M. A. Moram, *Sci. Rep.* **2016**, *6*, 31230.

[176] S. P. Ong, W. D. Richards, A. Jain, G. Hautier, M. Kocher, S. Cholia, D. Gunter, V. L. Chevrier, K. A. Persson, G. Ceder, *Comput. Mater. Sci.* **2013**, *68*, 314.